

Alma Mater Studiorum - Università di Bologna

DOTTORATO DI RICERCA IN
IL FUTURO DELLA TERRA, CAMBIAMENTI CLIMATICI E SFIDE
SOCIALI

Ciclo 35

Settore Concorsuale: 02/C1 - ASTRONOMIA, ASTROFISICA, FISICA DELLA TERRA E DEI
PIANETI

Settore Scientifico Disciplinare: FIS/06 - FISICA PER IL SISTEMA TERRA E IL MEZZO
CIRCUMTERRESTRE

ANALYSIS OF HEAT-RELATED PHENOMENA AND THEIR INTERACTIONS AT
DIFFERENT SPATIO-TEMPORAL SCALES

Presentata da: Marco Possega

Coordinatore Dottorato

Silvana Di Sabatino

Supervisore

Silvana Di Sabatino

Co-supervisori

Paolo Ruggieri
Leonardo Aragão

Esame finale anno 2023

Abstract

This thesis analyzes the impact of heat extremes in urban and rural environments, considering processes related to severely high temperatures and unusual dryness. The first part deals with the influence of large-scale heatwave events on the local-scale urban heat island (UHI) effect. The temperatures recorded over a 20-year summer period by meteorological stations in 37 European cities are examined to evaluate the variations of UHI during heatwaves with respect to non-heatwave days. A statistical analysis reveals a negligible impact of large-scale extreme temperatures on the local daytime urban climate, while a notable exacerbation of UHI effect at night. A comparison with the UrbClim model outputs confirms the UHI strengthening during heatwave episodes, with an intensity independent of the climate zone. The investigation of the relationship between large-scale temperature anomalies and UHI highlights a smooth and continuous dependence, but with a strong variability. The lack of a threshold behavior in this relationship suggests that large-scale temperature variability can affect the local-scale UHI even in different conditions than during extreme events.

The second part examines the transition from meteorological to agricultural drought, being the first stage of the drought propagation process. A multi-year reanalysis dataset involving numerous drought events over the Iberian Peninsula is considered. The behavior of different non-parametric standardized drought indices in drought detection is evaluated. A statistical approach based on run theory is employed, analyzing the main characteristics of drought propagation. The propagation from meteorological to agricultural drought events is found to develop in about 1-2 months. The duration of agricultural drought appears shorter than that of meteorological drought, but the onset is delayed. The propagation probability increases with the severity of the originating meteorological drought. A new combined agricultural drought index is developed to be a useful tool for balancing the characteristics of other adopted indices.

Contents

1	Introduction	3
1.1	Heat-Related Extreme Events	3
1.2	Objective and Thesis Structure	5
2	Notions of Heatwaves and Urban Heat Island	9
2.1	Heatwaves	9
2.1.1	Defining a Heatwave	9
2.1.2	Mechanism and Characteristics of European Heatwaves	10
2.2	The Urban Heat Island Effect	12
2.2.1	Urban Heat Island Classification and Retrieving Methods	13
2.2.2	Energy Budget of Urban Heat Island	15
2.2.3	Impact of Heatwaves on Urban Heat Island	17
3	Study of Urban Heat Island during Heatwaves in Europe	20
3.1	Purpose	20
3.2	Methodology	22
3.2.1	Data Sources for Urban Heat Island Analysis	22
3.2.2	Urban Heat Island Index	22
3.2.3	Method to Select Cities and Weather Stations	23
3.2.4	Selection Results	24
3.2.5	Method for Heatwaves Identification	25
3.2.6	Characteristics of Identified Heatwaves	27
3.2.7	Methods of Analysis	29
3.3	Results and Discussion	33
3.3.1	Statistical Analysis	33
3.3.2	Temporal Evolution	39
3.3.3	Correlation Analysis	41
3.4	Comparison with UrbClim Model Products	44
3.4.1	The UrbClim Model	44
3.4.2	Methodology	44

3.4.3	Results and Discussion	45
3.5	Synthesis of the Main Results	47
4	Concepts of Drought	49
4.1	Definitions of Drought	49
4.2	Drought Propagation and Indices	52
5	Analysis of Drought Propagation over the Iberian Peninsula	56
5.1	Purpose	56
5.1.1	The Iberian Peninsula Hot Spot	57
5.2	Methodology	59
5.2.1	Drought Indices	59
5.2.2	Dataset	62
5.2.3	Methods of Analysis	63
5.3	Results and Discussion	67
5.3.1	Characterization of Drought Phenomena over IP	67
5.3.2	Propagation from Meteorological to Agricultural Drought	73
5.4	Synthesis of the Main Results	85
6	Conclusion	86
6.1	Summary of Relevant Outcomes	86
6.2	Future Developments	89

Chapter 1

Introduction

1.1 Heat-Related Extreme Events

All over the world, the effects of human-induced climate change are well documented in several kinds of weather and climate hazardous phenomena. Heatwaves, heavy rainfalls, tropical cyclones, river flooding and droughts have become more frequent during the last decades and, according to the Sixth Assessment report from the Intergovernmental Panel on Climate Change IPCC (Masson-Delmotte et al. [1]), their intensities are unprecedented in the observed record and will further increase in alignment with global warming. In particular, the worldwide dramatic growth in temperature monitored since the 1950s, with 2012-2021 defined as the hottest measured decade since the beginning of thermometer-based observations, has originated a substantial amplification of heat-related extremes.

The relationship between global warming and heat extremes can be effortlessly comprehended from a statistical point of view. Considering a normal distribution of possible temperatures in a certain region, the most likely values of observable temperature are concentrated at the center of the curve, while the most rare events are located at the edges. Under the simplifying assumption that the shape of frequency distribution stays approximately unvaried when its average modifies, the most appreciable relative changes lie in the “tails” of the distribution. In this regard, to reproduce the effect of global warming, a shift can be applied to the whole curve by enhancing the average temperature of a small δT . After this alteration, the perceived effect near the center of the curve is not really marked, whereas changes in the extremes are substantial. Indeed, the previously estimated extremes have become not so unusual, and even more impactful events, which were not feasible before, can occur (see Figure 1.1).

Abandoning statistics to make considerations of a physical nature, the most rel-

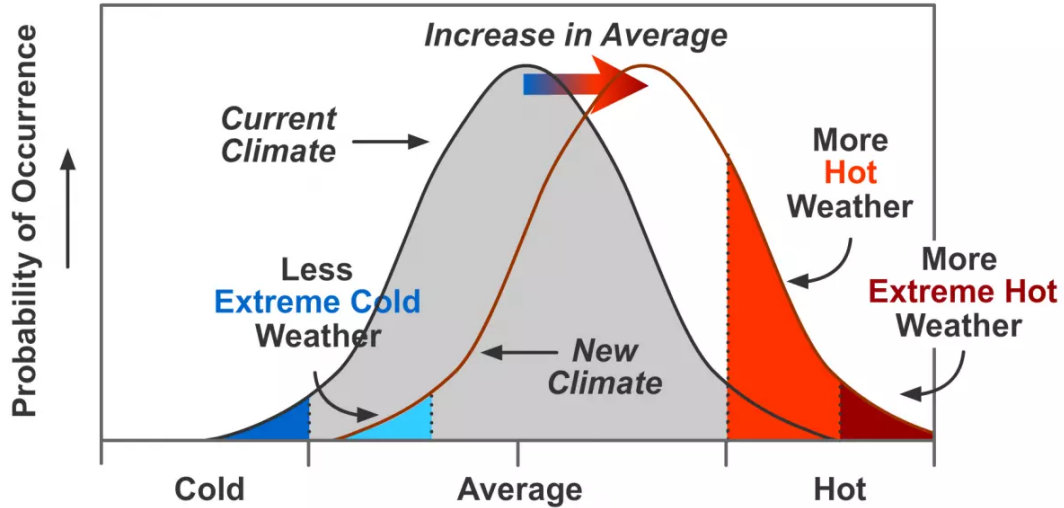


Figure 1.1: Schematic showing the effect on extreme temperatures when the average temperature increases of a small δT considering a normal distribution. From Masson-Delmotte et al. [1].

evant effect of this shift towards higher temperatures is the strengthening of evaporation rate from Earth's surface and the increment of precipitable water. In fact, from the Clausius-Clapeyron equation (Brown [2]) it can be deduced that, for a 1°C temperature increase, the equilibrium vapor pressure of water grows approximately of 7%. Therefore, keeping a fixed relative humidity, the atmospheric water vapor available for conversion into rainfall increases, concurrently with the loss of water from the surface by evapotranspiration in dry land conditions. In other words, an exacerbation of the raise of temperature leads to both more meaningful precipitation phenomena and to an accelerated soil desiccation, namely heavy storms and severe droughts. Moreover, several feedback responses can be activated through dynamical and thermo-dynamical processes capable of farther aggravating the impacts of global warming. For example, when droughts occur dehydrating the surface, the evaporative cooling can be reduced, producing additional heat-related extremes.

The environmental factors characterizing severe thermal climatic conditions can seriously affect human health and well-being. Indeed, the human body responds to hot temperatures by lowering the blood pressure, accelerating the heartbeat and enhancing the loss of body fluids through perspiration. These variations can jeopardize the cardiovascular system, particularly in infirm and elder people, and for this reason the extreme heat is one of the main weather-related causes of death worldwide. In this respect, Figure 1.2 shows the increasing trend of global heat-related mortality for old people during the last 20 years. However, not only the air temperature can generate a stress accumulation for human body, but also hu-

midity, wind speed and radiation play a significant role in what is called *perceived temperature*, which is proven to be strongly correlated with the rate of mortality during periods of extremely hot meteorological conditions. In addition to its health effects, prolonged periods of heat may negatively influence economy. To cite some critical effects, roads, electrical wires and other infrastructure can get damaged and even enhance the accident rate, more expenses are needed to maintain efficient air conditioning systems and generally employee productivity diminishes during adverse work conditions.

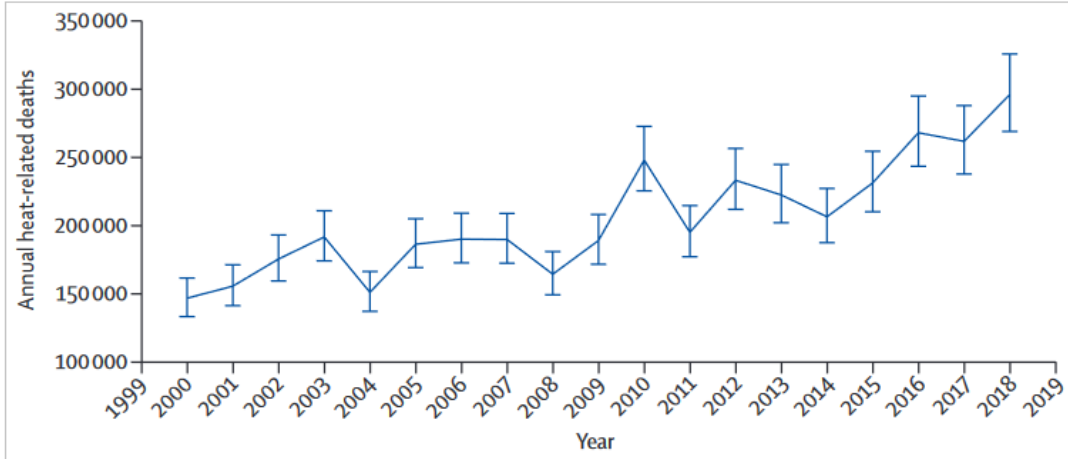


Figure 1.2: Global heat-related mortality for people older than 65 years. From Watts et al. [3].

Besides heatwaves and severe temperatures, also prolonged dry conditions connected with extreme heat patterns can be responsible of disastrous consequences on many regions across the globe. The development of droughts, indeed, can produce major impacts on agriculture, with repercussions involving crop and livestock shortage and incidence of plant diseases, ultimately leading to famine. During recurring periods of drought, the damage to ground and flora often become so irreversible that the land is transformed into desert. The low availability of water implies the reduction of activities of hydroelectric and thermal power plants, with related high economic losses for the sectors involved. Finally, dangerous wildfires can be generated in case of prolonged hot temperatures and extremely dry conditions.

1.2 Objective and Thesis Structure

The study of heat-related extreme events has acquired rising importance during the last years, both for their documented exacerbation in intensity and frequency and for the posed threats. In particular, the potential multi-scale features of these phenomena and the generated impacts on various natural and human ecosystems are issues of

primary interest. For example, considering extremes associated to hot temperatures, the formation of a heatwave at large scale is capable to influence human health in populated areas, affecting the local scale urban heat island effect. This phenomenon, especially marked at night, consists in a higher temperature retrieved in urban centers with respect to the surrounding rural areas, mainly due to the anthropogenic heat released from buildings, to the reduced vegetation and evapotranspiration and to the abundance of low albedo surfaces. Therefore, the large-scale temperature anomaly generated by a heatwave occurrence may have repercussions on the urban heat island intensity, with results depending on the different response of urban and rural environment to the unusual warming. Several studies have addressed the issue of the relationship between urban heat island and heatwave, following various approaches ranging from numerical to observational analyses. Generally, the literature on urban heat island-heatwave interaction reveals an increase of urban heat island during heatwaves in numerous cases, while some studies assess the absence of a significant synergy between the two phenomena, or even a lowering effect of heatwaves on the urban heat island. The lack of a universally accepted multi-scale modelling approach and the inhomogeneities in data and adopted methodologies complicate the comparison through the results of different studies, and reaching a consistent assessment about the effect produced on urban heat island by heatwave events is a challenging task. Recently, diverse research gaps have been identified, in particular regarding the importance to examine multi-year datasets including multiple heatwave episodes, and the usefulness of analyzing collections of cities with distinct characteristics to reveal the general trend. The first part of the thesis attempts to fill these gaps for the European continent, by evaluating the heatwave effects on the urban heat island of a large ensemble of European cities over a period of 20 years with an empirical approach, estimating the urban heat island intensity from daily temperature measured by meteorological stations.

Considering instead extremes connected to dry patterns, since the effects of precipitation deficits occur in different systems with distinct time scales, drought can be defined a multi-scale event. Indeed, the drought signal propagates through the water cycle involving a multitude of processes, and this phenomenon takes the name of drought propagation. The first transition typically occurs when the development of large-scale precipitation deficits provokes consequences on cultivated areas, inducing soil moisture deficits affecting plant growth and crop yield. In this way, the propagation from a meteorological to an agricultural drought takes place, according to the response of soil to variables as precipitation and evapotranspiration. Currently, studies about this kind of process are rather limited, and more investigations are necessary to understand the propagation characteristics especially in terms of tem-

poral response and of driving factors. Since usually only the soil moisture is taken into account in examining agricultural droughts, the combined contribute provided by evapotranspiration and precipitation deficits has not been completely explored. Therefore, the application of recently formulated multi-variate indices could be useful to clarify this aspect. Moreover, although the investigation of drought propagation requires long-term data, the majority of studies are based on poor observation networks with relatively short records of soil moisture. The second part of the thesis tries to overcome these research gaps regarding the analysis of agricultural drought phenomena and particularly the propagation from meteorological droughts, employing a long multi-annual dataset containing numerous drought events and diverse types of standardized drought indices which take into account the various physical quantities involved. The analysis aims at describing the multi-scale drought propagation characteristics, and it is entirely conducted over the Iberian Peninsula, a widely acknowledged drought-prone area.

This thesis fits in the field of studies concerning the investigation of interaction and propagation of heat-related extreme events, considering the effects of large-scale occurrences on phenomena acting at a different spatio-temporal scale. The overarching purpose is to analyze how the heat extremes influence both urban and rural environment taking separately into account hazardous processes dealing with severely high temperatures and unusual dryness. In this regard, the thesis addresses two distinct problems by examining independently the heatwave and the drought phenomenon, trying to reach conclusions about the relationship between different scales heat-related events.

After this introductory chapter, the thesis is structured as follows:

- Chapter 2 separately describes the general characteristics of heatwaves and urban heat island phenomena, then it focuses on the main drivers and outcomes of their relationship according to the recent literature;
- Chapter 3 discusses in detail the research gaps and the purpose of the conducted study about the urban heat island effect during heatwaves in European cities through observational data, then it describes the employed methodology and the major outcomes retrieved;
- Chapter 4 introduces the drought phenomenon, reporting the main features of the different types of drought and the relevant concepts about drought propagation, also illustrating some examples of the most adopted standardized drought indices;

- Chapter 5 precisely clarifies the objective of the study about droughts, and includes the information about the analyses performed to characterize drought events on the Iberian Peninsula, with a focus on the propagation from meteorological to agricultural droughts;
- Chapter 6 delineates the concluding discussion about the whole work, providing the summary of the main results and furnishing ideas for future developments.

Chapter 2

Notions of Heatwaves and Urban Heat Island

2.1 Heatwaves

Among the environmental extremes, heatwaves are one of the most dangerous because of their impacts on many different systems such as human health, infrastructures, natural habitats and socioeconomy. For example, two significant episodes recently experienced in the European continent were the 2003 Central Europe heatwave, characterized by reiterated temperatures of 35 to 40 °C causing economic damages superior to 13 billion euros (De Bono et al. [4]) and more than 70,000 life losses (Guha-Sapir et al. [5]), and the 2010 Eastern Europe/Russia heatwave, that provoked more than 50,000 deaths in several countries (Barriopedro et al. [6]). These kinds of events are proven to be more frequent and severe in the last decades, and the evolution of climate change will be responsible of a further aggravation of this trend in the future years (Guerreiro et al. [7], Fischer et al. [8] and Perkins-Kirkpatrick et al. [9]).

2.1.1 Defining a Heatwave

Intuitively, a heatwave is a phenomenon which features large-scale persistent high-temperature conditions that may have adverse health effects on the affected population. Even though heatwaves can be considered from a climatological perspective, they are identified as meteorological events since generally their temporal scale is limited to one week, with the most impactful effects relevant on regional spatial scales. However, despite the widespread usage and understanding of the term *heatwave* with the associated features, there is still lack of a unified definition for this

phenomenon. Indeed, the majority of studies involving heatwaves adopt different metrics, particularly due to the multiple factors related to their characterization, for example the temperature climatology varying with the investigated locations. To provide a guideline, the World Meteorological Organization WMO (Bekiashev et al. [10]) delineated a recommended definition of heatwave, designating it as ” *A period of marked unusual hot weather over a region persisting for at least three consecutive days during the warm period of the year based on local climatological conditions, with thermal conditions recorded above given thresholds*”. Since this overall definition leaves room for interpretation, a range of weather-related and bioclimatic indices were developed to identify the heatwaves, by using methodologies often valid only for a specific region or purpose. In spite of the large number of definitions employed in literature, it is possible to find three parameters which differentiate them:

- **Temperature Metric** - The type of temperature indicator selected to properly consider the features of a heatwave. A wide range of variables has been used including maximum temperature, mean temperature, apparent temperature, heat index and their combinations. For studies regarding death exposure in urban areas, frequently the minimum temperature at night is chosen, while daytime temperature is barely important;
- **Intensity** - The kind of temperature threshold imposed. It can be a relative threshold, namely a temperature percentile (the most used are 90th, 95th and 99th percentiles) or an absolute threshold depending on the area of interest, usually ranging from 35 to 38 °C;
- **Duration Threshold** - The minimum number of consecutive days with temperature above the chosen threshold. It does not necessarily match the 3 days recommendations by WMO, and it generally varies from 2 to 6 days depending on the aim of the analysis.

2.1.2 Mechanism and Characteristics of European Heatwaves

The synoptic structure which commonly characterizes the heatwaves is the *blocking high* (Coughlan et al. [11]), namely a quasi-stationary and self-sustaining high-pressure system whose center remains in a fixed location for a longer period than usual, 7-10 days on average. Typically blockings originate from tropospheric flows which are influenced by a large meridional flow component, capable of interrupting the zonal westerly flow at the mid-latitudes (Nakamura et al. [12]). More specifically, traditional blocking highs occur due to the meandering of the jet stream, which is a narrow band of fast-moving air in the upper atmosphere that influences weather

patterns. When the jet stream meanders, it can split into two branches, with one branch passing to the north and the other to the south of the blocked region. This creates a blockage that prevents the normal eastward movement of weather systems. As a result, the region affected by the blocking high experiences several days of relatively stable weather conditions, often characterized by clear skies and warm temperatures. The lack of mixing between colder air to the north and warmer air to the south allows the warm air to build up, leading to an increase of high pressure at the surface. This high pressure system, which further reinforces the blockage and helps to maintain the stable weather conditions, generally extends vertically from the surface to the entire troposphere, with large pressure anomalies at the 500 hpa geopotential height (Figure 2.1 shows an example of observed high-pressure anomalies at 500 hPa during the 2003 European heatwave).

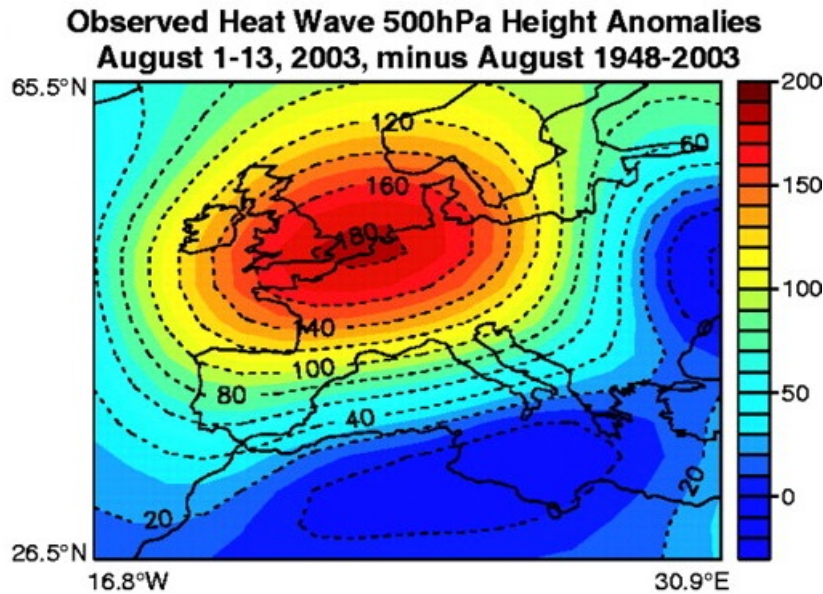


Figure 2.1: Observed geopotential height anomalies at 500 hPa (gpm) during the European heatwave in 2003. Anomalies were calculated against the 1948–2003 monthly averages of August, the month when the heatwave occurred. From Meehl et al. [13].

The persistent anticyclonic flow anomalies of blockings strongly correlates with the occurrence of European temperature extremes in summer. Indeed, heatwaves in Europe are typically associated with co-located anticyclonic circulation features in the free troposphere, mostly due to a northward displacement of an anticyclonic ridge from North Africa with a southerly advection of hot air, and high pressure anomalies throughout the troposphere till the surface. More in detail, European heatwaves form through two main processes, both fostered by blockings: heat accumulation due to atmospheric transport and diabatic heating via radiation and surface fluxes (Miralles et al. [14]). Clearly the blocking formation itself, associated

to the northward advection of subtropical warm dry air masses to the region affected, plays an important role. However, this effect is mostly relevant in the middle and upper troposphere, while it is of only secondary importance for the near-surface air layers. In fact, the accumulation of heat near the surface is mainly resulting from the adiabatic descent of air inside the blocking anticyclones, which is also linked to clear-sky conditions promoting firstly the surface heating by solar radiation, and secondly the diabatic heating of the near-surface air due to enhanced sensible heat fluxes. Moreover, the soil moisture can be fundamental for this diabatic heating depending on a feedback mechanism (Miralles et al. [15]). Whereby the precipitation deficit in the blocking region provokes a depletion of soil moisture and, thus, an increment in the sensible heat fluxes, the latent heat fluxes become almost negligible and a further atmospheric heating and soil drying occur. Viceversa, when the land surface has plenty of moisture, latent heat is the dominant flux over sensible heat, producing a negative feedback. However, in both cases the duration of blocking strongly impacts the lifetime of the heatwaves, and consequently the long-term accumulation of heat.

2.2 The Urban Heat Island Effect

The growth of urban population, which has recently overcome the 50% of total population across the globe (World Bank [16]), and the fact that urban-based activities have repercussions both at the local and at the large scales, have contributed to augment the interest about phenomena affecting the urban climate. Moreover, the concomitant evolution of global warming has aggravated both the heat-related health effects and the vulnerability of urban populations. The urbanization process transformed the environments characterized by natural vegetation into agglomerations of buildings whose structure enhances the thermal-storage capacity, producing notable modifications in urban climate with respect to adjacent rural areas, resulting in the so called urban heat island (UHI) effect (Oke [17]). Most major global cities experience UHI to varying degrees, mostly due to the combined effect of the elevated thermal inertia provided by asphalt roads and the other impervious surfaces of the urban environment, the low ventilation induced by the urban “canyons” between tall buildings, and the heat emanated from vehicles and air conditioners. The most serious concern about UHI effect is the large heat absorption during the daytime and its diffusion at night, with the subsequent raise of the nighttime minimum temperatures which can lead to an exacerbation of heat-related mortality.

2.2.1 Urban Heat Island Classification and Retrieving Methods

The urban heat island is generally defined as a variation in temperature between urban areas and their surroundings, but it is possible to classify four types of UHI considering various layers to calculate the temperature difference (Figure 2.2). In particular:

- **Subsurface UHI** (UHI_{sub}): the temperature gradient between subsoil urban and rural patterns. It originates from a transfer of sensible heat from the urban surface and infrastructure into the ground. It can reveal climatic processes since UHI_{sub} regards the behavior of the heat stored in the terrain over long periods;
- **Surface UHI** (UHI_{surf}): the temperature difference at the atmosphere-ground interface of the city and of the rural regions. It reveals a complex spatial pattern primarily due to the geometry, radiative and thermal properties of surface features, and its magnitude is maximum during clear daytime conditions in low vegetated urban areas;
- **Canopy layer UHI** (UHI_{UCL}): the gradient between the temperature of the air confined in the urban canopy layer (UCL), which is the layer between the urban surface and roof level, and the corresponding height in the near-surface layer of the rural surroundings. Its intensity is greatest after sunset, because air above urban surfaces cools more gradually than in rural ones. In city centre sites with tall buildings and narrow streets, its magnitude is strongest during nighttime, while during daytime UHI_{UCL} is frequently smaller;
- **Boundary layer UHI** (UHI_{UBL}): the temperature difference of the air enclosed between the top of the UCL and the maximum height of the urban boundary layer (UBL), and the height equivalent air in the atmospheric boundary layer of the rural area. It is driven by an intensified sensible heat flux from the city, which supports the mixing in the lower atmosphere during daytime and preserves it at night, producing an UBL warmer than the rural one all over its depth.

To study each type of UHI, different retrieving methods can be adopted to measure or model the distinct processes involved. At this purpose, three notable techniques have been used, namely *in-situ* measurement, remote sensing and numerical modelling. The *in-situ* measurement approach is made up of values estimated by

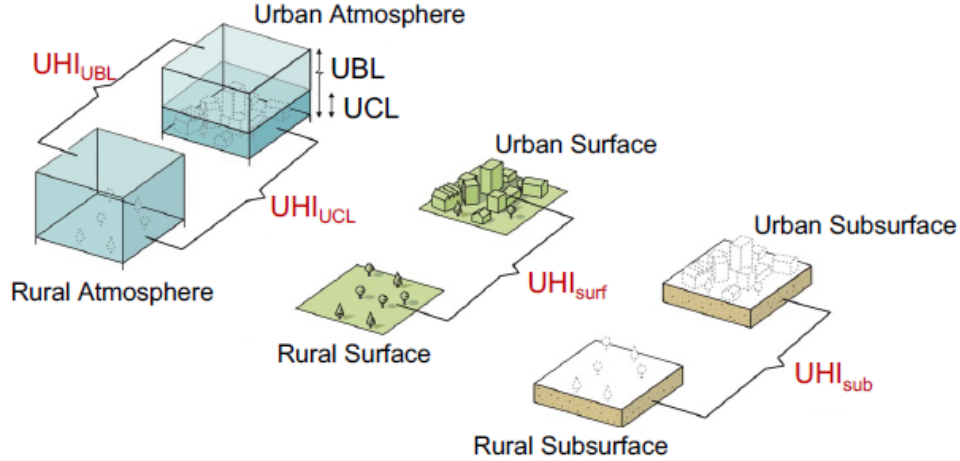


Figure 2.2: Schematic of the temperature differences generating the four types of UHI. From Kong et al. [18].

weather stations, so it can permit direct, instantaneous and continuous measurements of many useful variables such as air temperature, wind speed and humidity. On the other hand, it also exhibits some constraints, in fact the restricted number of stations makes difficult to provide a high spatial resolution of the investigated phenomena. Moreover, it is important to accurately select the most appropriate urban and rural stations to calculate the correct UHI without including spurious effects. Many suggestions and criteria have been dispensed in literature about this, describing methodologies involving land cover, population and satellite night-time brightness index. To overcome the issue of low spatial resolution information provided by the *in-situ* measurements, thermal infrared remote sensing from satellites has been employed for its capability to globally monitor numerous parameters such as land surface temperature, which is extremely used for the study of UHI_{surf} . The most utilized satellite instrument is the Moderate Resolution Imaging Spectroradiometer MODIS (Pagano et al. [19]), which can furnish images almost every day with a spatial resolution of few hundred meters. The main disadvantage of these retrieving methods lies in the fact that they cannot be used to monitor continuous temporal variations of UHI, since they move orbiting around the Earth. Also, the cloud cover may be responsible of alterations in measured data. The necessity to obtain continuous information at high spatial and temporal resolutions has contributed to increase the interest about the modelling approach, which even offers the possibility to assess hypothetical future scenarios. Among the many existing models, the most commonly employed are the Consortium for Small-scale Modeling COSMO (Baldauf et al. [20]), the Community Earth System Model CESM (Hurrell et al. [21]), and especially the Weather Research and Forecasting Model WRF

(Powers et al. [22]). These models can capture temporal–spatial variations caused by urbanization of countless physical quantities, all performing with the same conservation laws but differing in the hydrostatic assumptions, in the formulation of equations and in the parameterization schemes. Typically, these differences must be taken into account choosing appropriate models to properly study specific processes of interest.

2.2.2 Energy Budget of Urban Heat Island

The UHI_{UCL} is the most commonly studied heat island, and the following discussion is specifically referred to this type of phenomenon. As aforementioned, the birth of new urban settlements creates substantial modifications in the conditions of the original environment. For example, the superimposition of a linear and compact topography causes the disruption of air flows, reducing the wind speed and increasing the turbulence. Then, the replacement of the natural soil with building materials and drainage systems changes the local energy and water balances, as well as the extensive generation and release of anthropogenic heat, influencing both the temperature and the humidity and strengthening the convection. Side effects are related to the emission of aerosols and gaseous pollutants, capable of deteriorating air quality by reducing visibility, increasing cloudiness and leading to several respiratory diseases.

According to Oke [23], to model the UHI effect the starting point is to define the different energy balance over a simplified flat rural surface (Figure 2.3(a)) and over the urban ecosystem (Figure 2.3(b)). In the first case, the balance is obtained between the net radiative heat flux Q^* (including both incoming and outgoing long-wave and short-wave), the ground heat flux Q_G (transferring sensible heat to the subsoil by conduction), and the two turbulent heat fluxes exchanging energy between the surface and atmosphere, namely the sensible heat flux Q_H and the latent heat flux Q_E :

$$Q^* = Q_G + Q_H + Q_E \quad (2.1)$$

The warming or cooling of an air layer is directly related to changes in its heat content. Indeed, the impact of heat fluxes on temperature variation in a rural near-surface layer of air can be described by the equation

$$\frac{\partial T}{\partial t} = \frac{\text{div } Q_z^*}{C} - \frac{\text{div}(Q_{Hz} + Q_{Ez})}{C}, \quad (2.2)$$

where C is the heat capacity of air and $\text{div } Q_z^*$ and $\text{div}(Q_{Hz} + Q_{Ez})$ denote the change of net radiation and sensible/latent heat with height in the layer z , and

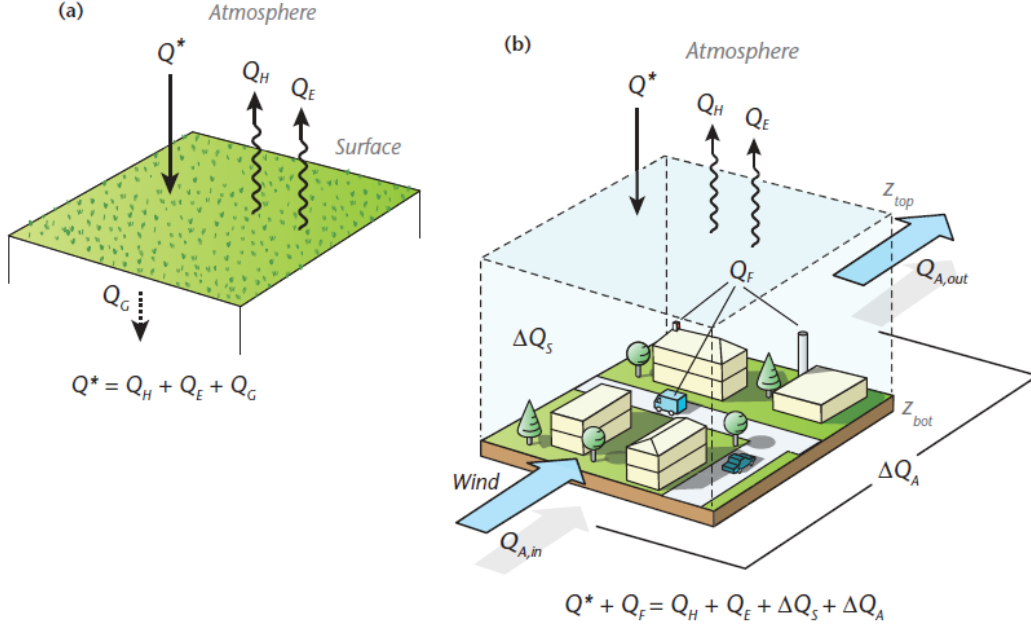


Figure 2.3: Schematic of the fluxes in the surface energy balance of a rural (a) and an urban (b) building-soil-air volume. From Oke [23].

the term relative to Q_G is negligible since it acts only at the surface. Regarding the urban context, it is inadequate to describe separately the energy balance of individual surfaces to provide a characterization of the whole urban area. In this situation, it is recommended to define a conceptual volume, integrating the entire urban ecosystem from the top of the roughness sublayer (the layer immediately adjacent to the surface including roughness elements such as trees or buildings) to a certain depth in the subsoil for which the vertical heat flux by conduction across the bottom is irrelevant over the period of consideration. The surface energy balance for such a control volume is defined by the equation

$$Q^* + Q_F = Q_H + Q_E + \Delta Q_S + \Delta Q_A, \quad (2.3)$$

where additional contribution with respect to the rural energy budget are given by the anthropogenic heat flux Q_F released within the volume due to human activities (e.g. traffic, air conditioners, residencies), by the net stored heat flux ΔQ_S referring to all energy storage mechanisms within the volume (including air, soil, building fabric and trees), and by the net horizontal advective heat flux through the sides of the volume ΔQ_A . In this case, to represent the temperature change in this air volume, it is necessary to use the equation

$$\frac{\partial T}{\partial t} = \frac{\text{div} Q_v^* + Q_{Fv}}{C} - \frac{\text{div}(Q_{Hv} + Q_{Ev})}{C} - \frac{\partial S}{c_p \partial t} - \vec{u} \cdot \vec{\nabla} T, \quad (2.4)$$

where $\text{div } Q_v^* + Q_{Fv}$ and $\text{div}(Q_{Hv} + Q_{Ev})$ are respectively the volumetric divergence of net radiation plus anthropogenic fluxes and of sensible plus latent heat fluxes, c_p is the specific heat of air at constant pressure and the last two terms denote the contributions from heat storage and the advection by the mean wind. Therefore, the origin of UHI_{UCL} lies in the difference between the air temperature in the urban volume and that of a layer at the same height in the rural surroundings. Obviously the anthropogenic heat fluxes are one of the main responsables of temperature increase in urban areas with respect to rural, especially the heat release due to fuel combustion or by "consumption" of electricity for human activities such as heating and cooling of buildings. Also the thermal properties of building materials in urban environments play an important role, often having a higher capacity to store and release sensible heat compared to vegetation and soil. Additionally, the surface moisture-waterproofing caused by buildings and paving reduces soil moisture and surface wetness, with a consequent diminished cooling effect with respect to the high evapotranspiration in densely vegetated rural regions. Regarding radiation, the more polluted urban atmosphere emits higher downward long-wave radiation compared to the rural one, and the closely-spaced buildings characterizing the urban surface geometry generate multiple reflection (greater short-wave absorption) and inhibit the net long-wave loss because of small sky view factors. Finally, the wind sheltering of tall infrastructures reduces the heat losses by convection. All these factors generally result in a positive temperature gradient between urban zones and rural territories, with features depending on the city structures, usually with maximum magnitude after the sunset when air above urban surfaces cools more slowly than air above rural ones, in condition of calm wind.

2.2.3 Impact of Heatwaves on Urban Heat Island

The major impact of heatwaves is definitely the increase of temperature in a certain location with respect to its climatology. Thus, at first glance it could be reasonable to assume that a raise in the background temperature is simply added to that resulting by the UHI effect. Nonetheless, the UHI definition relies on the temperature difference between urban and adjacent rural areas, and its intensity is regulated by the conditions in both kinds of environment, together with the background climate. As aforementioned, the warming of the urban and rural environments is connected to the energy balance, which is governed by numerous drivers such as atmospheric stability, wind speed, air pressure, cloudiness, evapotranspiration, surface albedo, pollution, soil moisture, and so on. Therefore, the impacts of heatwaves on UHI are determined by the urban–rural contrasting feedback to the various drivers and the resultant modifications in the energy budgets. In general, three possible outcomes

have been assessed in the literature:

- **UHI increases** - Considering that heatwaves are characterized by clear sky condition and lower water vapor, the net all-wave radiation is commonly higher with respect to normal conditions, so urban zones gather more radiative energy input than rural ones. Also, the high atmospheric stability during heat waves prolongs stagnant conditions and inhibits the horizontal advective cooling effect, and the presence of tall buildings in densely built urban areas contribute to interrupt the wind flows, lessening the heat removal. Moreover, during heatwaves it is typical to observe an increase in the anthropogenic heat released due to higher air conditioners demand together with a notable increment of heat storage in urban areas (An et al. [24]). Finally, while in urbanized areas the rare vegetation cover and soil moisture minimize the cooling effect of latent heat fluxes by evapotranspiration, in rural regions this process can be enhanced during heatwaves due the higher atmospheric temperature and the better capability of air to absorb water vapor. All these considerations make reasonable to expect a UHI magnitude intensification concurrently with heatwave events;
- **UHI decreases** - The absence of rainfall during heatwaves and the consequent possibility of heatwave–drought co–occurrence must be taken into account (He et al. [25]), possibly generating more severe impacts than the occurrence of individual extremes especially on water scarcity in soils (Jiang et al. [26]). Indeed, poor precipitation produces a decrease in soil wetness reducing the evapotranspiration cooling effect in rural areas whereas the impact on urban temperature is minimum, and UHI can undergo a decrease concurrently with heatwaves (Kumar et al. [27]). Also the advective heat flux can be an important component in UHI diminution, mainly in coastal cities where the urban region is influenced by the advection of humid and cool air from the sea, while a dry and warm advection in rural areas can accelerate the depletion of moisture and latent heat flux;
- **UHI is unaffected** - A restricted number of studies report an unvaried UHI intensity during heatwaves compared to climatological values. This is justified by the fact that the investigated periods show very similar wind features in heatwave and normal conditions, with consequent unaltered urban–rural soil moisture deficit and heat storage. Furthermore, it is important to note that other studies which have concluded that UHI effects remain constant during heatwaves are primarily based on analyses of smaller cities. These cities may not have a sufficiently large thermal capacity or a significant urban-rural soil

moisture gradient to accurately account for any substantial changes in UHI effects during heatwaves.

Chapter 3

Study of Urban Heat Island during Heatwaves in Europe

3.1 Purpose

The assessment about the effect produced on urban heat island by heatwave events is not homogeneous. Indeed, regarding the capability of heatwaves to influence the urban-rural temperature difference, dissimilar outcomes for different locations or heatwave events were retrieved, describing both exacerbations and reductions of urban heat island. Numerous studies examined the interaction between these two phenomena acting at different scales, following various approaches. Employing numerical simulations, many studies assessed the existence of a synergistic behavior producing intensified urban-rural temperature differences in heatwave conditions especially in places located across the USA (Zhao et al. [28], Ramamurthy et al. [29]), also suggesting that added heat stress in cities is higher than the sum of the background UHI and the heatwave effect (Li et al. [30]). Conversely, other numerical studies such as Chew et al. [31] retrieved the absence of a significant synergistic interaction between UHI and heatwaves, even for the USA (Kunke et al. [32]). Another approach involved analyses of observational measurements and was adopted in several studies, addressing different locations and heatwave events. For example, Schatz et al. [33] retrieved an UHI increment in Madison, USA, during summertime heatwaves and similar results were obtained for diverse cities across the globe, such as the metropolitan city of Karachi, Pakistan (Rizvi et al. [34]), Beijing, China (He et al. [35]) and Athens, Greece (Katavoutas et al. [36]), with more remarkable consequences for the nighttime UHI. On the other hand, the investigations about UHI intensity based on observational and reanalysis data during hot temperature extremes in Dijon, France (Richard et al. [37]) and in

Lisbon, Portugal (Oliveira et al. [38]), did not reveal significant synergistic effect of heatwaves on UHI, or even a decrease of UHI values. Variations of UHI behavior were found also inside the same city, as evidenced by a study regarding Shanghai, China (He et al. [39]). In this case, the amplification of UHI during heatwaves was found to depend on localized effects, especially assessing that less urbanized districts were generally more sensitive to this synergy. Not only the features of urban areas, but also different rural backgrounds were proven to be crucial in determining the heatwave-induced UHI augmentation, particularly the rural evapotranspiration cooling effects based on humidity and vegetation type (Miao et al. [40]).

Along these lines, Kong et al. [18] currently reviewed the scientific literature on UHI-heatwave interaction concluding that most examined studies suggest an UHI increase during heatwaves due to a raise in incoming shortwave radiation or to high anthropogenic heat released, although others detect no significant synergy or even a reduction of UHI intensity during heatwaves, motivated by a decreased cooling effect of evapotranspiration due to soil moisture depletion in rural areas. However, the lack of widely accepted multi-scale modelling approaches and the inhomogeneities in data and methodologies adopted blur the picture on UHI-heatwave interaction, raising questions on its robustness and making the comparison through the results of different studies an arduous mission. Several research gaps were identified, in particular highlighting the necessity to investigate multi-year datasets instead of single heatwave events and the importance of considering an ensemble of cities with different characteristics to reveal the large-scale general trend. The present study attempted to fill these gaps for the European continent, refining the methodology used by Scott et al. [41] which investigated a large ensemble of USA cities through *in-situ* meteorological records and observed a reduced UHI intensity during warmer synoptic conditions, a result remarkably in contrast with the majority of studies. Bearing also in mind the different morphology of European and USA cities (Antipova [42]), respectively characterized by abrupt and smooth urban-rural transitions, it was unclear whether European cities behave like those examined by Scott et al. or they follow the dominant paradigm of positive UHI-heatwave correlation. Therefore, the adopted approach was aimed at clarifying this question and at complementing recent existing literature on specific case studies for European cities (e.g. Founda et al. [43], Nicholson [44], Unger et al. [45]), by providing an unprecedented assessment through observational data for Europe about impacts of large-scale features on thermal stress at local scale. In particular, the analyses were addressed at the evaluation of heatwave effects on UHI in European cities over a long record of events adopting an empirical approach, estimating UHI intensity from daily temperature measured by meteorological stations. The focus was particularly on summer nighttime, when

UHI effect is generally more pronounced and dangerous for human health (Wong et al. [46]).

3.2 Methodology

3.2.1 Data Sources for Urban Heat Island Analysis

In this study the meteorological stations data gathered by European Climate Assessment & Dataset ECA&D (Klein Tank et al. [47]) and by World Meteorological Organization network WMO (Bekiashev et al. [10]) were employed. The ECA&D consists of daily records obtained from climatological divisions of National Meteorological and Hydrological Services, together with station series maintained by observatories and research centres across the European continent and the Mediterranean. Following the recommendations of Klok et al. [48], only the series which passed the quality controls and the homogeneity tests were used. Similarly, the selected WMO dataset was the Global Surface Summary Of Day (GSOD) product provided by NOAA’s National Centers for Environmental Information (NCEI), which uses as input the quality controlled Integrated Surface Data ISD (Smith et al. [49]). The two variables extracted from these datasets were daily maximum and minimum temperatures, used to estimate daytime and nighttime UHI, respectively, as in Scott et al. The analysis covered 20 years (from 2000 to 2019) of heatwave events, binding the observational data availability and the length of the dataset, and considering only boreal summers, namely the months of June, July and August, following the suggestions of Rasilla et al. [50] and Stefanon et al. [51].

3.2.2 Urban Heat Island Index

For each city the daily intensity of urban heat island effect was determined by calculating a Composite UHI Index (UHII) as defined in Basara et al. [52] and [53]:

$$UHII = \overline{T_U} - \overline{T_R}, \quad (3.1)$$

where T_U and T_R are the urban and rural temperatures, respectively, and the overline indicates that the values are averaged over all the employed stations. Compared to the original definition based on a couple of observations (Oke [54] and Ackerman [55]), this UHI index was chosen since it allows to reduce the demonstrated impact of site-specific variability for both the urban and rural zones (Hawkins et al [56]).

3.2.3 Method to Select Cities and Weather Stations

The selection of weather stations started from European cities having more than 150,000 inhabitants according to Eurostat [57], keeping only those with available data in ECA&D or WMO repositories. Then, 3 parameters were employed to ensure the uniformity of the analysis and to reduce the heterogeneity of dataset characteristics. In particular:

- 1) the maximum distance D of urban and rural stations from the central point of the city (according to the coordinates provided by Wolfram Knowledgebase [58] and reported in Table 3.1), necessary to circumscribe the surrounding area of the cities and to guarantee a homogeneous analysis among cities with different sizes. Urban stations within a distance $D \leq 10$ km from the city centre were considered, a choice supported by a check on the European Urban Atlas [59] which suggested this value as the average radius of the urban area for analyzed cities. Rural stations were selected at a distance $10 < D \leq 35$ km from the city centre, with an additional control over stations positioned near 10 km to distinguish urban from rural ones. The 35 km threshold was appropriately within the range between 1 and 50 km identified by Li et al. [60], which reviewed studies about effects of rural extent on UHI. This adopted parameter was similar to those employed by Scott et al. to have a solid reference and to enable comparisons with another study focusing on highly populated cities through observational data. For vast cities like Paris or London, the rural stations were adequately chosen to consider the larger size of the urban area. Also, the Copernicus Climate Change Service UHI application (Hooyberghs et al. [61]) was checked for available cities to verify the spatial extension of the UHI effect. Other thresholds like 20 km as in Zhang et al. [62] were tested for maximum rural distance, obtaining unaltered results;
- 2) the maximum height difference $|\Delta H|$ between urban and rural stations, necessary to remove factors such as topography capable of impacting the UHI evaluation. This threshold for altitude was based on Martin-Vide et al. [63], which indicated the rules for correctly selecting the stations to measure UHI removing temperature differences depending on external components such as vertical temperature gradient. The suggested threshold of ± 30 m was modified into ± 70 m to increase the number of stations included and, consequently, the analysis strength. However, to check the reliability of the adapted threshold, sensitivity tests were performed using ± 30 m without noticing significant variations in the results;

3) a check of land cover like in Scott et al., since Ngarambe et al. [64] recommended to select rural areas in terrains surrounded by natural properties, without densely constructed buildings. In this regard, the urban climate dataset provided by Copernicus Climate Change Service C3S (Hooyberghs et al. [61]) and the land cover characteristics furnished by CORINE Land Cover 2018 inventory (CLC [65]) were used. The imposed condition was that urban stations had to present land cover characteristics of urban areas according to the rural-urban mask of C3S based on CLC, also discussed in Schumacher [66]. The CLC method classifies each pixel obtained on satellite images into different land cover classes, as described in the technical report (Berckmans et al. [67]). While the C3S dataset lacked masks for some of the cities analyzed, it was possible to reproduce them for those missing locations based on C3S guidelines. However, it is worth noting that the dataset did not differentiate between urban and suburban areas, and simply classified all non-urban zones as rural. This classification was not extremely refined, as it did not recognize the detail of suburban regions.

List of selected locations					
Location	Latitude	Longitude	Location	Latitude	Longitude
1) Aachen	50.77 N	6.09 E	20) Karlsruhe	49.00 N	8.04 E
2) Amsterdam	52.37 N	4.89 E	21) Leipzig	51.35 N	12.40 E
3) Antwerp	51.22 N	4.42 E	22) Lisbon	38.72 N	9.14 W
4) Athens	37.98 N	23.73 E	23) Ljubljana	46.06 N	14.51 E
5) Berlin	52.52 N	13.38 E	24) London	51.50 N	0.12 W
6) Bologna	44.50 N	11.34 E	25) Madrid	40.42 N	3.71 W
7) Bremen	53.08 N	8.81 E	26) Malmo	55.61 N	13.02 E
8) Brussels	50.83 N	4.33 E	27) Mannheim	49.50 N	8.47 E
9) Budapest	47.51 N	19.08 E	28) Munich	48.14 N	11.58 E
10) Catania	37.50 N	15.08 E	29) Nuremberg	49.45 N	11.05 E
11) Cologne	50.95 N	6.97 E	30) Paris	48.86 N	2.34 E
12) Copenhagen	55.68 N	12.57 E	31) Saarbrucken	49.25 N	6.97 E
13) Dresden	51.05 N	13.74 E	32) Stockholm	59.33 N	18.07 E
14) Dublin	53.33 N	6.25 W	33) Stuttgart	48.79 N	9.19 E
15) Frankfurt	50.12 N	8.68 E	34) Toulouse	43.62 N	1.45 E
16) Goteborg	57.72 N	12.01 E	35) Vienna	48.22 N	16.37 E
17) Hamburg	53.55 N	10.00 E	36) Zagreb	45.80 N	15.97 E
18) Hanover	52.40 N	9.73 E	37) Zurich	47.38 N	8.54 E
19) Helsinki	60.17 N	24.94 E			

Table 3.1: Analyzed cities with information about their locations. *Source:* Wolfram Knowledgebase™[58].

3.2.4 Selection Results

Following the described methodology, a total of 37 suitable cities was identified. The geographical distribution of these cities (Figure 3.1) covers areas with different geographical features of the European continent such as latitude, distance from the sea and altitude.

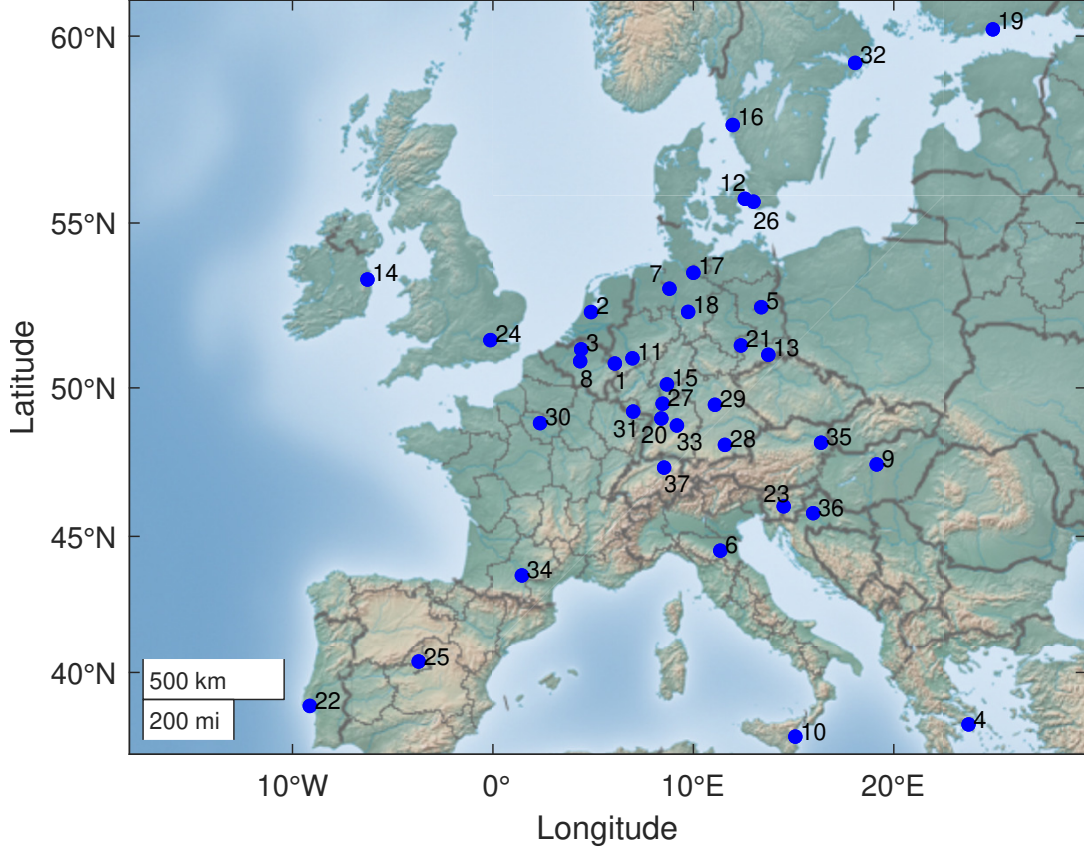


Figure 3.1: Geographical distribution over the European continent of the cities composing the final dataset. The numbers refer to locations reported in Table 3.1.

Figure 3.2 (left) shows the percentage of stations located at different distances D from the city centres, where more than 80% of the stations are placed at a distance $D \leq 8$ km. Rural sites exhibited a homogeneous distribution from $15 \leq D \leq 35$ km, while only a small percentage positioned between 9 and 15 km. Figure 3.3 depicts an example of the spatial distribution of selected stations for the city of Berlin.

Figure 3.2 (right) contains the histogram of rural stations settled at various height difference $|\Delta H|$ from the city centre and shows more than 50% of the stations attending the $|\Delta H| \leq 30$ m of Martin-Vide et al. [63], while the more $|\Delta H|$ increases, the less the number of stations. Despite the abundance of rural stations with $|\Delta H| > 30$ m, the produced temperature difference did not significantly affect the following analysis, which regarded the differences of UHI in presence and absence of heatwaves, when this altitude effect was assumed to act likewise.

3.2.5 Method for Heatwaves Identification

The target of this study was the interaction between phenomena acting at different scales, therefore to detect large-scale heatwave events a distinct dataset with respect to that used for local scale UHI analysis was employed, in order to avoid su-

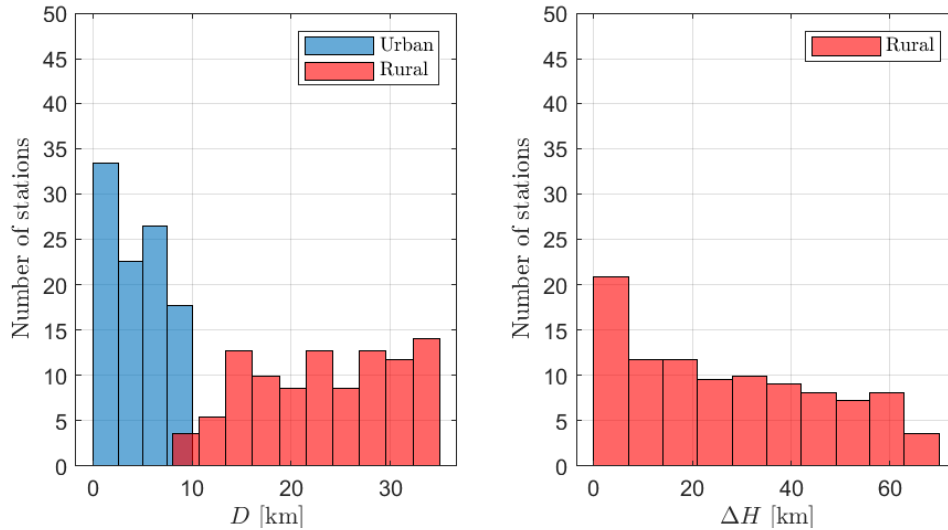


Figure 3.2: Characteristics of meteorological stations employed: on the left histogram of the distance D from city centres of urban (cyan) and rural (red) stations; on the right histogram of the height difference ΔH of rural stations with respect to the city centres.



Figure 3.3: Example of distribution of the selected urban and rural meteorological stations for Berlin, distinguishing ECA&D in green and WMO in blue.

proposing the identification of the two phenomena. To determine the occurrences of heatwaves, the methodology of Stefanon et al. [51] was reproduced, originally based on gridded and multi-year datasets and applied specifically to the European continent. ECMWF Reanalysis 5th Generation (ERA5) dataset (Hersbach et al. [68]) was selected, which combines model results with observations and provides hourly data on atmospheric, land-surface and sea-state parameters on regular latitude-longitude grids at $0.25^\circ \times 0.25^\circ$ resolution, comparable with gridded observational

dataset (Cornes et al. [69]). This dataset was appropriate for this kind of study, as suggested in Rousi et al. [70], also due to its applicability for developing heat-related quality-checked products at local scale (Di Napoli et al. [71] and Berckmans et al. [72]).

The adopted definition of heatwave was mentioned by Perkins [73] as an example of a recent multi-criteria definition since it includes the constraints on spatial and temporal extensions, expressly suitable for detecting large-scale phenomena and useful for removing discontinuous and local events. In detail, for each ERA5 grid-point daily temperature anomalies were evaluated with respect to the 2000-2019 climatology extracted from the ERA5 dataset. Extremely hot days were defined when anomalies exceeded the upper 95th percentile (T_{95}) of the local probability density function, computed for each day d using the 21 days centred moving average ($d - 10$ and $d + 10$) along the 20 summers of temperature data. The choice of the 95th percentile threshold was considered more appropriate than higher thresholds, such as the 99th percentile, which would have excessively reduced the number of detected events and the statistical significance of the analysis. On the other hand, using lower thresholds as the 90th percentile could have allowed to include other than extreme heat events. Each city reference gridpoint was selected as the nearest to the coordinates shown in Table 3.1. To take into account the spatial extension of heatwaves and to avoid considering isolated hot gridpoints, it was required to T_{95} threshold to be overcome in at least 60% of a square of side $L = 1^\circ$, namely a 5×5 gridpoints matrix centred on the city reference gridpoint. If these two criteria were satisfied for at least 3 consecutive days, all days in this time interval were labelled as HeatWave days (HW). All days not considered HW days were defined Normal Summer days (NO) as in Rasilla et al. [50]. To verify the reliability of the results, other heatwave definitions involving different thresholds were examined. In particular, the definitions based on the temperature 90th percentile for 3 days persistence, applied by Herbel et al. [74] and the definition used by Pyrgou et al. [75] based on the 95th percentile but shifting the temporal threshold to 4 days, were tested.

3.2.6 Characteristics of Identified Heatwaves

The methodology presented in Section 3.2.5 identified from 1 to 10 heatwave events for each city (Table 3.2).

Figure 3.4 shows the geographical distribution of heatwave properties across the European cities, highlighting the average heatwave duration and the average intensity. The latter describes the mean large scale temperature anomaly $\overline{T_{AN}}$ during heatwave events. The average heatwave duration for the 37 cities varied between 3 and 6 days, but for 28/37 cities it did not exceed 4 days. The heatwave intensity clas-

Location	Number of HWs	Location	Number of HWs
1) Aachen	7	20) Karlsruhe	7
2) Amsterdam	5	21) Leipzig	4
3) Antwerp	9	22) Lisbon	2
4) Athens	1	23) Ljubljana	5
5) Berlin	5	24) London	6
6) Bologna	3	25) Madrid	9
7) Bremen	7	26) Malmo	2
8) Brussels	10	27) Mannheim	6
9) Budapest	10	28) Munich	7
10) Catania	3	29) Nuremberg	8
11) Cologne	7	30) Paris	6
12) Copenhagen	3	31) Saarbrucken	6
13) Dresden	6	32) Stockholm	5
14) Dublin	2	33) Stuttgart	5
15) Frankfurt	7	34) Toulouse	4
16) Goteborg	3	35) Vienna	8
17) Hamburg	6	36) Zagreb	6
18) Hanover	7	37) Zurich	6
19) Helsinki	1		

Table 3.2: Number of detected heatwaves for each location.

sification presented in Figure 3.4, often employed in marine HW studies (Oliver et al, [76]), showed that 27% and 51% of cities experienced strong and severe intensity events since 2000, respectively.

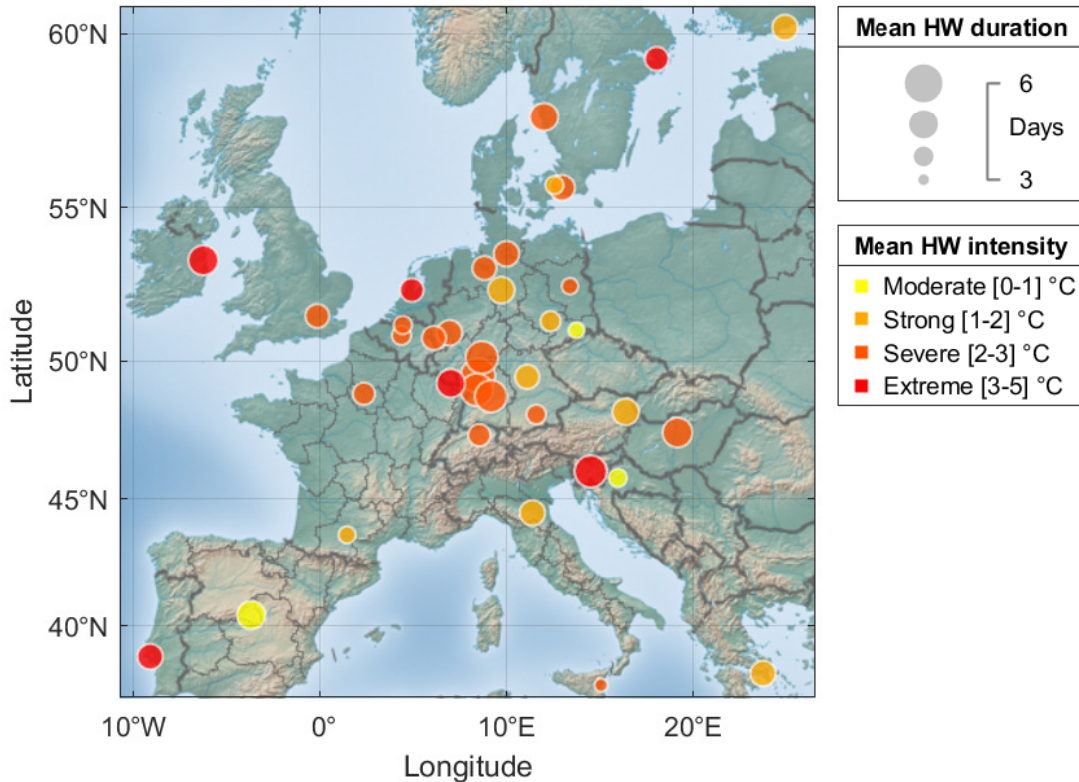


Figure 3.4: Geographic distribution of heatwave features for the analyzed cities: the dot size indicates the average duration [days] of heatwaves detected, while the colour depicts their average intensity.

3.2.7 Methods of Analysis

The first part of the analysis investigated the different behavior of the UHI Index during heatwaves and normal summer conditions from a statistical perspective, by comparing the mean UHII during HW days (\overline{UHII}_{HW}) to the mean UHII during NO days (\overline{UHII}_{NO}), calculating separately the case for nocturnal and for diurnal values. The results for daytime exhibited negligible variations of UHII during HWs, while considerable modifications were retrieved for nighttime UHII, so a detailed analysis was focused on nocturnal UHII. A parametric test to reject the null hypothesis that the two samples belonged to the same distribution was performed using a Welch t-test (Welch [77]), reliable for two unequal sample sizes (Ruxton [78]). To compute the t value, the effective sample size n' estimated as in Wilks [79] was used:

$$n' \cong n \frac{1 - \rho_1}{1 + \rho_1}, \quad (3.2)$$

where n is the initial sample size and ρ_1 is the lag-1 autocorrelation coefficient.

A test was conducted to assess the impact of intra-seasonal temperature variations on UHI in each city. This involved calculating the average intra-seasonal cycle for a period of 20 years and then determining the daily UHII anomaly with respect to the corresponding average intra-seasonal cycle for each city. Subsequently, the characteristics of UHII anomalies obtained from this analysis were compared with those of the previously described UHII. Also the modifications in frequency of positive UHII days during NO and HW were investigated, with the purpose to recognize if the variations of mean UHII were only due to the alteration of UHII values or they were also provoked by a modification of the percentage of days subjected to the UHI effect. An analysis taking into account the local features regarding the selected cities and related meteorological stations was conducted, involving the average altitude of the urban area, the population (associated to the city size), the geographical position, the influence of the sea/ocean, the distance and the height differences between urban and rural stations. In particular, the Pearson correlation among UHII and these characteristics was explored. In addition, a specific analysis was addressed to evaluate the influence of the morphology of the area surrounding the urban stations, following the well-established local climate zone (LCZ) classification (Stewart [80]). The LCZs are properly defined as zones of uniform surface cover, structure, material, and human activity ranging from hundreds of meters to several kilometers in the horizontal scale. The characteristic temperature regime of each LCZ is connected with the homogeneous ecosystems of cities (e.g., parks, commercial cores), natural biomes (e.g., forests, deserts), and agricultural lands. The LCZs are distinguished according to the height and packing of roughness objects or

the prevailing land cover, and they are usually separated in 17 standard classes (see Figure 3.5). The common set is divided into *built types* 1–10, and *land cover types* A–G, where built types consist of constructed features on a predominant land cover which is generally *paved* or *low plants/scattered trees* respectively for compact and for open regions.

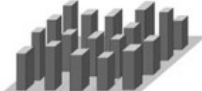
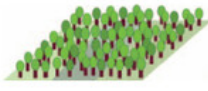



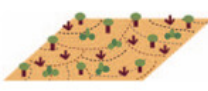






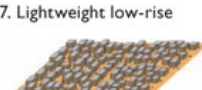




Built types	Definition	Land cover types	Definition
 <p>1. Compact high-rise</p>	Dense mix of tall buildings to tens of stories. Few or no trees. Land cover mostly paved. Concrete, steel, stone, and glass construction materials.	 <p>A. Dense trees</p>	Heavily wooded landscape of deciduous and/or evergreen trees. Land cover mostly pervious (low plants). Zone function is natural forest, tree cultivation, or urban park.
 <p>2. Compact midrise</p>	Dense mix of midrise buildings (3–9 stories). Few or no trees. Land cover mostly paved. Stone, brick, tile, and concrete construction materials.	 <p>B. Scattered trees</p>	Lightly wooded landscape of deciduous and/or evergreen trees. Land cover mostly pervious (low plants). Zone function is natural forest, tree cultivation, or urban park.
 <p>3. Compact low-rise</p>	Dense mix of low-rise buildings (1–3 stories). Few or no trees. Land cover mostly paved. Stone, brick, tile, and concrete construction materials.	 <p>C. Bush, scrub</p>	Open arrangement of bushes, shrubs, and short, woody trees. Land cover mostly pervious (bare soil or sand). Zone function is natural scrubland or agriculture.
 <p>4. Open high-rise</p>	Open arrangement of tall buildings to tens of stories. Abundance of pervious land cover (low plants, scattered trees). Concrete, steel, stone, and glass construction materials.	 <p>D. Low plants</p>	Featureless landscape of grass or herbaceous plants/crops. Few or no trees. Zone function is natural grassland, agriculture, or urban park.
 <p>5. Open midrise</p>	Open arrangement of midrise buildings (3–9 stories). Abundance of pervious land cover (low plants, scattered trees). Concrete, steel, stone, and glass construction materials.	 <p>E. Bare rock or paved</p>	Featureless landscape of rock or paved cover. Few or no trees or plants. Zone function is natural desert (rock) or urban transportation.
 <p>6. Open low-rise</p>	Open arrangement of low-rise buildings (1–3 stories). Abundance of pervious land cover (low plants, scattered trees). Wood, brick, stone, tile, and concrete construction materials.	 <p>F. Bare soil or sand</p>	Featureless landscape of soil or sand cover. Few or no trees or plants. Zone function is natural desert or agriculture.
 <p>7. Lightweight low-rise</p>	Dense mix of single-story buildings. Few or no trees. Land cover mostly hard-packed. Lightweight construction materials (e.g., wood, thatch, corrugated metal).	 <p>G. Water</p>	Large, open water bodies such as seas and lakes, or small bodies such as rivers, reservoirs, and lagoons.
 <p>8. Large low-rise</p>	Open arrangement of large low-rise buildings (1–3 stories). Few or no trees. Land cover mostly paved. Steel, concrete, metal, and stone construction materials.	VARIABLE LAND COVER PROPERTIES	
 <p>9. Sparsely built</p>	Sparse arrangement of small or medium-sized buildings in a natural setting. Abundance of pervious land cover (low plants, scattered trees).	<p>b. bare trees</p>	Leafless deciduous trees (e.g., winter). Increased sky view factor. Reduced albedo.
 <p>10. Heavy industry</p>	Low-rise and midrise industrial structures (towers, tanks, stacks). Few or no trees. Land cover mostly paved or hard-packed. Metal, steel, and concrete construction materials.	<p>s. snow cover</p>	Snow cover >10 cm in depth. Low admittance. High albedo.
		<p>d. dry ground</p>	Parched soil. Low admittance. Large Bowen ratio. Increased albedo.
		<p>w. wet ground</p>	Waterlogged soil. High admittance. Small Bowen ratio. Reduced albedo.

Figure 3.5: Building and land cover types according to the LCZ classification system. From Stewart et al. [81].

For this study, the European LCZ map from Demuzere et al. [82] was employed, which was created at a 100 m spatial resolution by experts in LCZ class labels through the use of multiple earth observation datasets. After identifying the appropriate LCZ for every urban station considered in the final dataset, a statistical examination regarding the potential impact of LCZ on the UHI modification during heatwave condition was performed.

Moreover, the possible dependence of the results on the Köppen-Geiger climate zone (Geiger [83]) was investigated. The Köppen-Geiger system organizes climate into 5 main categories (*A tropical*, *B arid*, *C temperate*, *D continental*, and *E polar*) and all climates except for those belonging to the polar group are divided into subgroups depending on the seasonal precipitation patterns (the second letter) and on temperature features (the third letter), establishing a total of 30 sub-types based on different threshold values (see Figure 3.6).

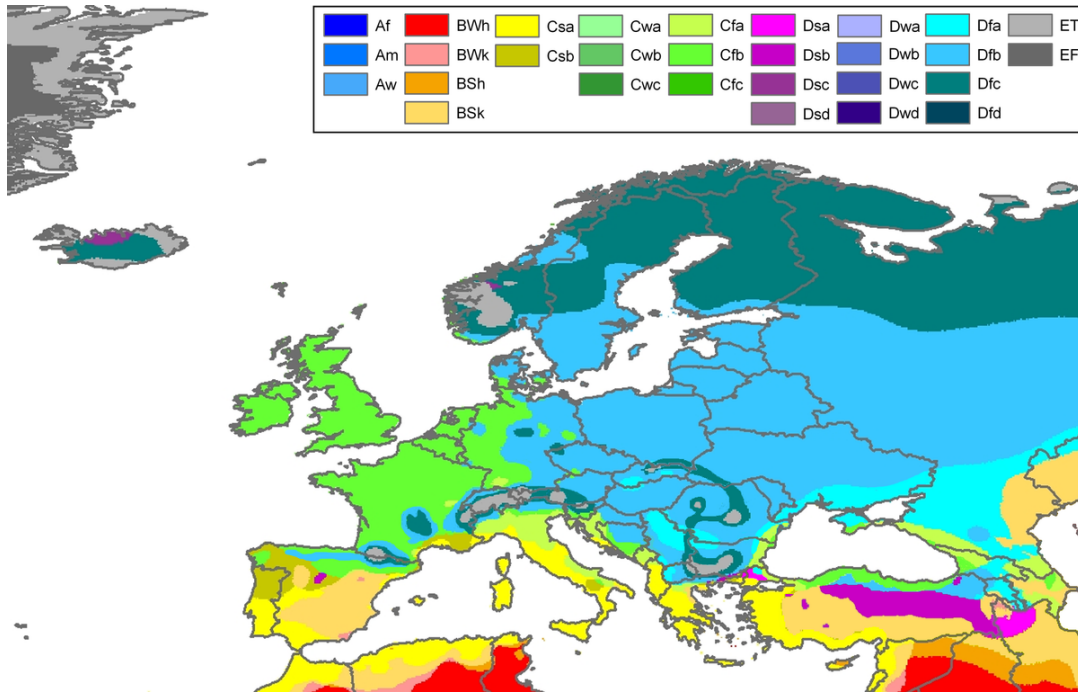


Figure 3.6: Köppen-Geiger climate zones map of Europe, which involves 29 of the different sub-types. From Peel et al. [84].

The re-analyzed Köppen-Geiger map with the high resolution of 5 arc minutes using the downscaling algorithms described by Rubel et al. [85] was employed to observe the climate zone of each considered city, and the UHII variations during heatwave days were examined distinguishing the Köppen-Geiger climate classes.

The second part of the study concerned the UHII temporal evolution during heatwave occurrences, also in relation to the behavior of large scale temperature anomaly T_{AN} computed with respect to T_{95} . This analysis was inspired by Scott et al. and the aim was to analyze the heatwave impacts on UHI more in detail with

respect to the statistical investigation, observing shapes and possible shifts of the signals. The focus was to examine the peak of UHI with respect to the maximum intensity of the heatwave, and the behavior of UHI few days before and after the heatwave occurrence. A standardization of UHI, urban/rural temperatures and T_{AN} by their climatological values (considering the period 2000-2019) was performed. In particular, urban and rural temperature data (and their ΔT) relative to the same lag day i with respect to heatwave onset were averaged over the number of heatwaves for each city, obtaining a mean value T_i . Then, these mean values were standardized to scale the UHI modifications according to the different city features. The standardized temperature \widetilde{T}_i referring to lag day i was calculated for every city as

$$\widetilde{T}_i = \frac{T_i - \overline{T}}{\sigma_{T_i}}, \quad (3.3)$$

where σ_{T_i} was the T_i -related standard deviation, and \overline{T} was the 20 years climatological value, including both HW and NO days. To identify possible temperature spikes, a test through a moving average was accomplished: the temperature values of each HW day d were determined by calculating the mean of the interval between $d - n \cdot r_{HW}$ and $d + n \cdot r_{HW}$, where r_{HW} was the heatwave duration and n was an integer set equal to 1,2 or 3, and then the results were compared to those previously obtained.

The last part of the study was addressed at the evaluation of linear correlation among different variables. The objective was to better understand the motivation behind the variation of UHI during heatwaves and to compare the outcomes with those of Scott et al. Specifically, the analysis consisted of evaluating the slope m of the linear regressions

$$T_x = m \cdot T_y + c, \quad (3.4)$$

where T_x and T_y stand for the different combinations of \widetilde{T}_U , \widetilde{T}_R and \widetilde{T}_A , the latter defined as the standardized environmental average temperature $(T_U + T_R)/2$, useful to provide information about the conditions of the entire city area. Finally, the relationship between UHI and temperature anomaly T_{AN} intensities was calculated, to assess the features of the correlation between these types of local and large-scale phenomena.

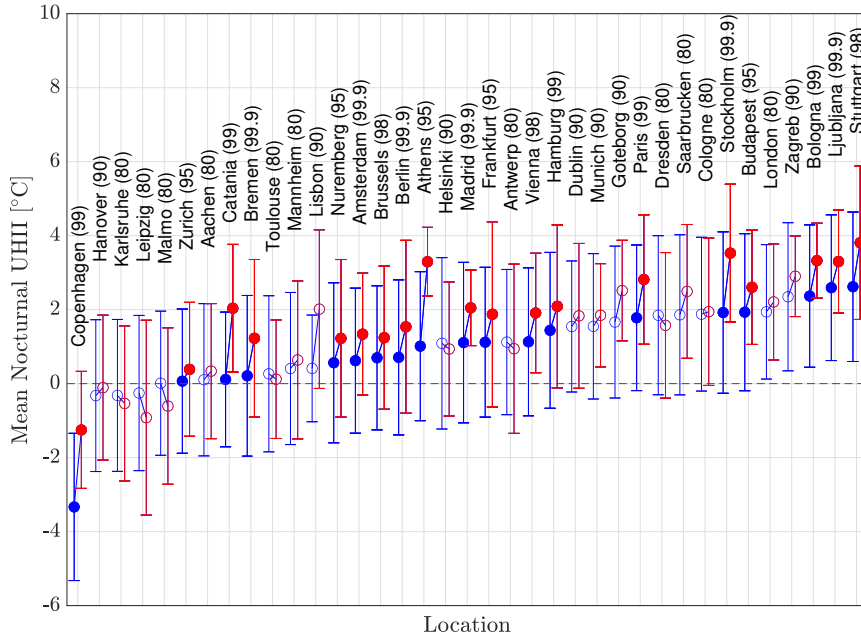
3.3 Results and Discussion

3.3.1 Statistical Analysis

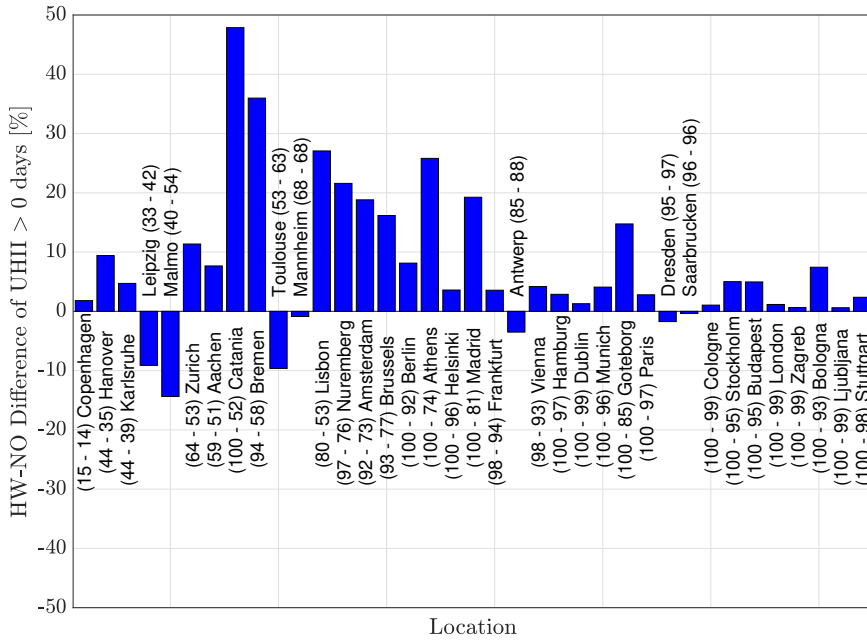
The statistical behavior of urban heat island during NO days and HW days for the 37 selected cities was analyzed. Despite the results for daytime urban heat island revealed negligible variations of \overline{UHII} during HW days compared to NO days, assessing the absence of a synergistic influence of large-scale features on urban climate, on the contrary substantial modifications were observed regarding nighttime. Therefore, the in-depth analysis was addressed specifically to nocturnal values. Figure 3.7(a) shows nocturnal \overline{UHII}_{NO} and \overline{UHII}_{HW} values with the corresponding standard deviation for each city, computed averaging respectively over NO and HW days for the 20 summer period. The cities are sorted by the magnitude of \overline{UHII}_{NO} , where some of them presented negative values, indicating that the adopted methodology did not sample the UHI effect for a subset of cities. However, excluding not statistically significant results, only Copenhagen exhibited $\overline{UHII} < 0$ values.

Focusing on the subset of 32 cities where a positive \overline{UHII}_{NO} was retrieved, it is possible to notice that for 28 out of 32 the \overline{UHII} increased during heatwave days. The intensification was on average $0.7\text{ }^{\circ}\text{C}$ (roughly 50% of the average magnitude of \overline{UHII}_{NO}). The Welch t-test revealed that 18 out of 28 cities presenting \overline{UHII} increment provided statistically significant results with a confidence level $p = 0.05$, while 10/28 did not ($p \geq 0.2$). Moreover, the test described in Section 3.2.7 regarding the potential influence of intra-seasonality established that \overline{UHII} values did not depend on intra-seasonal variability. Indeed, the comparison between the intra-seasonal cycle daily anomaly of \overline{UHII} with respect to the \overline{UHII} previously computed produced negligible variations.

Figure 3.7(b) shows the HW-NO percentage difference of days with positive UHII values. Here, 25 of the 32 cities with $\overline{UHII}_{NO} > 0$ exhibited an increase in percentage, and 18/25 were statistically significant. The amplification of \overline{UHII} and percentage of days appeared slightly linearly correlated, in fact the Pearson correlation coefficient was estimated about 0.5. This Figure was helpful to understand the contribution of $UHII > 0$ frequency to the intensification during heatwaves. In particular, in Figure 3.7(b) it is possible to distinguish 3 groups with different behaviors. The left side of the graph (from Copenhagen to Toulouse) contains cities having negative or zero \overline{UHII}_{NO} and irregular variations in the percentage. The central area (with few exceptions as Mannheim) includes locations exhibiting relatively small \overline{UHII}_{NO} values, but $UHII_{NO} > 0$ percentage undergoing large increment for days with $UHII_{HW} > 0$, meaning that UHI exacerbation was due to



(a)



(b)

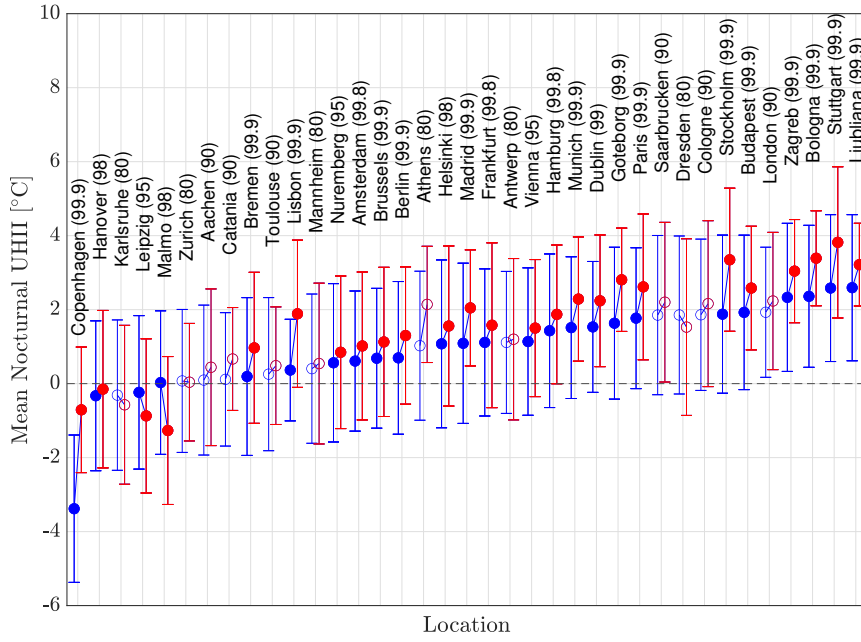
Figure 3.7: (a) Mean and standard deviation of nighttime UHII values for each analyzed city (blue dots indicate $UHII_{NO}$ and red dots $UHII_{HW}$). The numbers between parentheses represent the statistical significance, and filled dots refer to results with significance $> 95\%$. (b) Difference between HW and NO of the percentage of days with positive UHII. The numbers between parenthesis are the percentages during HW and NO.

a higher frequency of positive UHI nights. The right side (from Frankfurt onward) shows cities presenting high \overline{UHII}_{NO} values, and a $UHII_{NO} > 0$ percentage close to 100% which did not experience substantial modifications during heatwaves, suggesting that the primary cause of UHI exacerbation were larger UHII values, rather than higher frequency of $UHII > 0$ days.

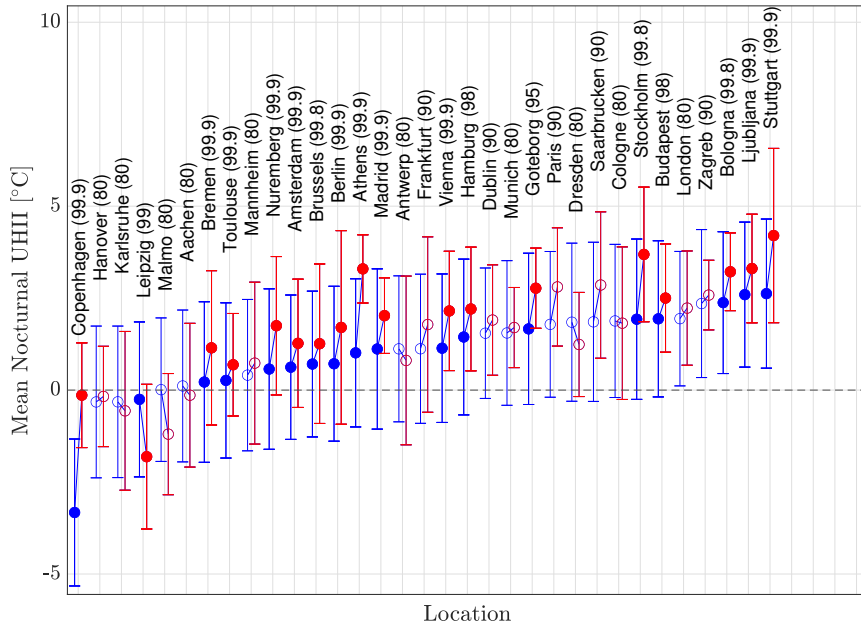
To observe the impact of different heatwave definitions on the obtained results, the analysis of Figure 3.7(a) was reproduced modifying the temperature and duration thresholds in heatwave detection (as Herbel et al. and Pyrgou et al.). Observing Figure 3.8, the outcomes showed slightly different results, e.g. in Figure 3.8(b) there are 4 missing locations due to the more restrictive heatwave definition, but the behavior was the same retrieved with the adopted Stefanon et al. methodology for all the statistically significant cities. Indeed, the obtained results confirmed the increment of nocturnal UHII for all significant locations with positive \overline{UHII}_{NO} , assessing the independence of the analysis from heatwave definition.

The characteristics of selected cities and stations were analyzed to detect common features between locations showing similar changes in the \overline{UHII} between HW and NO days. Linear Pearson correlations between UHII values and several variables were calculated, including urban altitude, population, latitude, longitude, distance from the sea, urban-rural stations $|\Delta H|$ and urban-rural stations distance D (Figure 3.9). Nonetheless, no significant correlations were retrieved (Pearson coefficient always smaller than $|0.36|$). Small correlation between UHII and urban-rural stations ΔH confirmed the possibility to extend the $\Delta H \leq 30$ m threshold proposed by Martin-Vide et al. without noticeably affecting the analysis. Also the poor correlation between the computed UHII and the urban-rural station distance D suggested the possibility to modify this parameter without impacting the results.

The analysis regarding the contribution of different LCZs to the variation of UHI during heatwave periods began with the identification of the LCZ classes for the urban stations considered in the dataset. In this regard, it is important to note that only 7 out of the 17 total LCZ classes were involved. In particular, as concerns the built types, LCZ2 *compact mid-rise*, LCZ3 *compact low-rise*, LCZ5 *open mid-rise*, LCZ6 *open low-rise*, LCZ8 *large low-rise* were included, while the two land cover types LCZA *dense trees* and LCZB *scattered trees* were combined into a new LCZP class (following the definition of Zong et al. [86]), which referred to the stations placed inside urban parks regardless of the density of vegetation. In order to isolate the individual contribution of different LCZs, a nocturnal UHII was computed for every single urban station as the difference between the temperature measured by that urban station and the average rural temperatures, namely



(a)



(b)

Figure 3.8: Similar to Figure 3.7(a), sensitivity tests modifying the definition of heat-wave: (a) Definition based on the temperature 90th percentile and the 3 days persistence thresholds, as Herbel et al. (b) Definition based on the temperature 95th percentile and the 4 days persistence thresholds, as Pyrgou et al.

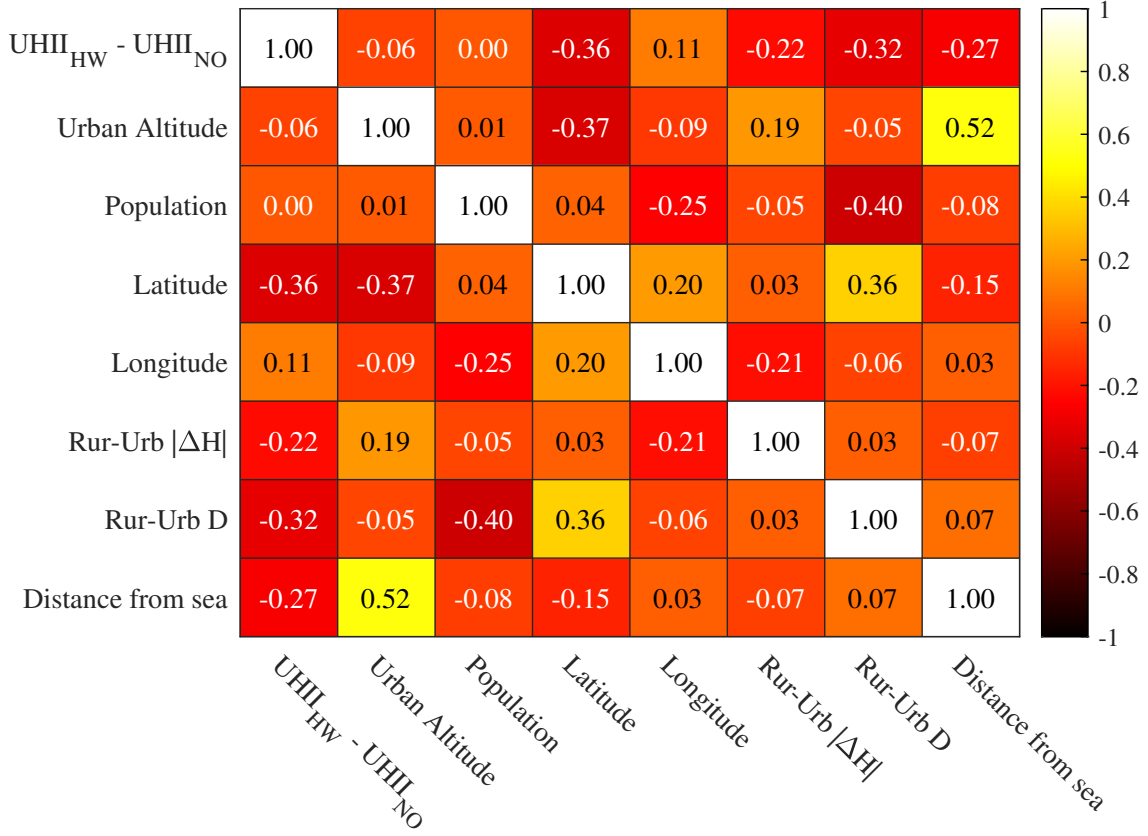


Figure 3.9: Heatmap of correlations among the characteristics of the analyzed cities.

$$UHII_{LCZ} = T_U - \overline{T_R}. \quad (3.5)$$

The $UHII_{LCZ}$ was calculated distinguishing HW and NO days, and Figure 3.10 shows the distribution of the average UHII variation over the 20 years period of data for each urban station, grouping the results based on the LCZ.

The morphology of areas enclosing urban stations appeared to slightly impact the behavior of UHI during heatwaves. Although the mean values of $UHII_{HW} - UHII_{NO}$ resulted similar among the LCZs (ranging from 0.4 to 0.9 °C), by observing the distribution of values it was noticeable how LCZ2, associated with the highest density of midrise buildings, exhibited a more exacerbated UHII difference between HW and NO periods than other LCZs. This was in agreement with other studies related to Asian cities such as Ngarambe et al. [64] and Tian et al. [87], and it was due to the larger capacity of concrete and steel in LCZ2 to store heat in the urban canopy layer during the day and then releasing it at nighttime to warm the environment. LCZ3, LCZ5 and LCZ6 showed comparable outcomes, while $UHII_{HW} - UHII_{NO}$ values related to LCZ8 described a small increment. Moreover, no substantial mitigation effect on the UHI phenomenon was generated by the predominantly vegetated land cover of LCZP, reporting similar values to the built type classes.

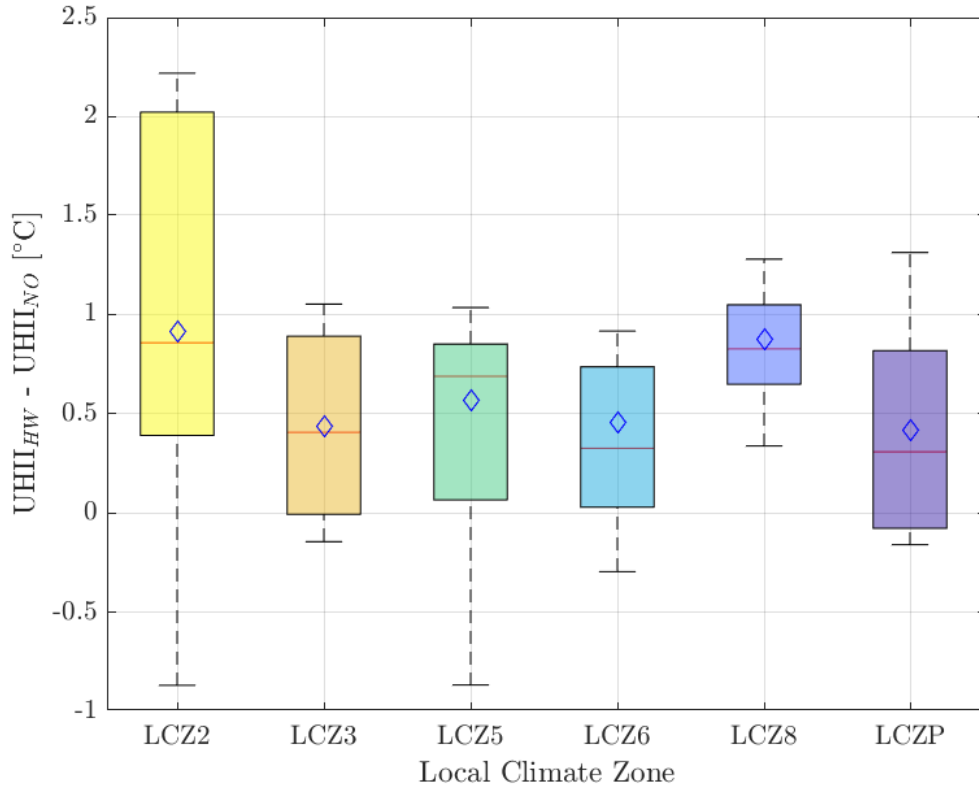


Figure 3.10: Distribution of the average UHII variation during HW and NO days for the various LCZs of the analyzed cities. The blue diamonds show the mean value for each LCZ, the red lines represent the median, while the bottom and top edges of the boxes indicate the 25th and 75th percentiles, respectively.

The investigation about the dependence of UHII values on the Köppen-Geiger classification started with the identification of the appropriate climate zone for each selected city. A low variability of climate zones was found, in fact 35 out of 37 cities belonged to the temperate macro-class, in particular 30 to *temperate oceanic climate* CFB, 4 to *hot-summer Mediterranean climate* CSA and 1 to *humid subtropical climate* CFA, and for 2 the macro-class was continental (*warm-summer humid continental climate* DFB). The UHII variations during HW days distinguishing the 4 categories of climate zones were examined (Figure 3.11).

Although almost all the selected cities belonged to the same CFB class, they exhibited different behaviors, with values of UHII modification ranging from negative to highly positive. It was therefore difficult to retrieve a common feature depending on the climate zone. Only the CSA class revealed similar outcomes, showing a substantial increase in all 4 cities involved. However, the statistics were too poor to make solid assessments and to retrieve reasonably exhaustive conclusions. The results were also compared to those retrieved by Scott et al. for USA cities, with the purpose to search for common or contrasting features depending on climate zones.

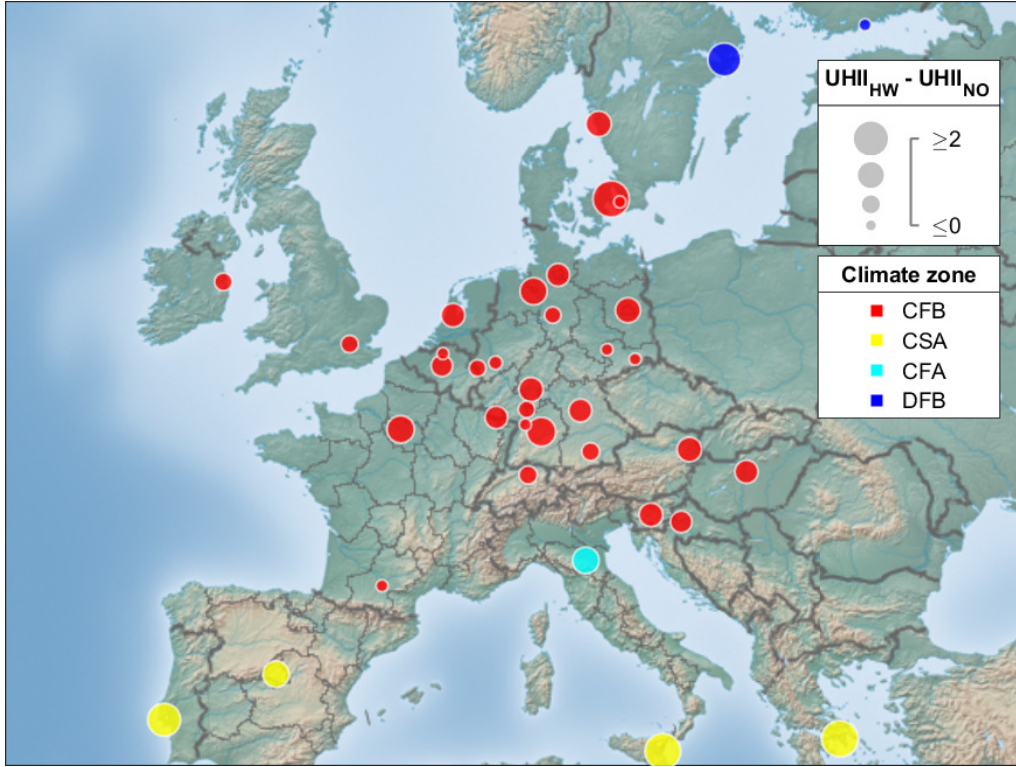


Figure 3.11: Geographic distribution of $\overline{UHII_{HW}} - \overline{UHII_{NO}}$ difference for all the analyzed cities. The colors represent the 4 Köppen-Geiger categories involved.

In this regard, the geographic distribution of values of temperature variations ΔT during heat days provided by their study was observed. Even in their case the outcomes did not demonstrate a clear dependence on the climate zone, because each region of USA exhibited significantly different ΔT values. For example, the North-West continental climate area showed both positive and negative ΔT even in adjacent locations. Only the West Coast, belonging to the temperate climate zone (mostly CSA and CSB categories), revealed a common behavior (except one city) with considerably negative ΔT . This was remarkably in contrast with the results of the present study for European cities corresponding to temperate climate zones.

3.3.2 Temporal Evolution

After the study about the statistical \overline{UHII} variations between NO and HW periods, the temporal evolution of nighttime temperatures and UHII during heatwave events was analyzed. Figure 3.12 depicts the results obtained for urban and rural temperature standardized as described in Section 3.2.7 and their ΔT (representing the urban heat island) from 10 days before to 14 days after the first day of heatwave occurrence, retrieved by averaging over the 32 cities with a positive $\overline{UHII_{NO}}$.

Both urban and rural temperature (Figures 3.12(a) and 3.12(b)) showed a sym-

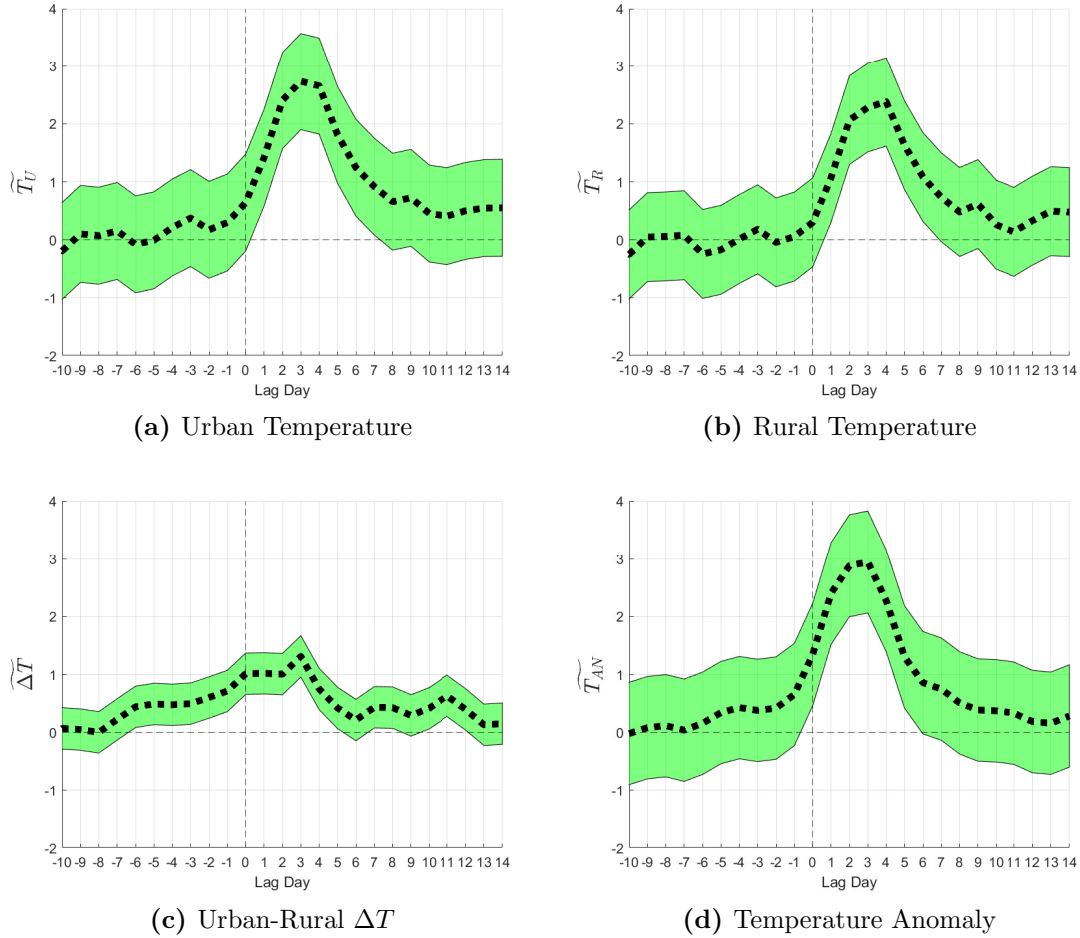


Figure 3.12: Temporal evolution during heatwave events averaged over the selected cities: (a) the standardized urban temperature, (b) the standardized rural temperature, (c) the standardized urban-rural ΔT and (d) the standardized large-scale temperature anomaly with respect to T_{95} . The black dashed lines represent the mean value obtained averaging on cities which exhibit positive UHI effect, while the green area is the standard deviation.

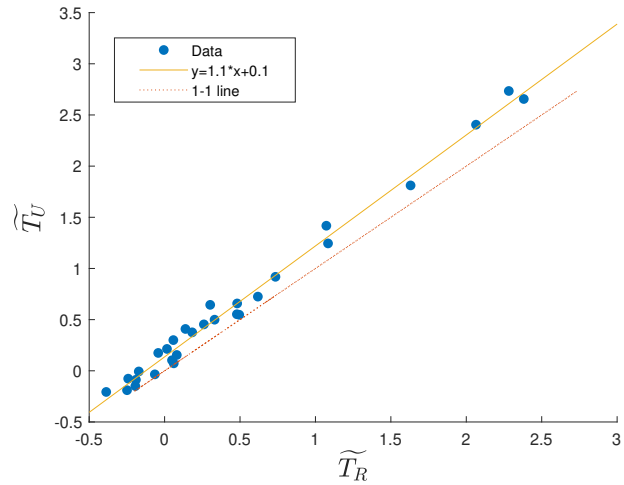
metrical evolution, gradually increasing from day 0, reaching the peak around day 3-4 and then diminishing, but with significant differences. Noticeably relevant was the discrepancy between the two maximum values of T_U and T_R , indicating that a few days after the heatwave occurrence the urban temperature tended to amplify more than rural temperature, reaching higher absolute values. Observing the trend of the two curves before and after the peaks, it is also evident that urban temperature began to grow before the rural, even a few days before the development of the heatwave, and then it required more days to stabilize around the climatological mean. These curves were also reproduced modifying the temporal definition of heatwave, extending the 3 days threshold to 4 and 5 days. The asymmetric behavior of UHI was confirmed, so the results were found to be qualitatively independent

from the methodology. The evolution of standardized mean urban-rural ΔT (Figure 3.12(c)) confirmed the intensification of UHI during HW days, with an evident growth starting before the heatwave onset and reaching its maximum 3 days after day 0. To quantify the possible impact of anomalous spikes in temperature values, the test through running average described in Section 3.2.7 was conducted. Even with these modifications, the results demonstrated a similar behavior as that in Figure 3.12(c), describing an amplification in UHI few days before the onset of the heatwave. This asynchronicity between the evolution of the HW and its imprint on the UHI was also retrieved in Richard et al. [37], where maximum UHI occurred before or during the first few days of extreme warm weather, and they used it to prove the absence of temporal correlation between UHI and heatwaves. However, in this study Figure 3.12(d) allowed to put this result in a different context, representing the standardized mean large scale T_{AN} during HW periods. Here, it is notable that the raise of ΔT began simultaneously with the increase in T_{AN} , namely almost a week before the heatwave onset. Then, during the first days of heatwave, when the maximum values of temperature anomaly were reached, also the UHI-related ΔT experienced an enhancement.

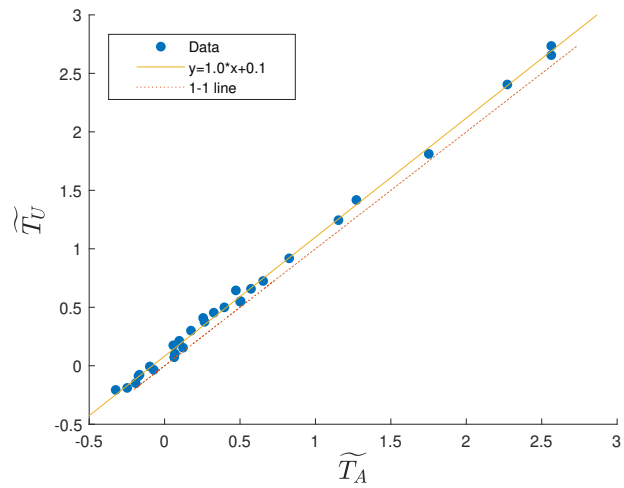
3.3.3 Correlation Analysis

To facilitate the comparison with Scott et al., the correlations between \widetilde{T}_U , \widetilde{T}_R and the environmental temperature \widetilde{T}_A were calculated. Figure 3.13 shows the linear regressions between these three quantities referring to the time interval ranging from 10 days before to 14 days after the heatwave onset, considering the mean values for each of the 32 cities with a positive \overline{UHII}_{NO} . The obtained slope greater than 1 in Figure 3.13(a), indicating that \widetilde{T}_U increased more than \widetilde{T}_R during warmer conditions, confirmed for this study the exacerbation of UHI during heatwave events, contrarily to Scott et al. Moreover, Figures 3.13(b) and 3.13(c) were useful to evaluate the role played by the different variables involved. In particular, the results showed that while urban temperatures warmed at the same rate as environmental temperatures (slope $m = 1$ for the regression between \widetilde{T}_U and \widetilde{T}_A), rural temperature increased at a slower rate (slope $m < 1$ for the regression between \widetilde{T}_R and \widetilde{T}_A). From this analysis emerged that UHI intensified under heatwave conditions due to different response of rural areas with respect to urban zones, the former being more resistant to heating than the latter. Although the results appeared in contrast with those reported by Scott et al., it is important to mention that their study referred to generally warm meteorological conditions, regardless of the occurrence of heatwave events.

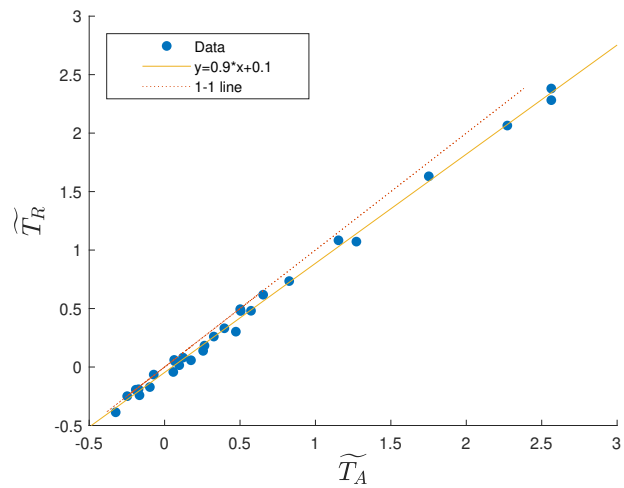
The analysis of the relationship between large-scale temperature anomalies and



(a)



(b)



(c)

Figure 3.13: Linear regressions between standardized mean temperatures during heat-waves: (a) T_U versus T_R , (b) T_U versus T_A and (c) T_R versus T_A .

local scale UHI revealed a smooth and continuous correlation, but a large variability. In particular, Figure 3.14 shows a binned scatter plot between large scale T_{AN} and nighttime urban-rural ΔT including all data during both NO and HW days for the 32 cities with $UHII_{NO} > 0$. The black dots concern HW days exhibiting the peak of UHI averaged for each city.

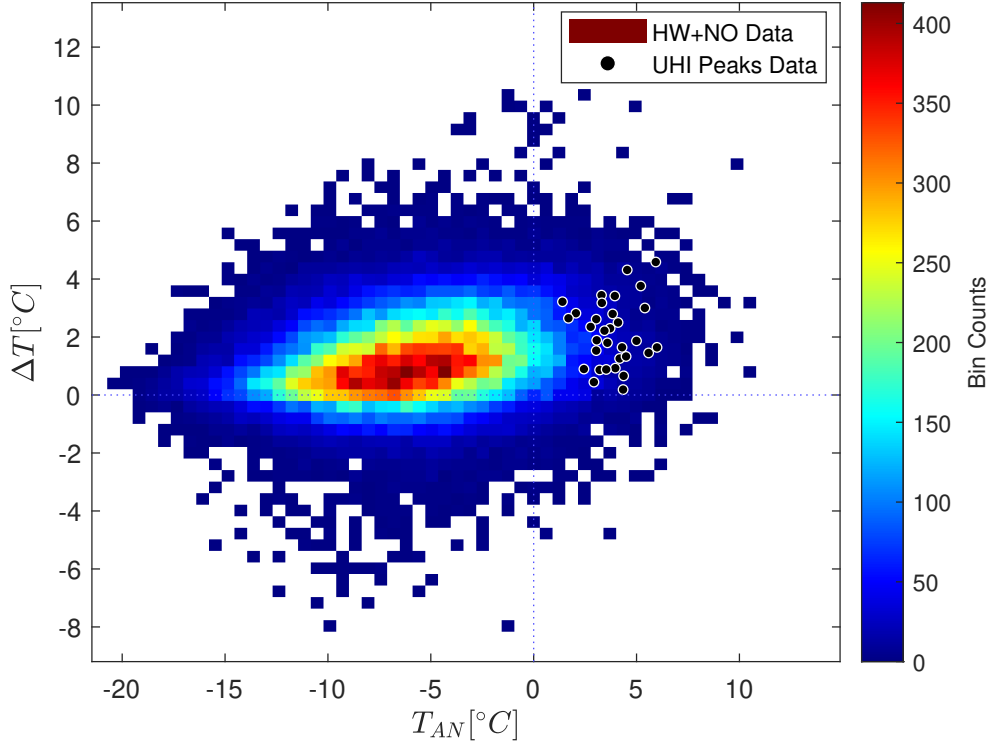


Figure 3.14: Binned scatter plot between large scale T_{AN} computed with respect to T_{95} and nocturnal urban-rural ΔT , including all data during both NO and HW days relative to 32 cities with $UHII_{NO} > 0$. Each black dot refers to HW days showing the maximum UHI values for a single city, averaged over the total number of heatwaves.

An increasing trend of ΔT with growing temperature was noticeable, verifying that UHI effect was exacerbated depending on temperature intensity. However, the lack of a threshold behavior in this relationship suggested that large-scale temperature variability could affect UHI at local scale not only during extreme events. The black dots revealed that the UHI peaks of $\sim 2^\circ C$ lied in a range around $T_{AN} = 4^\circ C$, but the highest values of UHI were found for lower values of T_{AN} (about $0^\circ C$). This indicated that the behavior of UHI was partially linked not only to temperature magnitude, but also to the duration of extreme heat conditions. In fact the greatest ΔT regarded even NO conditions, events not sufficiently hot or prolonged to be considered heatwaves. Moreover, an almost symmetrical behavior of UHI minima and maxima at $T_{AN} = -10^\circ C$ and $0^\circ C$ is observable.

3.4 Comparison with UrbClim Model Products

3.4.1 The UrbClim Model

The UrbClim model (De Ridder et al. [88]) was developed to scale large-scale meteorological conditions down to local scale and to retrieve the influence of urban topography on the weather parameters. It is composed of a land surface scheme describing the physics of energy and water exchange between the soil and the atmosphere in a urban area, coupled to a 3D atmospheric boundary layer module. The urbanization is accomplished by expressing the urban surface as a rough impermeable slab, with opportune values for the albedo, emissivity, thermal conductivity and volumetric heat capacity. Every surface grid cell is considered composed of a mixture of vegetation, bare soil and urban land cover, each type of land cover having a distinct energy/water balance. Moreover, the model takes into account the information about anthropogenic heating in urban grid cells. This surface scheme generates as outputs the turbulent fluxes of sensible and latent heat and momentum, which are then required as lower boundary conditions for the atmospheric boundary layer module. This module consists in a simple 3D model of the lower atmosphere, including the atmospheric boundary layer with an extension of a few kilometers altitude which describes the conservation equations for horizontal momentum, potential temperature, specific humidity and mass, while the pressure field is provided by the large-scale driving model. The atmospheric conservation equations are solved through a finite difference scheme, while the surface fluxes are generated by the land surface scheme, and the top values are interpolated from the large-scale driving model. Despite the primitiveness of some of its calculation procedures, UrbClim is proven to be of the same level of accuracy as more refined models, and it requires an inferior computational cost than high-resolution mesoscale climate models making it suitable for long time integrations. Generating hourly outputs at high spatial resolution (100 m), the model has been subjected to extensive validation for various European cities, and it was considered functional to produce comparisons with the previously presented outcomes related to observational data.

3.4.2 Methodology

Copernicus Climate Change Service (C3S) provides the UrbClim model outputs of 2 m temperature and the rural-urban mask obtained from Corine Land Cover CLC 2018, over a time period of 10 years (2008-2017) (Hooyberghs et al. [61]). The purpose of this analysis was to complement the results obtained about the UHI-

heatwave interaction, evaluating the data calculated by the model for urban areas in presence and in absence of heatwaves. In particular, 4 cities which revealed statistically significant results and representative of the different Köppen-Geiger climate zones identified in Figure 3.11 were selected, namely Bologna for CFA, Madrid for CSA, Frankfurt for CFB and Stockholm for DFB. For each city the UHI modification was analyzed distinguishing the 10 years climatology of C3S temperature data and the average values during heatwave events retrieved through the methodology described in Section 3.2.5. Specifically, also in this case urban and rural minimum daily temperatures were employed as a reference for nocturnal UHI, and the spatial pattern of the phenomenon was observed. The rural-urban mask of CLC 2018 was used to distinguish urban and rural zones.

3.4.3 Results and Discussion

Figures 3.15 and 3.16 show the 2 m temperature patterns distinguishing the 10-years summer climatology and the heatwave days respectively for Bologna and Madrid, and for Frankfurt and Stockholm. The temperature values were normalized by subtracting the average over the domain area in order to facilitate the comparison among the results of different cities.

Considering the case of Bologna, the distinction between urban and rural temperature was evident. The higher temperature values in areas related to the urban land cover with respect to the surrounding rural ones, according to the C3S rural-urban mask, revealed a notable UHI effect ($\sim 1.5^{\circ}\text{C}$) during summer (Figure 3.15(a)). During heatwaves, the UHI exhibited an exacerbation both in the intensity and in the spatial distribution. Indeed, Figure 3.15(b) shows $\text{UHI} \geq 2^{\circ}\text{C}$ over a wider zone of urban center. Also, the contrast between Southern and Northern rural areas was notable, the former being placed over a mountainous zone and therefore producing a significantly larger temperature difference with respect to the urban center. The outcomes related to Madrid were similar, describing a pronounced UHI phenomenon in summer (Figure 3.15(c)) which underwent an intensification during heatwave days (Figure 3.15(d)). Also in this case the rural region located near the mountainous zone (North) exhibited a more considerable UHI effect. Compared to Bologna, the UHI values for Madrid appeared slightly weaker. Moreover, another difference emerged by considering the classes of CLC 2018: while the *discontinuous urban fabric* was the land cover category which manifested the larger UHI increment in Bologna, the *industrial or commercial units* category was the most affected in Madrid.

The results for Frankfurt (Figure 3.16(a) and (b)) were analogous to the previous ones. However, the enhancement of UHI appeared more homogeneous across the

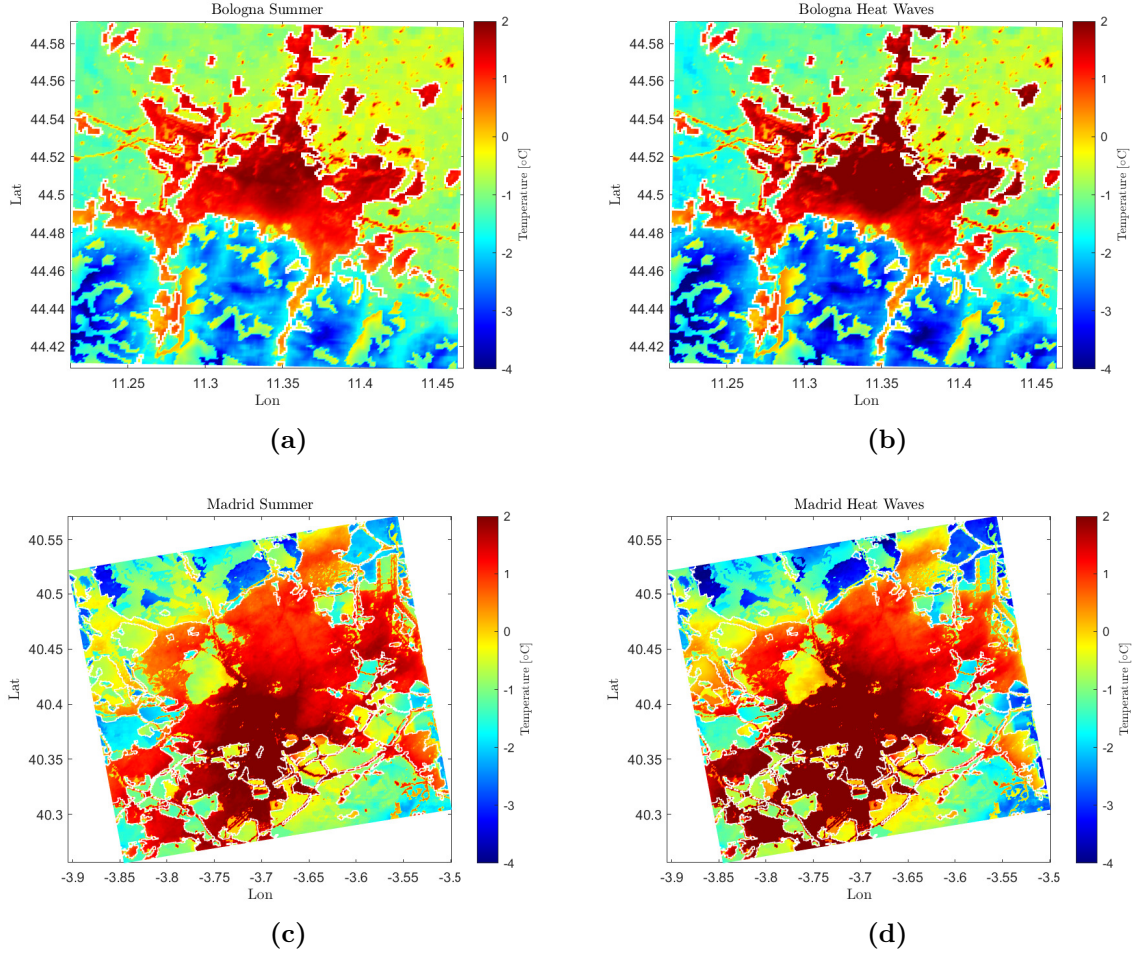


Figure 3.15: Temperature in summer (a), (c) and during heatwave days (b), (d) for Bologna and Madrid. The values are normalized with respect to the average over the domain area.

entire urban region, independent of the CLC classes involved. As for Bologna and Madrid, the temperature differences considerably varied across the regions surrounding the urban center, with substantial modifications depending on the topography. The results regarding Stockholm were moderately different. Indeed, the summer temperature gradient between urban and rural areas (Figure 3.16(c)) was found to be inferior compared to the other examined locations, and also the UHI enhancement during heatwave days (Figure 3.16(d)) was less evident, about $\sim 0.5^{\circ}\text{C}$. A possible explanation of the low UHI intensification could be provided by the peculiar structure of Stockholm, which is surrounded by rivers and waterways whose effect is proven to mitigate the UHI effect (Hatway et al. [89]).

Generally, the results obtained in the study through observational data and showed in Figure 3.7(a) were confirmed. The UHI effect was found to intensify during heatwaves in all the 4 investigated cities, with a $\sim 1^{\circ}\text{C}$ increment with respect

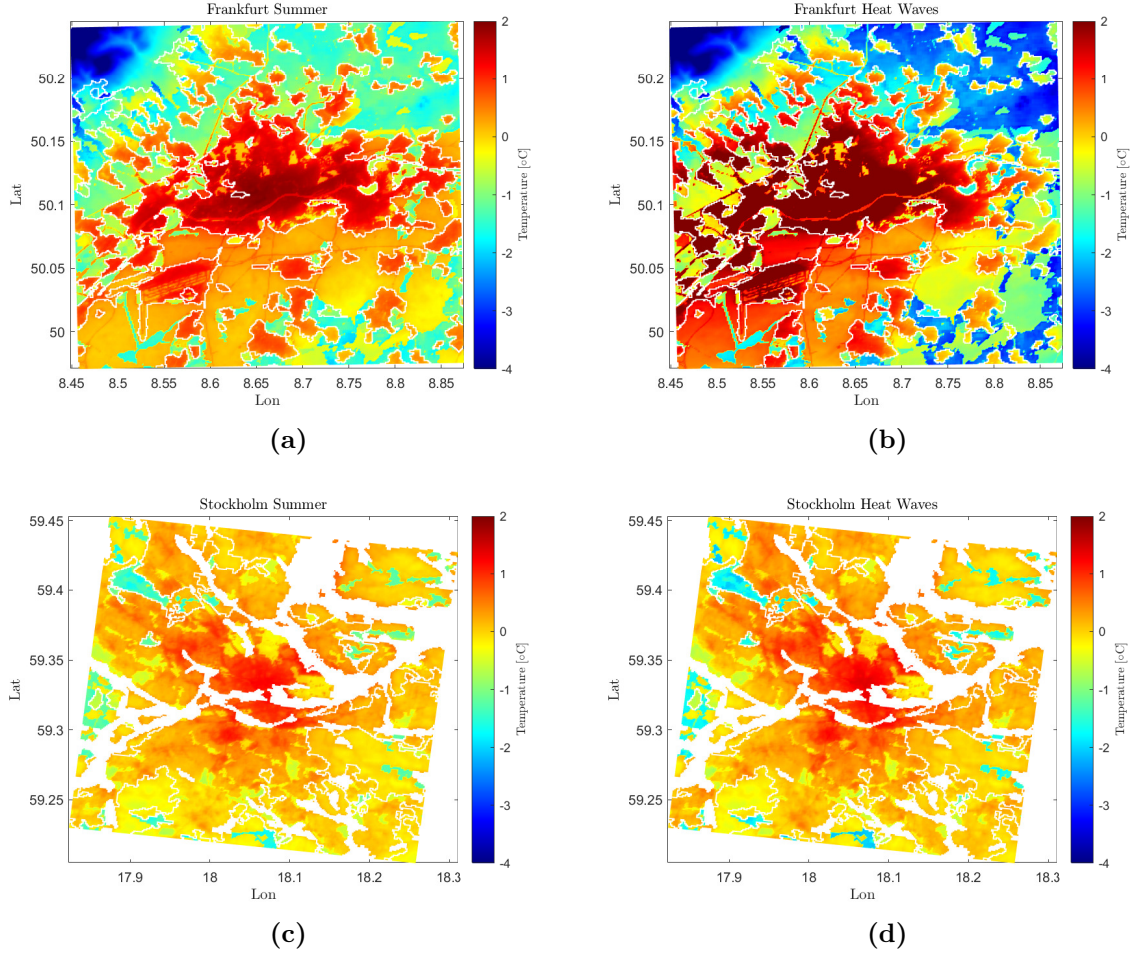


Figure 3.16: Temperature in summer (a), (c) and during heatwave days (b), (d) for Frankfurt and Stockholm. The values are normalized with respect to the average over the domain area.

to the surrounding rural areas. A strong variation of UHI values depending on the rural reference area was noticed, supporting the appropriateness of the adopted criteria for the selection of correct stations in the observational study. No significant differences were retrieved among cities belonging to distinct Köppen-Geiger climate zones. Only Stockholm produced an UHI exacerbation less significant compared to other cities, but the reason was attributed to its peculiar topography, characterized by several water bodies.

3.5 Synthesis of the Main Results

In the first part of the thesis, the relationship between heatwave and urban heat island was investigated. To this end, the daily maximum and minimum temperature records (for diurnal and nocturnal UHI, respectively) measured by meteorological

stations in 37 European cities were examined by distinguishing heatwave days from not-heatwave days during the summers from 2000 to 2019. A methodology that allows to select appropriate urban and rural stations was adopted, considering different characteristics of the station site such as altitude, distance from the city centre and land cover. The UHI magnitude was quantified through the Composite UHI Index (UHII), designed to reduce the role of site-specific variability, while a heatwave was defined as a persistent large-scale temperature anomaly diagnosed in reanalysis data.

For the majority of examined cities the nocturnal UHII featured a positive climatological mean that increased during heatwaves on average by $0.7\text{ }^{\circ}\text{C}$. The analysis of the frequency of days with significantly positive UHII allowed to distinguish between cities where the UHII enhancement was attributed to more days subjected to UHI effect and to more intense UHII values. The analysis of the temporal evolution of UHII during heatwave periods highlighted that the intensification of the UHII was explained by a larger and more persistent increase of urban temperature with respect to rural during a heatwave. The intensification peaks were found at about $1.3\text{ }^{\circ}\text{C}$, three days after the heatwave onset, but notably the increment of urban-rural temperature difference started to strengthen even one week before the heatwave peaks, suggesting that the meteorological conditions of clear-sky and weak winds on the days preceding the heatwave can be also responsible of positive UHI anomalies. The analysis of the relationship between large-scale temperature anomalies and UHII revealed a smooth and continuous relationship between large scale temperatures and UHII, but a large variability. The lack of a threshold behavior in this relationship suggested that large-scale temperature variability can affect UHI at local scale not only during extreme events. A comparison with the outputs provided by the numerical model UrbClim was performed for 4 representative European cities, confirming the evidence of a synergistic interaction between the nighttime UHI and heatwaves independent of the climate zone.

Chapter 4

Concepts of Drought

Drought is acknowledged as a heat-related environmental hazard with catastrophic impacts on several ecosystems. It can take place in all climatic zones and areas around the world, since it deals with the decrease in the amount of collected precipitation during a protracted period, from days to years. Among the other features, the time scale of drought differentiates it with respect to aridity, which is a permanent feature describing only low rainfall areas, and with heatwaves whose duration is usually of the order of a week. The variables involved in the characterization of drought are numerous, ranging from temperature, wind, humidity, and rain distribution, making it a complex phenomenon to analyze (Mishra et al. [90]).

Contrarily to other extreme weather events such as earthquakes or hurricanes, the onset of drought is gradual, and the severity worsens over time. When a drought occurs, it can last for long periods with effects lingering even for decades. The water shortages caused by the lack of precipitation make drought one of the most dangerous weather hazards. Indeed, about 55 million people are globally affected by droughts each year, and these phenomena contribute to further aggravate the issues related to water scarcity, which already impacts 40% of the world's population. Additionally, more than 700 million people are estimated to be at-risk of displacement by 2030 due to drought occurrences (World Health Organisation [91]), and on top of that droughts are projected to be larger in frequency and intensity with every additional increment of global warming (see Figure 4.1).

4.1 Definitions of Drought

The different hydro-meteorological and socioeconomic characterization of various areas across the globe, together with the stochastic nature of water demands, make complicated to provide a unique definition of drought. In addition, depending on

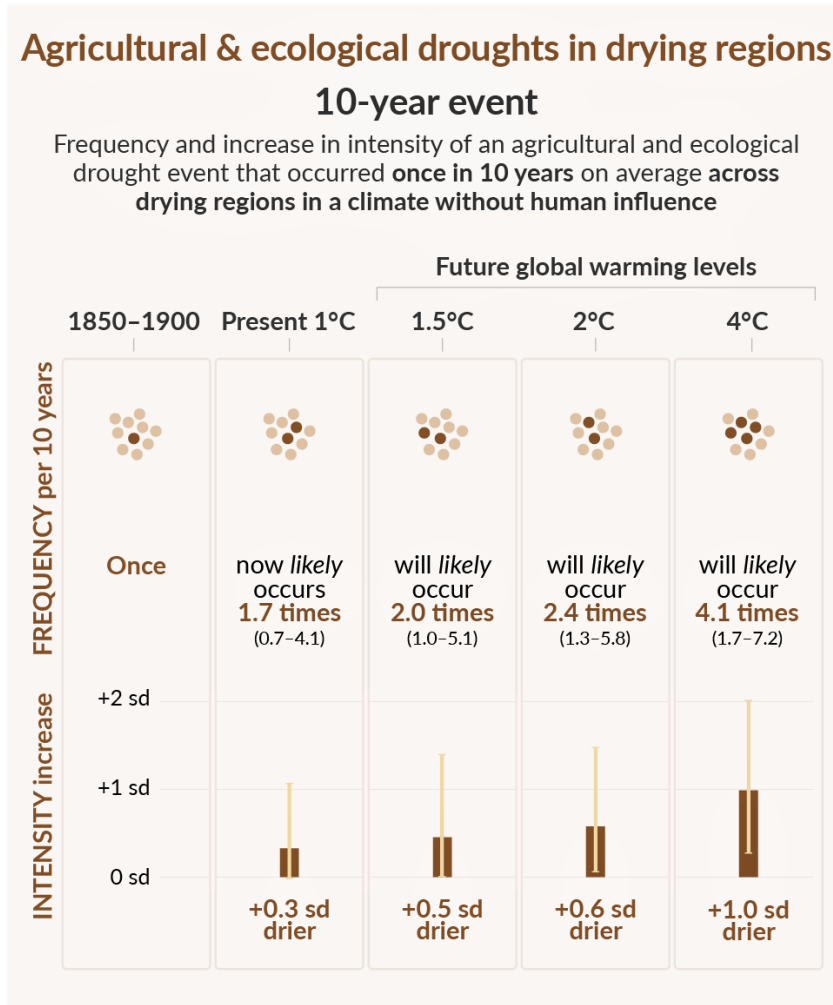


Figure 4.1: Projected changes in agricultural and ecological droughts in drying regions. From Masson-Delmotte et al. [1].

the variable used to describe the phenomenon of interest, drought definitions can change. For example, the World Meteorological Organization [92] defines drought as "a sustained, extended deficiency in precipitation", while the Food and Agriculture Organization of the United Nations [93] designates a drought hazard as "the percentage of years when crops fail from the lack of moisture". It is therefore evident that these two definitions refer to different aspects of the drought event, one related to its generating mechanism and the other concerning its impacts on the soil. In this regard, Wilhite et al. [94] classified the definitions in terms of four attitudes to detect droughts: meteorological, hydrological, agricultural and socioeconomic. The first three approaches treat drought as a physical phenomenon, whereas the last one focuses on the effects of water shortage on the socioeconomic systems. In detail:

- **Meteorological** drought is what usually originates when a precipitation deficit occurs in a certain area. It depends on the level of dryness and the duration

of the dry period with respect to standard climatological conditions. Owing to the variability of atmospheric conditions in different zones, the resulting deficiencies of precipitation are highly dissimilar from area to area, so generally the validity of meteorological drought definitions is limited to a fixed region. For example, some definitions establish drought periods according to the number of days with precipitation inferior to a determined threshold. This kind of methodology can be only applied to regions characterized by a yearly precipitation regime, such as humid mid-latitudes climate, while for areas with seasonal rainfall patterns and protracted periods without rainfall it can be not appropriate. For this reason, other definitions have been developed based on actual precipitation variations with respect to average amounts on monthly, seasonal or even annual time scales;

- **Agricultural** drought refers to agricultural impacts of droughts induced by precipitation shortages, that is to say the effects on evapotranspiration, the soil water deficits, the diminution of groundwater, and so on. In particular, the focus of this definition is mainly about the characteristics of croplands and agricultural terrains, which strongly depend on water supply and on the properties of the soil. A precise definition of agricultural drought should be capable of taking into account the susceptibility to precipitation deficit of crops according to soil moisture, considering also that agricultural droughts are usually out of phase with or delayed with the occurrence of meteorological droughts;
- **Hydrological** drought is connected with the repercussions of prolonged lack of precipitation on surface and subsurface water supply, including streamflow, reservoir and lake levels, and groundwater. Even though all kinds of drought arise from a precipitation deficit, the necessity of this definition comes from the peculiar interest about the role of the hydrologic system. Indeed, as agricultural droughts, even hydrological ones often exhibit a lag with respect to the onset of meteorological droughts because it takes a longer time for precipitation shortage to impact the components of the hydrological process. The significance of this kind of drought is noticeable since it can eventually complicate the management of water usage in hydrologic storage systems dedicated to multiple purposes, such as flood control, irrigation, hydropower, and so on;
- **Socioeconomic** drought definitions derive from the link of the other types of droughts with the supply and demand of some economic assets. Since it is not directly associated to a physical driver, it differs from the aforementioned kind of drought and depends on the temporal and spatial processes of the

economic evolution. To assess the occurrence of socioeconomic drought it is necessary to have a greater demand than the supply for an economic good related to weather-related shortage. Therefore, it is the ratio between demand and supply, and more precisely their relative rate of change, that gives place to this kind of drought. Commonly, the demand for water-related economic goods can increase in line with population growth, and the development or not of socioeconomic drought depends on the correlated improvement of production efficiency, of technology, and overall of the quality of storage surface water.

Nowadays, also a new definition is catching on, namely *ecological drought* (Crausbay et al [95]). Since an episodic deficit in water availability can lead the ecosystems to overcome the thresholds of vulnerability, can impact ecosystem services, and can trigger some feedbacks in natural and human systems, this term has been developed to take into account all these environmental consequences. In particular, ecological droughts consider aspects from various points of view such as losses in plant growth, increases in fires, altered rates of carbon, and water cycle.

4.2 Drought Propagation and Indices

The various drought types appear to be strongly connected with each other, mutually influencing in a direct or indirect manner. Firstly, drought generally originates from precipitation deficits, which define meteorological droughts, and then propagates through the hydrological cycle. Through this process, other factors than the lack of precipitation acquire relevance, such as the high vapor pressure deficit and the enhanced atmospheric evaporative demand. This leads to soil moisture deficits that affect plants and cultivated terrains, generating the agricultural droughts. The diminished soil moisture and evapotranspiration can be then responsible of low runoff and streamflow on the surface or reduced groundwater in the subsurface, producing the hydrological droughts. In turn, the impacts caused by these kind of droughts can deplete the water resources, and ultimately affecting human society when the water supply is insufficient to meet the water demand, resulting in socioeconomic droughts. At the same time, the considerable effect induced by droughts on environmental systems, like forests or aquatic systems, can be accountable of ecological droughts. The entire process regarding the evolution of anomalous hydro-meteorological quantities through the interdependent terrestrial hydrological cycle, outlined in Figure 4.2, has been conceptualized by using the term *drought propagation* (Van Lanen et al. [96]).

A quantitative technique has been adopted for comparing different kinds of drought in various regions across the globe. In particular, the development of *drought indices* has played a fundamental role in the contribution to measure these kinds

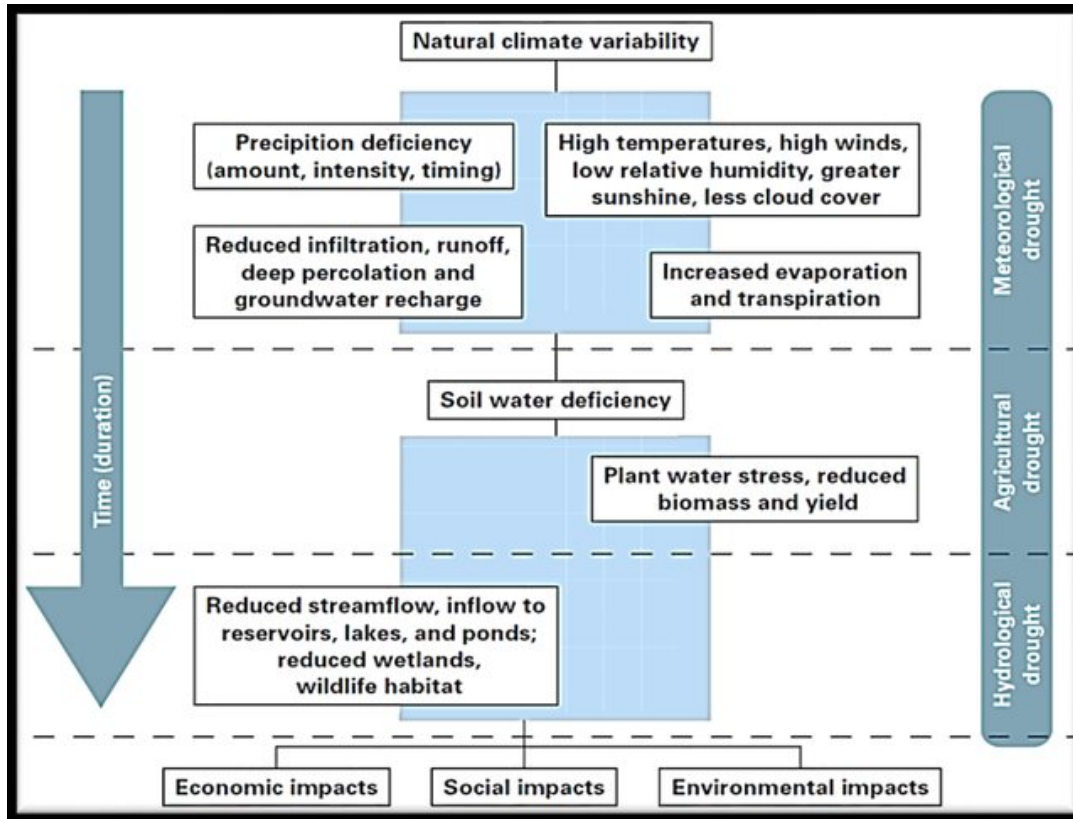


Figure 4.2: Diagram showing the sequence of drought occurrence and impacts of the drought types linked with physical drivers. From Wilhite et al. [97].

of phenomena, and because of their complex mechanisms, several indices have been formulated to appropriately capture drought characteristics. According to Friedman [98], a drought index should be formulated by following these four basic criteria:

- 1) Its time scale, or reference period, should be adequate to the investigated problem;
- 2) It should be a quantitative measure of large-scale, persistent drought conditions;
- 3) It should be applicable to the examined phenomenon;
- 4) A long and precise past record of the index should be available or at least estimable.

Since different systems exhibit distinct response times to the accumulated precipitation deficits, drought impacts have a multi-scalar nature. For this reason, to compare drought conditions across different temporal and spatial scales, standardized drought indices have been developed over the years, with different methodologies and purposes. There is not a specific index universally performing better than

others, so for selecting the most appropriate for the purpose of a study, it is fundamental to take into account various aspects such as the capability to identify the spatio-temporal characteristics of droughts in the region of interest and the primary features of the drought index, as the calculation technique, the input variables, and general advantages and weaknesses. Regarding the detection of meteorological droughts, one of the most employed is the Standardized Precipitation Index SPI (McKee et al. [99]), due to its computational and interpretative simplicity, its robustness, its multi-scalar nature, the possibility of being easily compared across regions subjected to considerably different climates, and especially because it requires only precipitation as input data. By contrast, the Palmer Drought Severity Index PDSI (Palmer [100]), mostly used to monitor long-term droughts, can take into account the potential reduction of moisture due to temperature influences (i.e. the effect of evapotranspiration), so it is opportune in a context of warming environment. However, the main disadvantage is the complexity of its calculation and evaluation, together with its temporally invariant nature. Another index, the Standardized Precipitation and Evapotranspiration Index SPEI proposed by Vicente-Serrano et al. [101], has been recently developed for the study of meteorological droughts, whose formulation follows that of the SPI, but combined with the reference of evapotranspiration, like the PDSI. Therefore, it comprises both the multiple advantages of the SPI and the better accuracy in considering the global warming given by the inclusion of evapotranspiration. Other relevant examples of meteorological drought indices are the Effective Drought Index EDI (Byun et al. [102]), which can identify the onset and end of water deficit periods with high precision since it is based on daily precipitation inputs, and the Drought Reconnaissance Index DRI (Tsakiris et al. [103]), based on the ratio between precipitation and potential evapotranspiration at different time scales and therefore sensitive and suitable in cases of a changing environment, similarly to the SPEI. Regarding agricultural droughts, the Standardized Soil Moisture Index SSI (Hao et al. [104]) is one of the most simple and adopted indicators. It treats the soil moisture analogously to how SPI uses the precipitation, namely considering the accumulation across different time scales with respect to the corresponding climatology. Also the Soil Moisture Deficit Index SMDI, introduced by Narasimhan et al. [105] and based on weekly data of soil water in the root zone (100 cm of depth), has been frequently selected for identifying short-term droughts affecting agriculture. Other more elaborate indices have been lately created to deal with the effects of agricultural droughts. For example, the Multivariate Standardized Drought Index MSDI (Hao et al. [106]) uses as inputs monthly precipitation and soil moisture data, so it is helpful for the identification and monitoring of drought in cases where the lack of rainfall and the subsequent

dehydration of soil are the major contributors. To investigate hydrological drought a widely adopted index is the Standardized Streamflow Index SSFI (Modarres [107]), developed using monthly streamflow values and the standardization method associated to the SPI, and helpful to monitor the hydrological conditions at multiple time scales. Similarly, also the Streamflow Drought Index SDI (Nalbantis et al. [108]) is often employed, exploiting monthly streamflow values and a historical time series for the reference stream gauge to identify hydrological drought events. The analysis of the relationship between distinct types of drought detected through these different kinds of indices furnishes the basis for understanding drought propagation.

Chapter 5

Analysis of Drought Propagation over the Iberian Peninsula

5.1 Purpose

Since the effects of precipitation deficits appear in different systems at distinct time scales, drought is defined as a multi-scalar phenomenon (McKee et al. [109]). Involving mechanisms at multiple scales, the drought signal propagates in the water and energy cycle through a multitude of processes. The first transition generally occurs from the meteorological to the agricultural drought according to the response of soil moisture or crop yield to various meteorological variables, such as precipitation and evapotranspiration. Indeed, the combined effect of water shortage due to a lack of precipitation and the enhanced atmospheric evaporative demand can be responsible of a significant depletion of soil moisture, and therefore lead to agricultural drought events.

Presently, studies on the propagation from meteorological drought to agricultural drought are rare, and more investigations are necessary to deeply understand the propagation characteristics. In a recent review, Zhuang et al. [110] highlighted the most crucial aspects regarding this kind of drought propagation which require further studies. The first one deals with the concurrence of multiple driving factors in drought generation. In particular, since commonly only soil moisture (Xu et al. [111]) or soil water deficit (Zhou et al. [112]) and agricultural reservoir levels (Bae et al. [113]) are taken into account, the conjoint contribute provided by soil moisture, evapotranspiration and precipitation to the development of agricultural droughts is not completely comprehended. Accordingly, as suggested in previous studies, the development and application of new multi-variate indices (Vicente-Serrano et al. [101]) could be helpful in shedding light on the complex relationships between

meteorological and agricultural drought. Also, for the analysis of propagation from meteorological to agricultural drought it is appropriate to employ high resolution and long-term data, as highlighted by Li et al. [114], in particular as concerns soil moisture which can be obtained through three major sources: *in-situ* observations, remote sensing, and hydrological models. The majority of studies based on *in-situ* observations involve measuring soil moisture levels at different depths across the globe using various soil moisture networks, but this approach has limitations as the observations are relatively short (Quiring et al. [115]) and unevenly distributed (Zhu et al. [116]), or may be unavailable in some isolated areas. Remote sensing products have been preferred in some studies (Tian et al. [117]) since they provide better spatial coverage, but they appeared insufficient because they only cover a few centimeters of soil, while soil moisture from hydrological simulations has been found to be possibly affected by discrepancies compared to *in-situ* data (Xia et al. [118]). Therefore, more studies combining and evaluating different datasets are needed. Note that variations in vegetation health and/or cover may be due not only to rainfall or soil moisture deficits, but also to other stress factors, such as plant diseases. In this sense, indicators of vegetation stress and information on the deficit of precipitation and soil moisture must be considered together.

Bearing in mind these considerations, the present study attempted to fill the evidenced research gaps related to the study of agricultural droughts and particularly to the propagation from meteorological droughts. The purpose was to analyze an adequately selected multi-annual dataset containing multiple drought events in order to characterize the meteorological and agricultural drought with a sufficiently wide spectrum of information. The study involved diverse kinds of standardized drought indices, ranging from uni-variate to multi-variate indices considering various physical quantities, together with a suggestion for a new combined index, in order to consider the contribution provided by different factors to the phenomenon of drought propagation. The entire analysis was carried out over the well recognized drought hot spot of Iberian Peninsula (IP) (Figure 5.1), a Mediterranean region with a highly variable rainfall regime, that has presented recurrent droughts and a significant tendency towards more arid conditions in the last decades (Pàscoa et al. [119]).

5.1.1 The Iberian Peninsula Hot Spot

The spatial patterns of droughts are complex, because the variability of conditions between adjacent locations can be high. Indeed, it is easy to find an area subject to drought while neighbouring regions feature a normal or even wet environment. Different spatial characteristics of droughts are mainly detectable in climatic tran-

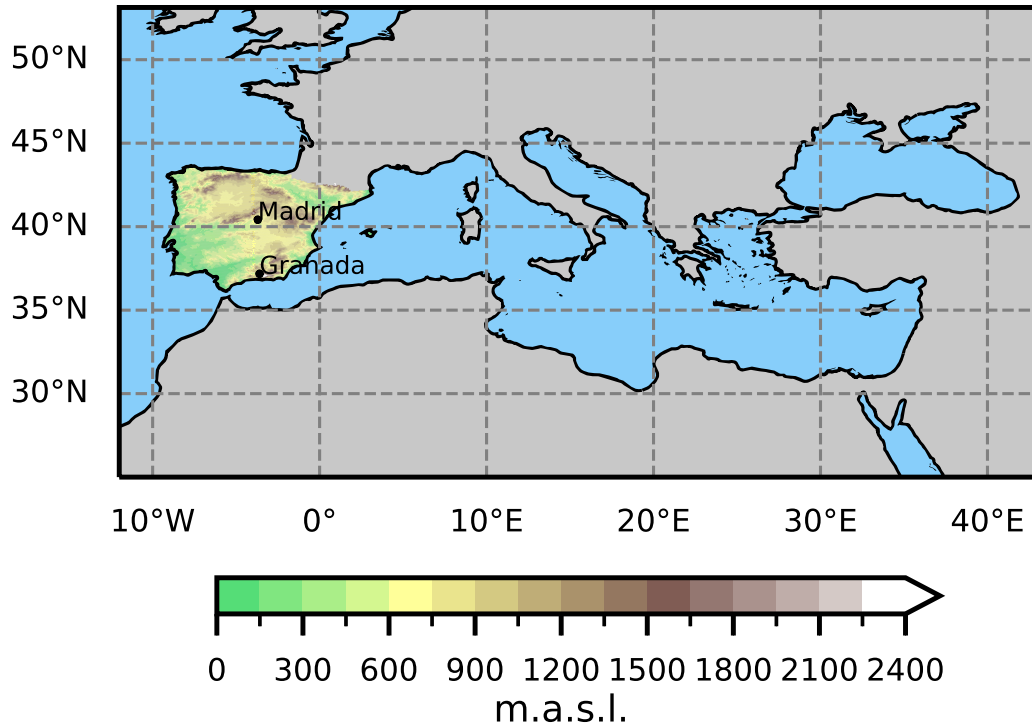


Figure 5.1: Location of the Iberian Peninsula within the Mediterranean sector. It includes the continental areas of Spain, Portugal and Andorra.

sition areas, where atmospheric influences are heterogeneous. A notable example of this kind of zones is the Iberian Peninsula (IP), which is located between temperate and subtropical climates and it is subjected to a large variability of precipitation caused by diversified atmospheric patterns. Studies demonstrated that droughts have been severe and long in the IP during the years (Martín-Vide et al. [120]), and that this phenomenon has produced strong effects in ecosystems with related social and economic impacts. In the IP, agricultural droughts have produced substantial losses in cultivated terrain, and crop yields have been seriously reduced during dry years (Austin et al. [121]). Moreover, the frequency of droughts affecting the semi-arid areas of the IP hindered the development of vegetation cover and made the soil inclined to erosion. Additionally, the socioeconomic vulnerability to drought exacerbated due to the growth in water demands concurrent with the population increase. In the last decades, the severity of droughts in the IP has intensified, with a reduction of vegetation land cover owing to an enhanced atmospheric evaporative demand (Vicente-Serrano et al. [122]). Moreover, Greve et al. [123] assessed that the South-West of the IP is one hot spot of the pattern *dry gets drier*, and that the projected increase of drought frequency in this region during the 21st century is estimated to further worsen this problem.

5.2 Methodology

5.2.1 Drought Indices

For the identification of meteorological droughts, the Standardized Precipitation and Evapotranspiration Index SPEI based on precipitation minus evapotranspiration (water balance) was selected, due to its demonstrated suitability for drought detection in Spain (Vicente-Serrano et al. [101]). To capture agricultural droughts, several standardized indices were adopted, with the purpose to analyze the different outcomes generated depending on their distinct formulations. The first agricultural drought index was the Standardized Soil Moisture Index SSI, which was chosen for its simplicity and well documented capability to detect agricultural drought events [124], besides its reliability at a global scale for studying the propagation from meteorological drought detected by SPEI (Zhu et al. [116]). Then, to evaluate the composite effect of different variables in the characterization of agricultural droughts, an additional multi-variate index was computed, namely the Multivariate Standardized Drought Index MSDI based on precipitation and soil moisture. Moreover, a currently developed index was included in the analysis, due to its capacity to entirely account for the different variables involved in agricultural drought generation. It is named the Standard Precipitation, Evapotranspiration and Soil Moisture Index SPESMI, introduced by Xu et al. [125] and formulated depending on both precipitation minus evapotranspiration balance and soil moisture. All the indices employed in this study were calculated following the non-parametric procedure indicated by Hao et al. [104], which provided an alternative to the commonly employed technique proposed in Hao et al. [106] based on multivariate parametric copulas (Nelsen et al. [126]). Specifically, considering the formulation of MSDI as a representative example, precipitation and soil moisture at a selected time scale (e.g. 3 months) were defined as random variables X and Y , respectively, and their joint distribution was indicated as

$$P(X \leq x, Y \leq y) = p. \quad (5.1)$$

In contrast with the parametric method, which computes the cumulative joint probability p through the copula $C[F(X), G(Y)]$ where $F(X)$ and $G(Y)$ are the marginal cumulative distribution functions of X and Y , in this case the empirical joint probability p was estimated with the Gringorten plotting position formula (Gringorten

[127]) as in Hao et al. [104]

$$P(x_k, y_k) = \frac{m_k - 0.44}{n + 0.12}, \quad (5.2)$$

where n was the number of the total input data and m_k was the number of occurrences of the pair (x_i, y_i) with $x_i \leq x_k$ and $y_i \leq y_k$ for $i = 1, 2, \dots, n$. Removing the adoption of a copula family, which is typically chosen making assumptions regarding the probability distributions of the involved variables (Salvadori et al. [128]), allowed to avoid the computational burden due to the necessary goodness-of-fit tests. Similarly, for univariate indices such as SSI, the empirical marginal probability was calculated by using the univariate form of the Gringorten plotting position formula

$$P(x_i) = \frac{i - 0.44}{n + 0.12}, \quad (5.3)$$

where n was again the number of total input data and i was the rank of the observed values from the smallest. After obtaining the joint or marginal probability P , to compute the drought index it was only needed to retrieve the inverse of the standard normal distribution function ϕ , namely

$$MSDI = \phi^{-1}(P). \quad (5.4)$$

Following this procedure it was possible to accomplish all the aforementioned drought indices simply modifying the considered variables. For example, in SPESMI the joint probability p of precipitation minus evapotranspiration and soil moisture was calculated (see Table 5.1 for all the details).

Drought Index	Structure	Variables	Type of Drought
SPEI	Multivariate	P-E	Meteorological
SSI	Univariate	SM	Agricultural
MSDI	Multivariate	P, SM	Agro-Meteorological
SPESMI	Multivariate	P-E, SM	Agro-Meteorological

Table 5.1: Characteristics of the standardized drought indices constructed with the non-parametric technique. P stands for Precipitation, SM for Soil Moisture and E for Evapotranspiration.

The advantage of this method was evident, not only related to the simplicity but also to the uniformity of the required calculations. Thanks to this homogeneous methodology, the entire analysis was unaffected by the different nature of the drought indices and it was possible to assess their distinct features exclusively depending on the physical quantities concerned. The selected time scales for

drought indices were 1-, 3- and 6-month since the focus was from the immediate to seasonal/semi-annual influence of precipitation, evapotranspiration and soil moisture on drought characterization. The drought categories were defined according to the study of Ojeda et al. [129] regarding the IP, in order to classify the values of the drought indices. Therefore, all indices with values below -2 were considered to be *extreme*, namely drought category -2; the *severe* drought category (-1.5) was assigned to index values between -2 and -1.5; *moderate drought* category (-1) was assigned to values below -1 but above -1.5; *normal/wet* conditions (1) were associated to values above 0; and finally -0.5 was set for all other cases, identifying *dry* conditions (see Table 5.2).

Drought Index	Drought Category	Conditions
$\text{Index} \leq -2$	-2	Extreme Drought
$-2 < \text{Index} \leq -1.5$	-1.5	Severe Drought
$-1.5 < \text{Index} \leq -1$	-1	(Moderate) Drought
$-1 < \text{Index} \leq 0$	-0.5	Dry
$\text{Index} > 0$	1	Normal/wet

Table 5.2: Drought categories for the uni-variate and the multi-variate standardized drought indices.

Besides the described uni-variate and multi-variate indices, owing to the complex nature of drought events, another new index was proposed. In order to avoid relying on the information provided by a single index only, which might omit important characteristics of drought phenomena, a Combined Agricultural Drought Index (COMB) was developed adapting the Combined Drought Indicator described by Spinoni et al. [130]. In detail, COMB was based on the composition of the three agricultural drought indices SSI, MSDI and SPESMI, and it was structured to favour the predominance of drought conditions over the other possible classes, namely when more than one indicator showed values below -1. Following the indications proposed by Spinoni et al. [131], COMB was not built as a simple average, but in agreement with the drought categories reported for individual drought indices. Therefore, it was assigned a value corresponding to extreme drought conditions (-2) when at least two single indices revealed values below -2, to severe drought conditions (-1.5) if at least two indices showed values between -2 and -1.5, to moderate drought conditions (-1) if at least two indices reported values below -1 and above -1.5, to dry conditions (-0.5) when two or more indices had values between -1 and 0, and normal/wet conditions (1) if at least two single indicators showed positive values (see Table 5.3).

The severe drought condition (-1.5) was a refinement with respect to Spinoni et

Drought Indices (SSI, MSDI, SPESMI)	COMB	Conditions
2+ indices $\in (-\infty, -2]$	-2	Extreme Drought
2+ indices $\in (-2, -1.5]$	-1.5	Severe Drought
2+ indices $\in (-1.5, -1]$	-1	(Moderate) Drought
2+ indices $\in (-1, 0]$	-0.5	Dry
2+ indices $\in (0, +\infty)$	1	Normal/wet

Table 5.3: Methodology for the calculation of Combined Agricultural Drought Index COMB. Adapted from Spinoni et al. [131], with a refined classification.

al., useful to provide information with higher detail and consistent with the study of Ojeda et al. In the event that the three indices belonged to three different classes, the arithmetic average was calculated and COMB was defined depending on the category of the resulting value. It is evident that, through this procedure, the main focus of the combined index is on identifying drought conditions, while normal and wet conditions are important only to detect the end of the drought events.

5.2.2 Dataset

With the development of data assimilation technology, reanalysis data has become more representative of observed conditions and less limited than *in-situ* and remote sensing data. Reanalysis data offers global coverage, long time series, no gaps in space and time, and contains subsurface data, making it ideal for assessing agricultural drought. Several reanalysis datasets have been developed, and this study was conducted by employing the state-of-the-art reanalysis dataset for land applications ERA5-Land (Muñoz et al. [132]), provided by the European Centre for Medium-Range Weather Forecasts (ECMWF) and included in the Copernicus Climate Change Service (C3S) of the European Commission. The ERA5-Land dataset was chosen as recommended in Zhang et al. [133] due to its demonstrated relatively high accuracy compared to other remote sensing and reanalysis datasets (Beck et al. [134]). It furnishes a detailed record of land surface evolution from several decades ago to the present with a large amount of key variables representing the water and energy cycles. ERA5-Land contains data at a monthly temporal resolution, which were accumulated for the computation of the drought indices according to the different time scales employed. ERA5-Land was produced by replaying the land component of the ERA5 climate reanalysis, and it was chosen due to its improvement in characterizing the water cycle compared to ERA5 (Muñoz et al. [135])). The original spatial resolution of the ERA5-Land reanalysis dataset is 9 km on a reduced Gaussian grid, but C3S provides data re-gridded to a regular latitude-longitude grid of $0.1^\circ \times 0.1^\circ$, which corresponds to ~ 11 km at mid-latitudes. As aforementioned, the

selected area was the Iberian Peninsula for a 72 years period ranging from 1950 to 2021, using monthly-mean averages pre-calculated by C3S since sub-monthly fields were not required. The variables used for this study, which were necessary for the computation of drought indices, were essentially three:

- **Total Precipitation** [m] - The accumulated liquid and frozen water (rain and snow), that fell to the Earth's surface from the beginning of the simulation time to the end of the model step. It includes large-scale precipitation and convective precipitation, but it does not consider fog, dew or precipitation evaporating in the atmosphere before reaching the surface of the Earth. The units of precipitation are depth in metres, which correspond to the extent that water would have if it were spread uniformly over the grid box;
- **Soil Moisture** [m^3m^{-3}] - The volume of water in different soil layers defined by the ECMWF Integrated Forecasting System. In particular, considering the surface at 0 cm of depth, layer 1 goes from 0 - 7 cm, layer 2 from 7-28 cm, layer 3 from 28-100 cm and layer 4 from 100-289 cm. Although the depth required for the most adequate representation of soil moisture content for agricultural droughts is still under exploration (Arora et al. [136], Qiu et al. [137]), it is common to consider the first 100 cm of depth, namely the Root Zone Soil Moisture. However, for this study the indication of Bageshree et al. [138] was taken into account, which suggested to remove the lower layers to better represent the soil moisture conditions due to ancillary sources such as local rainfall or irrigation, and only the first two ERA5-Land layers were used (0-28 cm);
- **Potential Evapotranspiration** [m] - Usually considered to be the amount of evaporation, under existing atmospheric conditions, from a surface of water having the temperature of the lowest layer of the atmosphere. The ECMWF Integrated Forecasting System computes it for an agricultural surface as if it is well irrigated, but assuming that the atmosphere is not affected by this artificial surface condition. For completeness, the values of potential evapotranspiration provided by ERA5-Land were compared to those obtained with an analytical calculation by using the Penman-Monteith equation (Monteith [139]), and negligible variations were retrieved.

5.2.3 Methods of Analysis

In the present study several aspects of drought phenomenon were investigated. In particular, the main focus was the propagation from meteorological to agricultural

drought, and this process was addressed through different approaches always in a perspective of retrieving the distinct behaviors of the employed drought indices. The first part of the analysis was dedicated to separately characterize the two types of droughts selected, with a more in-depth attention to agricultural drought events. Considering the entire time window of the utilized dataset (1950-2021), the initial step was a qualitative examination of the temporal evolution of the diverse drought indices at the three time scales, observing the trend over the years and trying to identify possible similarities or differences between SPEI and agricultural indices, and among the agricultural indices themselves.

Then, a comparison with observations was conducted for agricultural drought indices. In detail, the Fraction of Absorbed Photosynthetically Active Radiation (FAPAR) Anomaly was chosen, which provides an estimation of the health conditions of vegetation (Myneni et al. [140]), due to its demonstrated capability of monitoring and assessing agricultural drought impacts (Gobron et al. [141]). The FAPAR Anomaly indicator that is implemented in the Copernicus European Drought Observatory EDO (Spinoni et al. [142]) was employed, whose values are computed as deviations from the long-term mean of the biophysical FAPAR derived from surface reflectances measured by the MODIS-Terra satellite over a time window of 21 years (2001-2021). The FAPAR anomalies furnished by EDO are available with a 1 km spatial resolution and are calculated for every 10-day interval, so it was necessary to integrate them on a 11 km grid and to compute the mean for every 3 values (30 days) in order to appropriately compare these products with the monthly drought indices obtained from the ERA5-Land dataset. In addition, as recommended by Peng et al. [143], a re-standardization F_s of the obtained monthly averaged FAPAR anomalies was computed, described by

$$F_s = \frac{F_i - \bar{F}}{\sigma}, \quad (5.5)$$

where F_i is the monthly averaged FAPAR anomaly for month i during a specific year, while \bar{F} and σ are the mean and the standard deviation of monthly averaged FAPAR anomaly considering all months i over the whole time period from 2001 to 2021. The analysis through FAPAR anomalies was aimed at evaluating the efficiency of agricultural indices to detect vegetation stress in areas affected by severe droughts, and it was based on the verification metrics adapted from Zhang et al. [144]. In particular, to compare the results of the drought indices SSI, MSDI, SPESMI and COMB with FAPAR anomalies, the following verification metrics were used: Probability Of Detection (POD), False Alarm Ratio (FAR), Critical Success Index (CSI) and Effect Of Drought (EOD). Keeping in mind the drought categories reported in Tables 5.2 and 5.3, the metrics were formulated as:

$$POD = H/(H + M)$$

$$FAR = F/(H + F)$$

$$CSI = H/(H + M + F)$$

$$EOD = (H + H_N)/(M + F + H + H_N)$$

where H (Hit) denoted the number of gridpoints where the agricultural drought index evidenced drought categories -1,-1.5 or -2 and FAPAR anomaly showed values belonging to the same range of categories; M (Miss) designated the number of grids where FAPAR anomaly was subjected to drought categories -1,-1.5 or -2 and the agricultural drought index was subjected to categories higher than -1; F (False Alarm) stood for the number of grids where the FAPAR anomaly belonged to categories higher than -1 but agricultural drought index indicated drought categories -1, -1.5 or -2; H_N (Hit Null) expressed the amount of grids where drought indices and FAPAR anomaly revealed categories 0.5 or 1; and $(M + F + H + H_N)$ denoted the total quantity of grids considered. Therefore, the values of all the four verification metrics range between 0 and 1, and a perfect fit is characterized by $POD = 1$, $FAR = 0$, $CSI = 1$ and $EOD = 1$.

The successive step consisted in studying the relationship between the properties of droughts detected with different types of indices. To identify the drought events, from which to extract the drought characteristics, the widely applied *run theory* (Yevjevich [145]) was chosen. According to this method, a drought event starts when a drought index falls below a fixed threshold, then persists until the index values are continuously below that threshold (negative run), and finishes when the index exceeds the threshold level (positive run). For this study, the threshold value for drought indices was established at -1 as usual, but a specific attention was dedicated to severe and extreme drought events, which are generally the most relevant in terms of impacts and consequences. Referring to the recognized drought events, average quantities over the whole time period were calculated for all agricultural drought indices on each gridpoint. Specifically,

- **Percentage:** spatial fraction of IP affected by severe/extreme droughts;
- **Duration:** number of months with drought index values below the severe drought (-1.5) threshold;
- **Frequency:** number of drought events per year;
- **Severity:** lowest value of the drought index during the drought periods;
- **Intensity:** ratio of drought severity to the drought duration;

- **Magnitude:** sum of absolute values of the drought index during the drought period.

After describing the average behavior and features of the agricultural drought events through different indices, the second part of the study dealt with the proper analysis of propagation from meteorological to agricultural droughts. Taking into account the entire time period of ERA5-Land dataset, in the first place the response time scale RT as in Huang et al. [146] was computed. The response time scale, also known as drought propagation time, refers to the duration required for the cumulative shortage of precipitation during a meteorological drought to translate into an agricultural drought, and it is based on a correlation analysis between the agricultural drought index at a monthly time scale and the meteorological drought indices at different time scales. Essentially, for each location the Pearson correlation coefficient between the time series of SSI/MSDI/SPEI/COMB at 1-month time scale and SPEI at time scales 1-, 2-, 3-, ..., 48-month was calculated. Then, the response time scale for a certain agricultural drought index corresponded to the time scale of SPEI showing the highest Pearson correlation coefficient with the values of that index.

Due to the characteristics of soil and other factors, not all meteorological droughts generate agricultural droughts, and vice versa not all agricultural droughts derive from meteorological droughts. For this reason, it was interesting to evaluate the drought propagation rate PR (Sattar et al. [147]), defined as the ratio between the occurrences of the two different drought types

$$PR = \frac{m}{n}, \quad (5.6)$$

where m is the number of agricultural drought events and n is the total amount of meteorological drought events occurred in the whole dataset period and area. Also in this case PR was calculated for all the agricultural drought indices, considering different time scales.

To analyze other specific parameters of drought propagation, it was helpful to restrict the investigation to a significant case study. In this respect, the most impactful drought event in the IP during the 72 years record of ERA5-Land occurred in 2005, which generated severe effects on the entire European continent reducing by a 10% the cereal yields (Ivanova [148]). This episode is well documented by Spinoni et al. [131], and it is reported in the European Drought Observatory database and in the Emergency Events Database EM-DAT (Sapir et al. [149]), which provided a good reference and allowed to select this event for the analysis. The period including the 2005 drought was investigated by empirically examining the sequential

spatial extent of drought coverage according to different drought indices at various time scales (Tijdeman et al. [150]). Through this procedure, the spatial drought propagation across different systems was observed over the IP and some locations were identified for a further analysis involving the lag time LT between the onset of meteorological and agricultural droughts. According to Sattar et al. [147], the lag time LT for two different types of drought event was expressed as

$$LT = T_M - T_A, \quad (5.7)$$

where T_M and T_A represented the initial time (in months) of meteorological and agricultural drought, respectively. Therefore, LT was useful to characterize the drought propagation through the difference of the onset timing of the two drought episodes.

5.3 Results and Discussion

5.3.1 Characterization of Drought Phenomena over IP

Temporal Evolution of Drought Indices

The introductory phase of the analyses concerned the qualitative inspection of the behavior of the computed indices during the whole time period considered. Figure 5.2 shows the temporal evolution of the IP averaged meteorological index (SPEI) and agricultural drought indices (MSDI, SPESMI, and SSI; AD indices hereafter) from 1950 to 2021. In particular, the spatially averaged SPEI and the four AD indices computed at 1-, 3- and 6-month time scales are represented separately, allowing to distinguish the main features of meteorological and agricultural events.

Due to the nature of the indices, clearly the evolution appeared smoother for the largest time scales with respect to the 1-month scale, but a common feature was evident. Indeed, both for SPEI and AD indices a slight trend towards an enhanced dryness was noticeable during the last two decades, confirming the results for meteorological droughts obtained by Coll et al. [151] with parametric indices, and extending the assessment also to agricultural droughts. Figure 5.2 revealed that the frequency and the severity of meteorological drought episodes have increased since 1990's, and especially for the last 10 years the recurrence of severe droughts has experienced a notable development. Despite it was difficult to retrieve detailed information to characterize drought phenomena from Figure 5.2, the similarities of the indices suggested a good correlation between the contributions of precipitation deficit, water balance and soil moisture. Moreover, regarding AD indices some

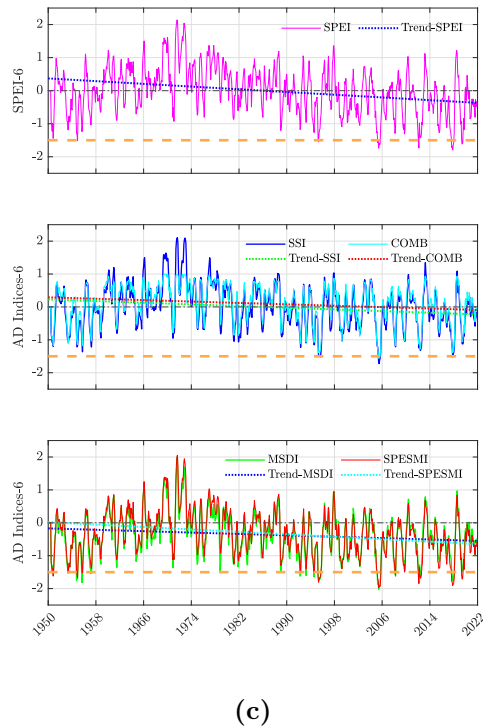
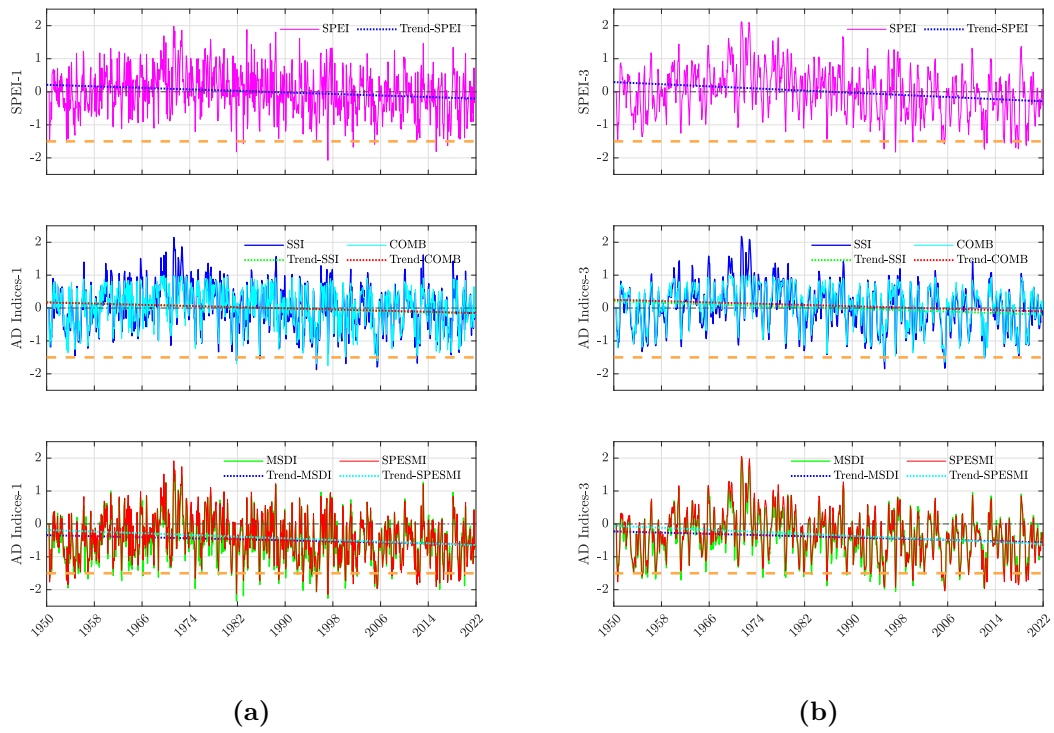


Figure 5.2: Temporal evolution of Iberian Peninsula averaged SPEI and agricultural drought (AD) indices (SSI, COMB, MSDI and SPESMI) at 1-month (*a*), 3-month (*b*) and 6-month (*c*) time scales for the entire period considered. The linear trend is also represented for each index. The orange dashed line indicates the -1.5 threshold for severe drought events.

differences emerged. In fact, the highest values among the AD indices were reached by SSI, while the two multi-variated indices reported the lowest values. COMB index revealed its intrinsic characteristic of being a compromise between these two types of indices. Also, the two multi-variate indices, which include the effect of precipitation, seemed to better reproduce the variations of SPEI, suggesting only a limited impact of soil moisture in their computation.

Comparison with FAPAR Anomaly

Figure 5.3 presents the skill score metric indices for the four AD indices at different time scales (1-, 3-, and 6-month) in comparison to FAPAR anomalies. As defined in section 5.2.3, H (Hit) means that the considered AD index could successfully identify the drought-affected areas in regions where there were also conditions of dry vegetation identified by FAPAR anomalies, while M (Miss) stands for the gridpoints where the AD index failed to detect drought in the zones with high vegetation stress monitored by FAPAR anomalies. Therefore, the large values of $POD = (H + M)/M > 0.8$ meant that M was near zero, implying that gridpoints dominated by agricultural droughts were definitely those characterized by a stressed land vegetation, especially concerning semi-annual droughts (6-month time scale) detected through MSDI and SPESMI. On the other hand, F (False Alarm) denotes the number of grids when SSI, MSDI, SPESMI or COMB detected drought conditions but with disagreement compared to the FAPAR anomalies. The non-zero results for $FAR = F/(H + F)$ indicated that there were some areas with dehydrated plants that could not be accurately monitored by AD indices, with almost negligible variations among the time scales and indices. This was also confirmed by the values of $CSI = H/(H + M + F)$, suggesting that the regions classified with a desiccated flora by FAPAR anomalies were not only those where the AD indices identified drought conditions, while the opposite was almost everywhere true. The ratio of drought-affected areas detected by AD indices corresponding to high vegetation stress with respect to the total zones of high vegetation stress recognized by FAPAR anomalies was approximately 0.5, with slightly increasing CSI for semi-annual droughts. This suggests that FAPAR could monitor arid areas which could not be successfully captured by SSI, MSDI, SPESMI, or COMB, maybe due to the fact that FAPAR anomalies reveal variations in the vegetation health which can derive not only from rainfall or soil moisture deficits, but also from other stress factors such as plant diseases. In parallel, considering H_N (Hit Null) the amount of gridpoints that were free of droughts and with healthy foliage, the values of $EOD = (H + H_N)/(M + F + H + H_N)$ lower than 1 implied some areas in mixed conditions, namely affected by drought which had no relevant impacts on vegetation

or unhealthy vegetated regions caused by other factors than droughts. In conclusion, SSI, MSDI, SPESMI, and COMB were efficient in assessing the vegetation stress of IP during drought events, but they were not sufficient to distinguish all the areas identified by FAPAR anomalies, whose stress could be due to different factors than drought occurrence.

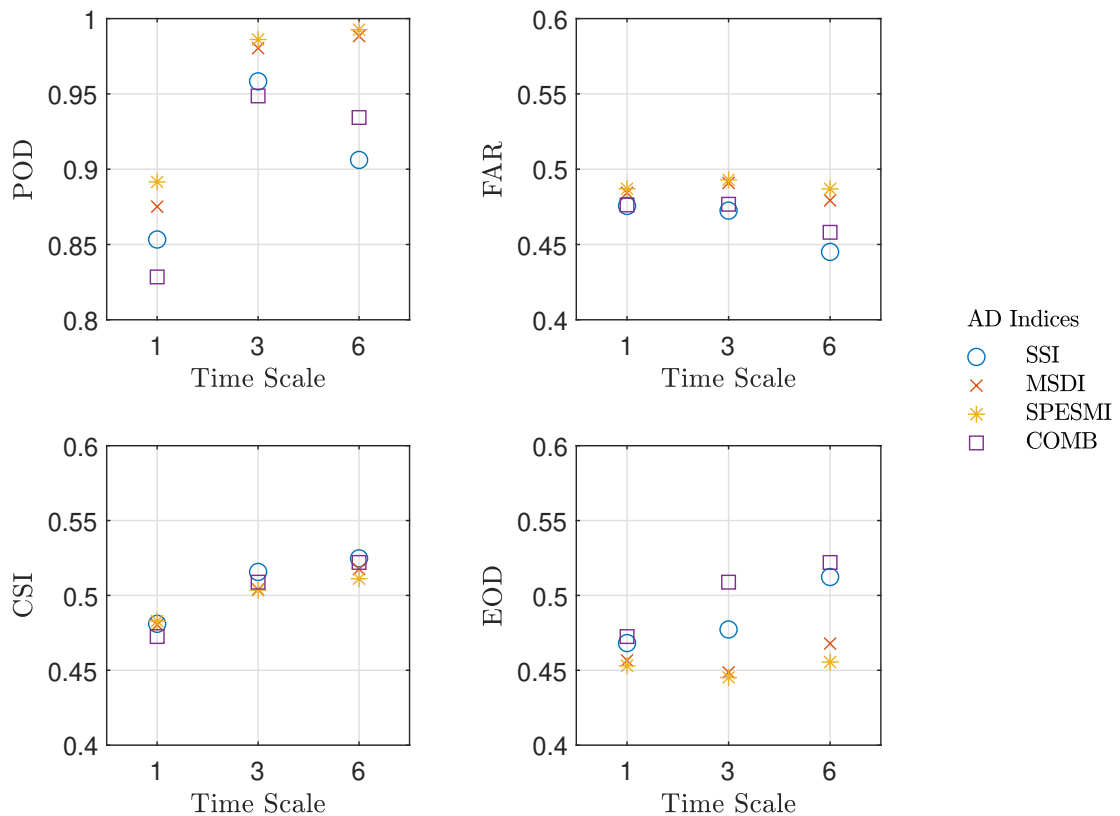


Figure 5.3: Skill score metrics regarding FAPAR anomalies for AD indices at the 1-, 3-, 6 month time scales.

Characteristics of Agricultural Droughts

To examine the different behaviors of the AD indices over the IP during the selected period, several drought characteristics were analyzed. In the first place, the percentage of the IP averagely affected by severe drought events was calculated by evaluating the spatial fraction of areas that showed an average severity value of -1.5 or lower. A relevant outcome is represented in Figure 5.4, which shows the percentage of IP averagely subjected to severe/extreme droughts (i.e. AD indices ≤ -1.5) at 1-, 3- and 6-month time scales. The most visible outcome was the considerably reduced drought affected area retrieved by SSI with respect to other indices, especially the two multi-variate. Indeed, while MSDI and SPESMI revealed a percentage superior

to 75% of IP, SSI did not reach the 40%. The joint effect of precipitation (or water balance) and soil moisture deficits produced drought events in a wider fraction of IP compared to the soil moisture deficiency alone, approximately with a 40% difference for each time scale, a logical consequence of the MSDI capability MSDI to detect both meteorological and agricultural events. COMB exhibited percentage values around 60%, a compromise between the uni-variate and the multi-variate indices. The variations of the values for the same AD index depending on the time scale were small, and generally the highest percentage were reached for 1-month droughts.

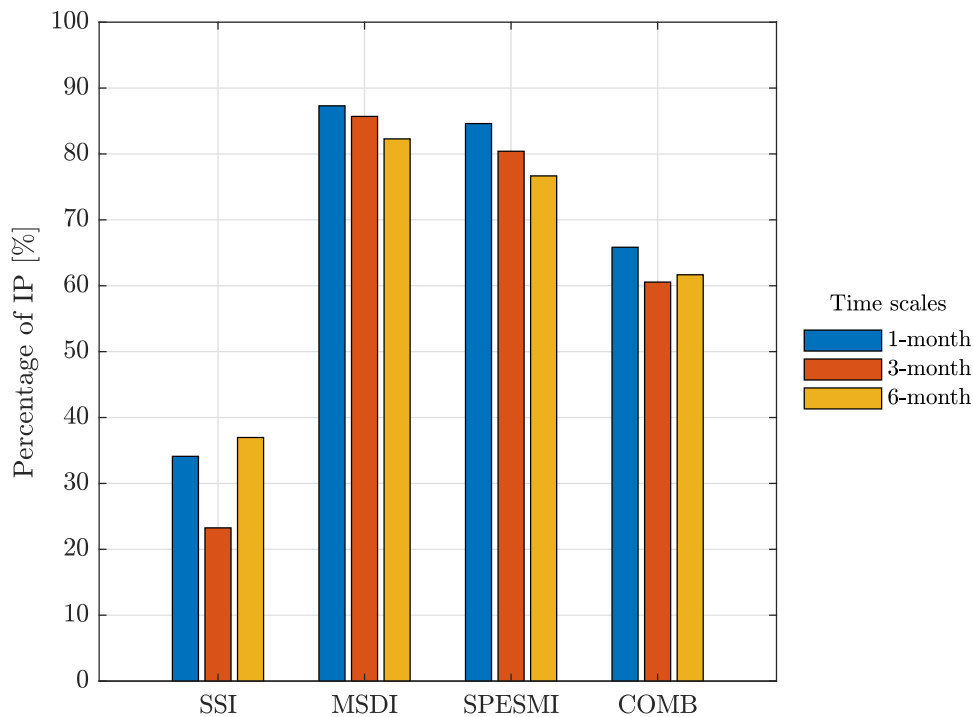


Figure 5.4: Percentage of the IP affected on average by severe/extreme droughts according to agricultural indices at the 1-, 3-, 6-month time scales.

Other interesting characteristics were investigated for agricultural droughts detected by AD indices at 1-, 3- and 6-month time scales. Figure 5.5 represents the frequency of severe/extreme droughts per year, which is strictly correlated with duration, and the drought severity, which is generally accounted as the most adequate characteristic to furnish information about the significance of drought events.

The frequency of severe/extreme drought events per year (Figure 5.5(a), 5.5(c), and 5.5(e) for 1-, 3- and 6-month time scales, respectively) confirmed that multi-variate indices were more sensitive than uni-variate ones in detecting drought events in a larger area. Specifically, SSI identified less than 1 severe/extreme drought event per year, on average, across all the IP at the 1-month time scale, while SPESMI

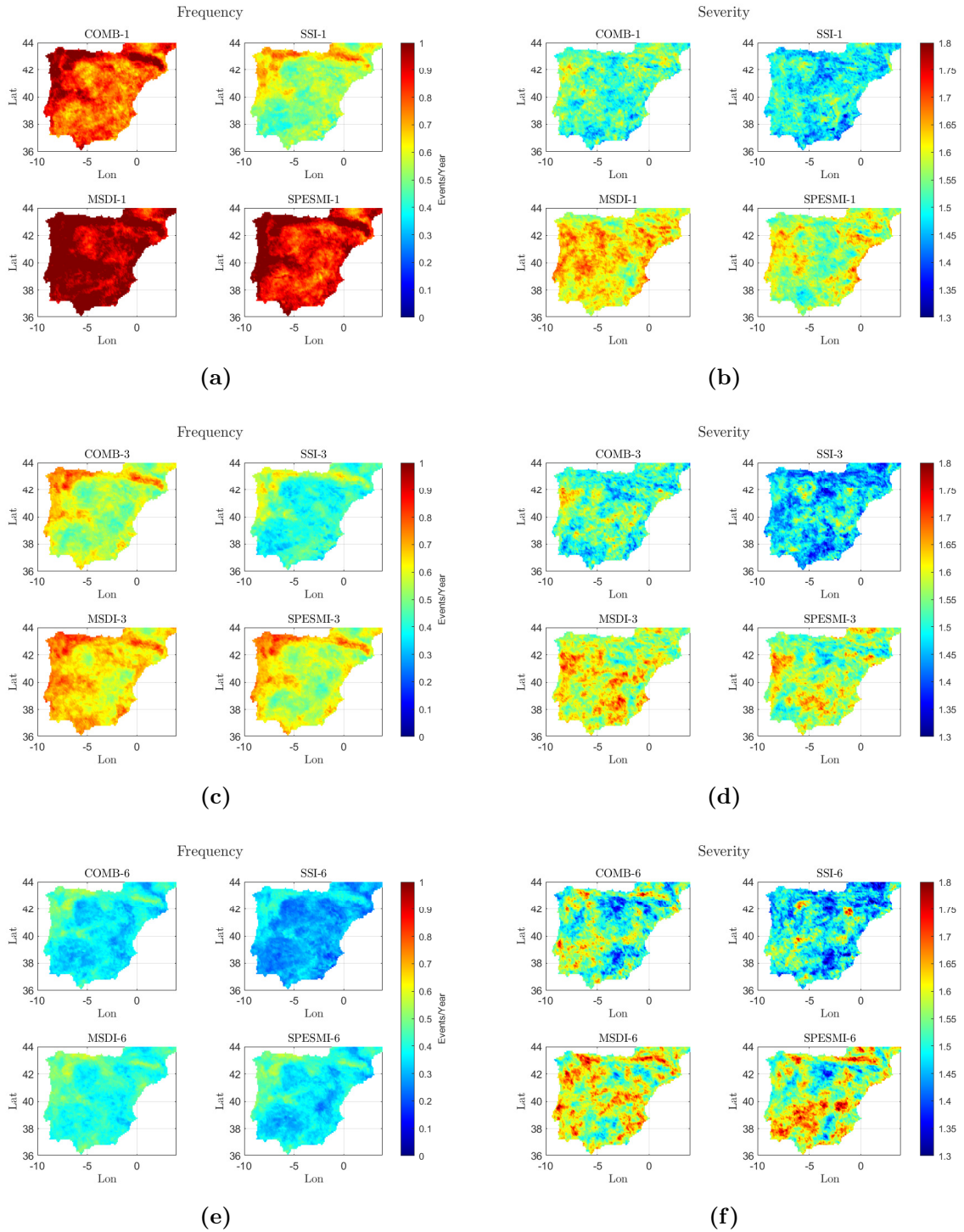


Figure 5.5: Patterns of the average characteristics of drought events on Iberian Peninsula according to 1-, 3- and 6-month time scales for the different AD indices: frequency of severe/extreme droughts per year ((a), (c), (e)), and absolute value of drought severity ((b), (d), (f)).

and MSDI detected multiple drought episodes in several areas, with values ranging from around 1 event/year to 1.2 events/year on average. This is in agreement with

the fact that precipitation, evapotranspiration and soil moisture variables are vital factors to adequately represent agricultural drought conditions (Xu et al. [125]), and especially in large areas with different climate characteristics their combination by using multi-variate indices could better detect the occurrence of drought events. As for the percentage, similarly the patterns of COMB appeared a balance between SSI and MSDI/SPESMI. The most affected zones were found to be the North-West and the Pyrenees for all the indices, indicating that both soil moisture and precipitation/water balance deficits were recurrent. The patterns were analogous for indices at 3- and 6-month timescales, whereas the frequency values were naturally lower due to the longer duration of the considered events. Regarding the average drought severity, a more complex behavior among the AD indices was obtained. Considering the 1-month time scale (Figure 5.5(b)), SSI exhibited a large area of non-severe droughts (severity smaller than 1.5), while COMB, SPESMI and MSDI showed gradually increasing regions affected by severe drought conditions. However, the distribution of the severity values revealed some differences among the indices. For instance, a small fraction of the Centre-East of the IP was one of the most affected zones according to SSI but was not equivalently accounted for by the other indices, especially by MSDI, which retrieved its lowest severity values in the same area. This suggested a balance between the contribution of water balance variables in multi-variate indices, which could significantly impact the effect of soil moisture. Severity also showed a wider range of values for longer time scales. Bi-annual deficits in water balance and soil moisture resulted in large areas affected by severe droughts, with peaks close to extreme droughts in certain regions. On the other hand, even if the 6-month scale showed severity values similar to shorter time scales on average, severity appeared more pronounced or not depending on the region and the index. For example, in the south of Portugal COMB-6, MSDI-6 and especially SPESMI described a higher severity than their corresponding at 1 and 3 months time scales. Other areas, such as the mountain region in the southern part of the IP and the northern peninsular zone, reported the opposite behavior revealing lower severity values at longer time scales.

5.3.2 Propagation from Meteorological to Agricultural Drought

Response Time Scale

The first analyzed parameter related to the drought propagation was the response time scale (RT), which represents the accumulated precipitation deficiency in antecedent RT months causing the agricultural drought, and the shorter it is, the faster the response to meteorological drought. Figure 5.6(a) reports the maximum

Pearson correlation retrieved between 1 month AD indices and SPEI computed from 1- to 48-month time scale over the whole 72 years period for the entire IP, while Figure 5.6(b) indicates the corresponding RT in months for each gridpoint.

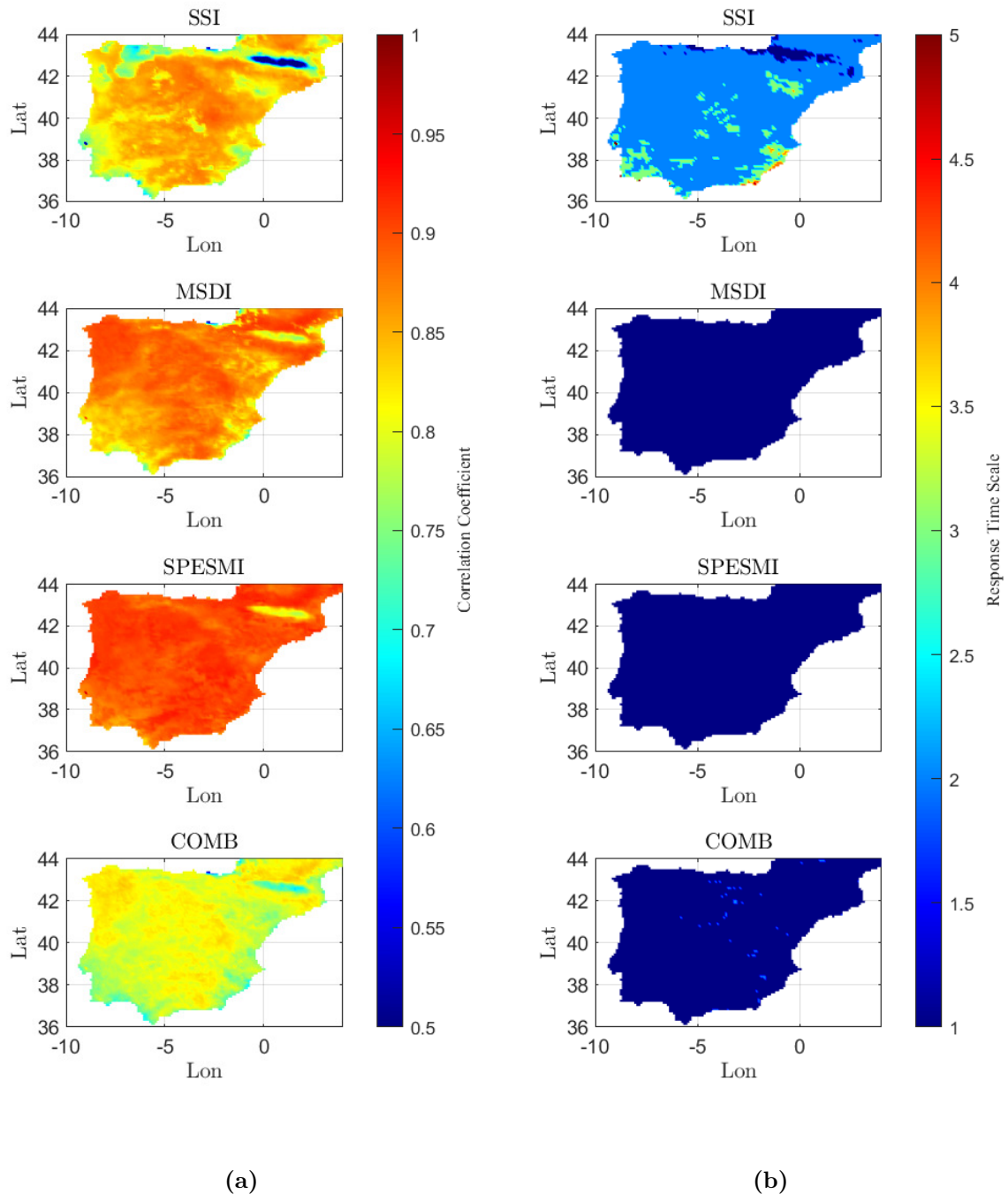


Figure 5.6: (a) Maximum Pearson correlation retrieved between the SPEI at the 1-,2-,..., 48-month time scales and the 1-month time scale AD indices. (b) Corresponding RT in months for each gridpoint.

The first notable element was the high correlation values for small time scales,

in agreement with other studies (Scaini et al. [152]) which retrieved a short RT of agricultural drought to meteorological drought, assessing that usually it is no longer than few months. In particular, for SSI it was obtained $RT = 2$ months for the majority of the IP (except the Pyrenees, where $RT = 1$ month, and $RT = 3-4$ months for some isolated regions, especially in the Southern coastal area), while it was retrieved $RT = 1$ month for MSDI, SPESMI and COMB, suggesting that the contribution of other variables accelerated the response compared to the soil moisture alone. Typically, the inclusion of evapotranspiration in SPESMI produced the highest values of correlation with meteorological droughts detected by SPEI, which was also based on water balance.

Propagation Rate

Taking into account the results regarding RT , the second studied feature of drought propagation was the propagation rate (PR). Since the response time scale of agricultural droughts to meteorological droughts was found to be 1 or 3 months, Figure 5.7 displays the values of PR over the entire IP for these time scales.

The largest values were retrieved for 1-month AD indices and 3-months SPEI, indicating high sensitivity and strong response of agricultural droughts to meteorological droughts at these time scales. High PR values were mostly obtained for MSDI and SPESMI, which revealed $PR > 1$ for the majority of IP over the investigated period. This result was in accordance with the study of Ojeda et al. [153] based on a multi-ensemble of regional climate simulations within the EURO-CORDEX project (Jacob et al. [154]), and implied that a single meteorological drought was capable of generating multiple agricultural drought events due to 1 month deficits in water balance and soil moisture. The lowest PR values were reached for SSI, while COMB showed an intermediate behavior. PR values near 1 were reported for 3 months AD indices, confirming the intense response between the two types of drought also for a longer time scale. The maximum PR was found in the North-Western and in the Centre-Eastern regions of the IP, which therefore resulted the most drought propagation-prone areas.

The 2005 Drought Event

The 2005 drought episode over the IP was selected for a detailed analysis regarding the propagation from meteorological to agricultural drought. To get a first general view of the event, Figure 5.8 shows the temporal evolution of the IP averaged AD indices at 3-month time scale and FAPAR Anomaly from October 2004 to December 2005.

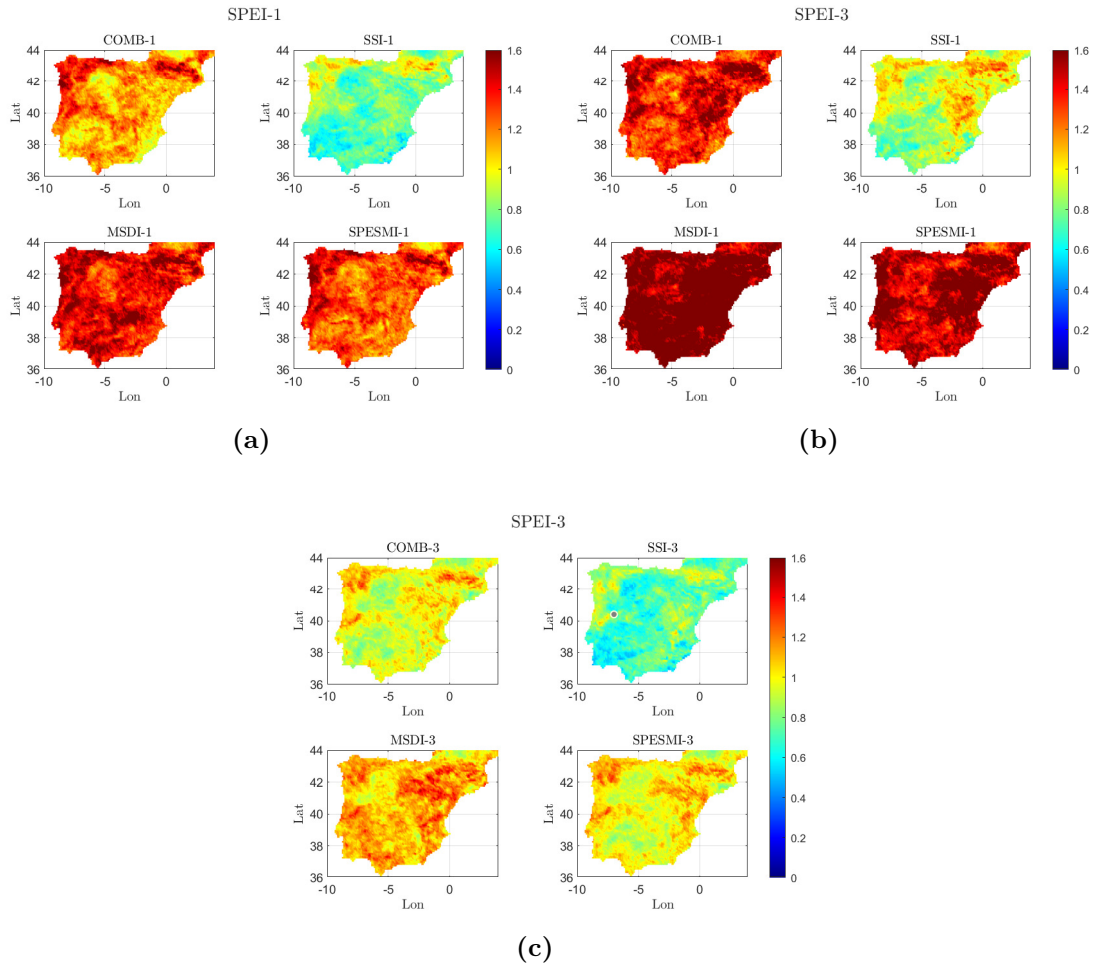


Figure 5.7: Propagation rate considering 1-, 3-month time scales SPEI and 1-, 3-month time scales AD indices.

The four AD indices clearly revealed the occurrence of a seasonal agricultural drought during the considered time window. In particular, according to run theory, MSDI and SPESMI similarly detected the drought onset in December 2004 (indices equal or below -1), with a duration of 9-10 months. On the other hand, SSI identified a 2 months delayed onset in February 2005, while the term was almost the same found for the multi-variate indices. COMB exhibited an intermediate onset in January 2005 and an extent in agreement with the other indices. The most relevant difference was found regarding the severity of the event, which was noticeably higher for MSDI and SPESMI compared to the others. Indeed, whereas for SSI the event could be categorized as moderate drought for the majority of its duration with an aggravation to severe drought only during a fraction of the time, MSDI and SPESMI classified the entire event as severe drought with a further exacerbation to extreme drought in July 2005. Because of the way it was formulated, COMB showed the minimum severity values (since its values could range only between -2 and 1). The FAPAR Anomaly revealed a similar behavior to AD indices in identifying the

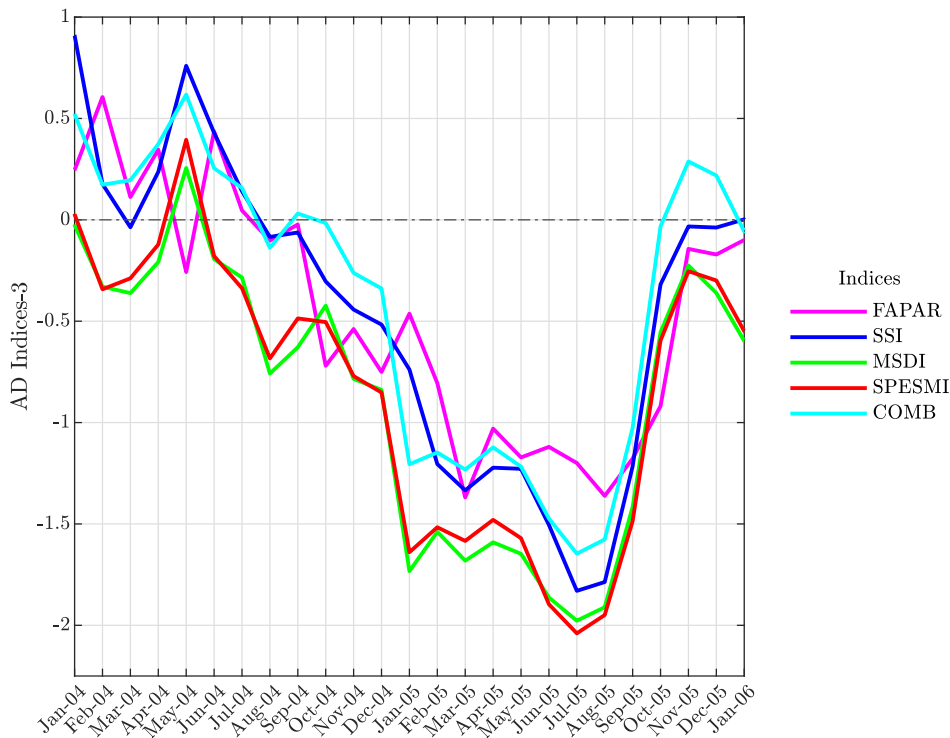


Figure 5.8: Temporal evolution of the IP averaged AD indices at 3-month time scale from October 2004 to December 2005, including FAPAR Anomaly.

drought event, despite suggesting a delayed onset in March 2005 and less severe values.

This picture provided an initial overview of the behavior of the indices during the event, but it was not sufficient to analyze the spatial evolution of the drought phenomenon. For this reason, the monthly patterns of drought indices values during the reference period (October 2004 - December 2005) were investigated. In particular, the variations of the AD indices at 1-month time scale were examined compared to the SPEI progression at 1-month and 3-month time scales, to analyze respectively the propagation from the current month and from the seasonal meteorological water balance deficit to the development of agricultural drought. Figure 5.9 shows the temporal evolution of the meteorological drought identified by SPEI at 1- and 3-month time scales from October 2004 to December 2005 over the whole IP.

According to Figure 5.9(a), the evolution of SPEI calculated at monthly time scale depicted a first moderate drought condition extended over the majority of the IP in December 2004, while February 2005 was identified as the driest month, with large areas subjected to extreme drought. This pattern exhibited a rapid evolution described by two wetter following months, and the severe/extreme drought episode reoccurred in May 2005 initially involving only the South of the IP. This condi-

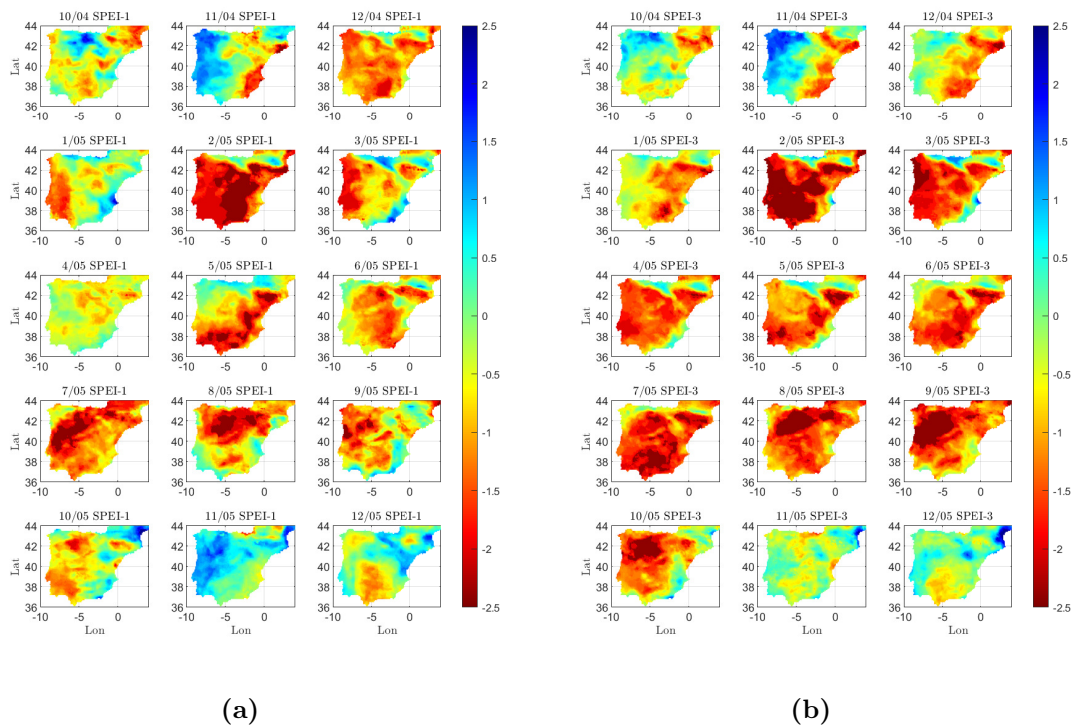


Figure 5.9: Temporal evolution of meteorological drought pattern over the IP according to SPEI at (a) 1- and (b) 3-month time scales, from October 2004 to December 2005.

tions lasted until the end of Summer 2005 (September) with a modified pattern, more concentrated in the Centre and Northern IP. This event provoked the most remarkable impacts in Spain and Portugal, as reported in European Drought Observatory, with a relaxation during the winter of 2005. The evolution of seasonal meteorological drought described in Figure 5.9(b) revealed some similarities, such as the initial peak of drought in February 2005. However, the patterns showed by SPEI-3 appeared more continuous compared to SPEI-1, essentially reporting prolonged drought conditions over the reference period, with a delayed conclusion (extreme drought conditions were retrieved even in October 2005). Also, in this case the driest region resulted the Southern IP, in the beginning, with varying features extending to Central and Northern IP.

In order to observe the evolution of the agricultural drought during the identified meteorological drought conditions, Figure 5.10 depicts the spatial patterns corresponding to the 4 different AD indices at 1-month time scale over the IP.

The onset of agricultural drought in February 2005 was also captured by all the 4 AD indices. However, while COMB, MSDI and SPESMI assessed moderately dry conditions over the IP even from December 2004 except for the eastern coastal region, SSI showed generally normal/wet patterns during the period preceding the drought event. Also, SSI values described overall less severe drought conditions with

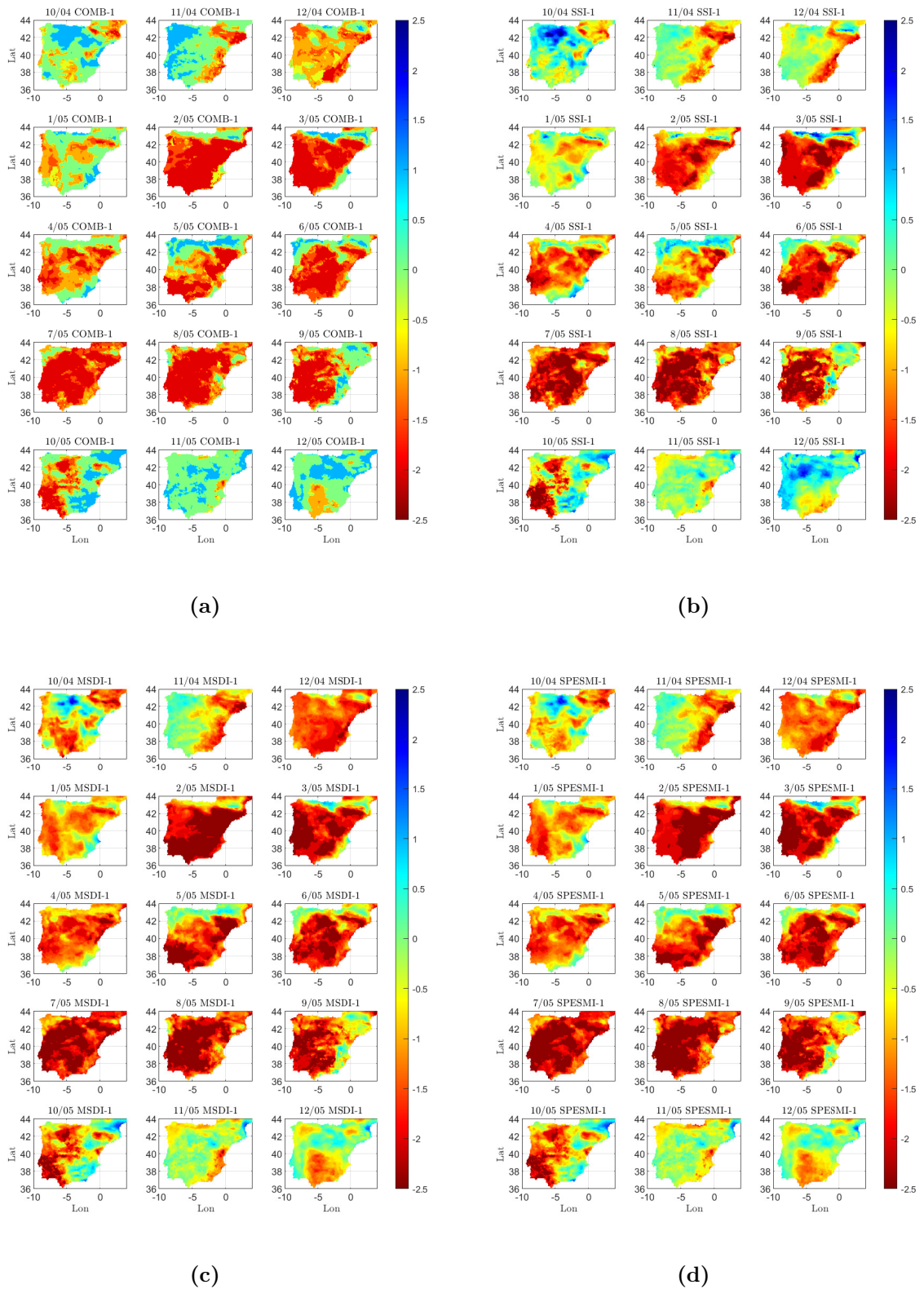


Figure 5.10: Temporal evolution of drought pattern over the IP according to the four AD indices: (a) COMB, (b) SSI, (c) MSDI, and (d) SPESMI at 1-month time scale from October 2004 to December 2005.

respect to the other indices, implying that including other variables than soil moisture allowed to retrieve stronger impacts. Moreover, the patterns represented by SSI were less uniform and homogeneous with respect to those indicated by MSDI and SPESMI, especially observing the first month of the drought occurrence (February 2005). The behaviors of MSDI and SPESMI appeared noticeably congruent, revealing also in this case that the introduction of evapotranspiration only marginally impacted the obtained results. Once again, COMB showed features balanced between the other 3 indices, but the notable similarity between the two multi-variate produced a greater influence on its behavior with respect to SSI. The patterns of the agricultural drought determined by the AD indices were consistent with those identified by SPEI, particularly by SPEI-3, revealing a higher spatial correlation with seasonal meteorological drought than monthly water balance deficits. Except for the aforementioned differences, the four AD indices demonstrated higher severity values compared to SPEI-1 and SPEI-3, assessing that the generated agricultural drought was evaluated severe or extreme in larger areas than the meteorological drought.

Figures 5.9 and 5.10 were useful to qualitatively monitor the spatial details of the 2005 drought evolution. However, to retrieve more quantitative information about the drought propagation, a further investigation was performed. Taking inspiration by the study of Zhu et al. [116], the probability of drought propagation from meteorological to agricultural under different levels of severity was analyzed. In particular, the fraction of the IP subjected to agricultural drought conditioned on the occurrence of meteorological drought was calculated for each month during the October 2004 - December 2005 period. This fraction was defined propagation probability (PP) and it was computed separately for the four AD indices at 1-month time scale distinguishing 3 severity thresholds, namely moderate, severe and extreme. Figure 5.11 represents the temporal evolution of PP for each AD index. Specifically, panels in the same row exhibit the PP values of gradually increasing types of agricultural drought from left to right, and in each panel the 3 different colors refer to the imposed severity threshold of meteorological drought according to SPEI-1. For example, the red line in the first panel of row one exhibits the time evolution of PP for the occurrence of moderate agricultural drought (according to SSI-1) conditioned on the occurrence of severe meteorological drought (based on SPEI-1).

The first notable outcome regarded a common characteristic showed by all the AD indices, i.e. the significant PP increment depending on the enhancement of severity levels of meteorological drought from moderate to extreme, with values close to 1, implying that the likelihood of agricultural drought tended to be higher when the meteorological conditions were drier. Taking the case of the first row (SSI)

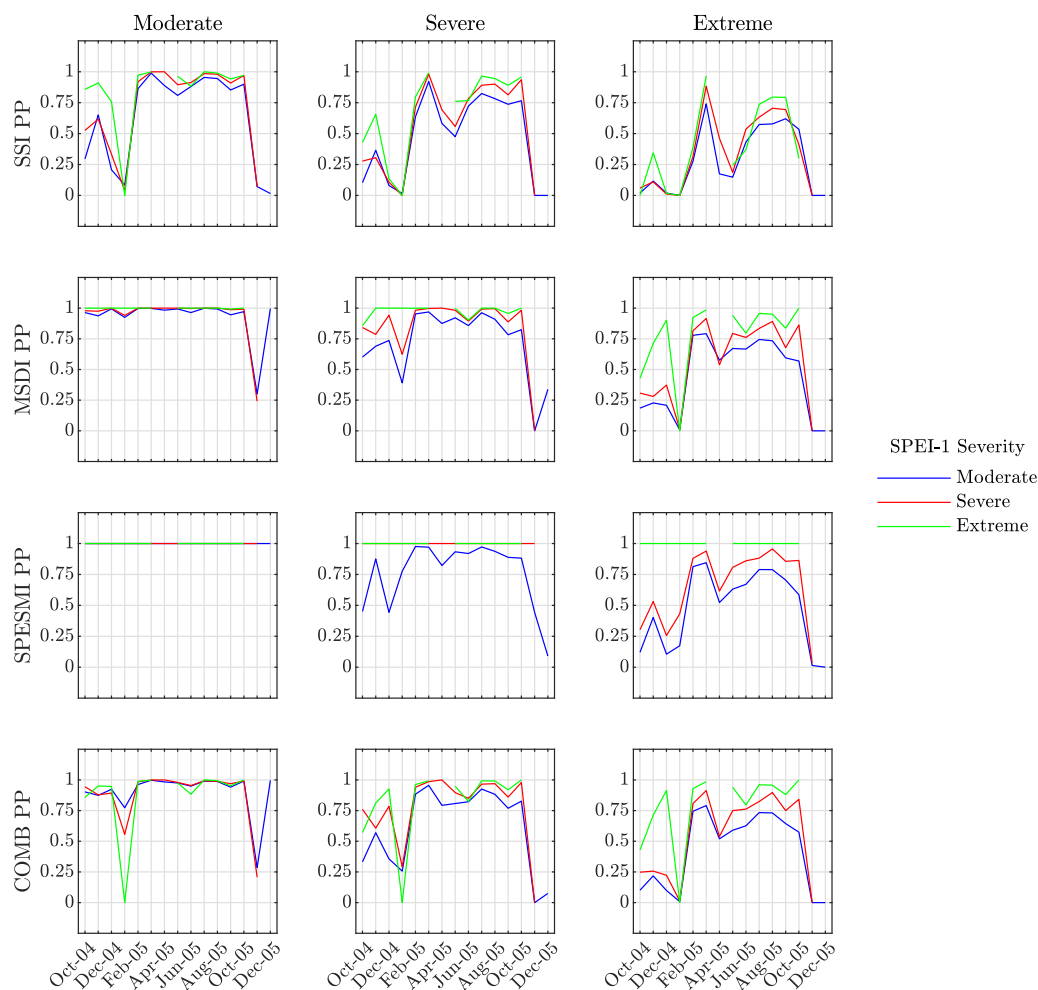


Figure 5.11: Propagation probability (PP) from meteorological drought detected with SPEI-1 to agricultural drought of different severity levels according to 1-month time scale AD indices. The colors distinguish the severity of generating meteorological drought (blue for $SPEI-1 \leq -1$, red for $SPEI-1 \leq -1.5$, green for $SPEI-1 \leq -2$).

as example, areas where extreme meteorological drought developed from February 2005 were very likely to be subjected to a propagation into agricultural drought of various severity levels, with the maximum PP obtained for moderate severity propagation. The almost constant values of $PP = 1$ in the left panels of MSDI and SPESMI assessed that the two multi-variate indices were exceptionally sensitive to moderate agricultural drought propagation, while less prone to severe and extreme. Generally, SSI revealed lower values of PP for the 3 levels of severity compared to the multi-variate indices, whereas COMB once again resulted in a balance between these two typologies of indices. Excluding the exceptional cases reported in the left panels of MSDI and SPESMI, all the indices showed overall high values of PP during the period of the identified drought event, with $PP > 0.5$ for moderate SPEI-

1 severity and $PP > 0.75$ for severe/extreme SPEI-1 severity. Only the two months following the initial drought onset (March and April 2005) exhibited a deflection, meaning that in this period the meteorological drought did not propagate in all the involved regions. Moreover, while for MSDI, SPESMI and COMB the PP values remained above 0.5 during this variation, SSI showed a more considerable reduction reaching $PP < 0.25$.

Then, the same procedure was applied to observe the propagation from seasonal meteorological drought, and in this regard Figure 5.12 shows the behavior of PP for agricultural droughts conditioned on the values of SPEI-3.

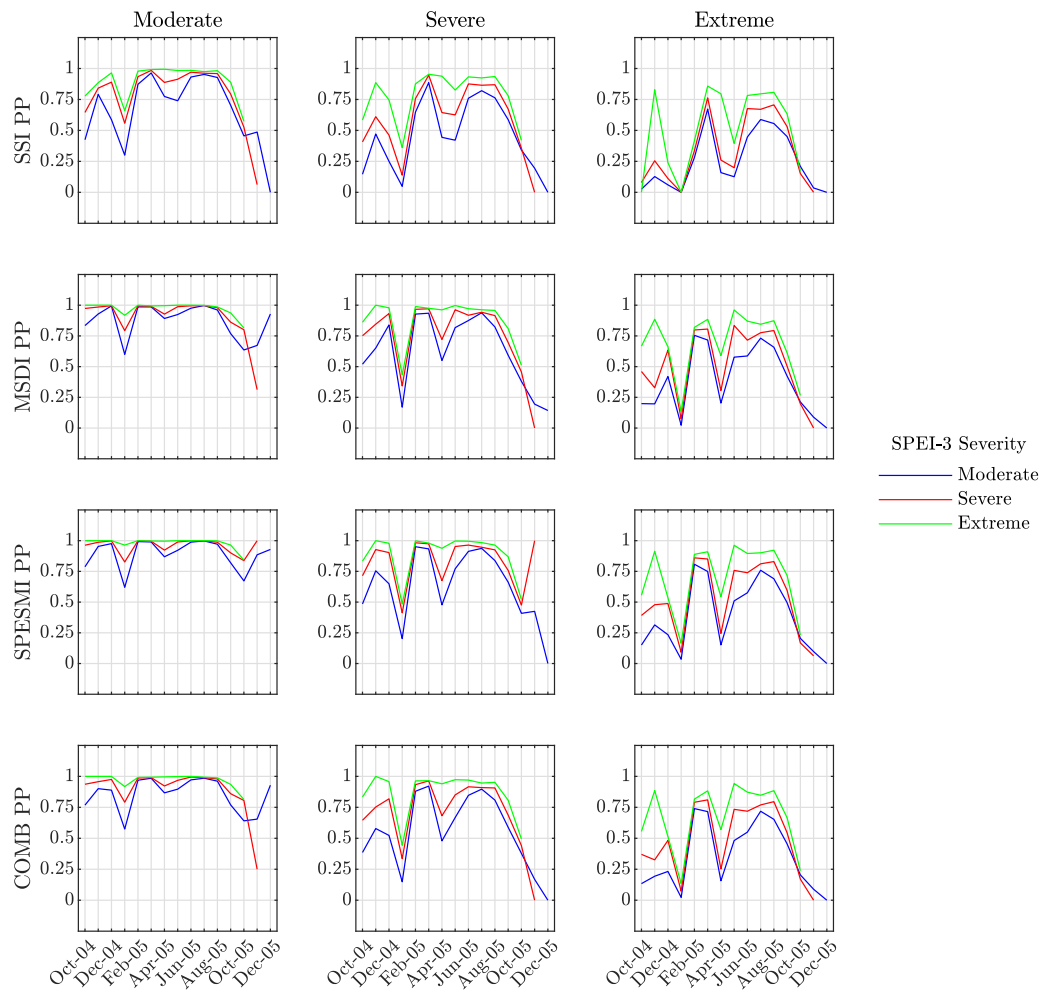


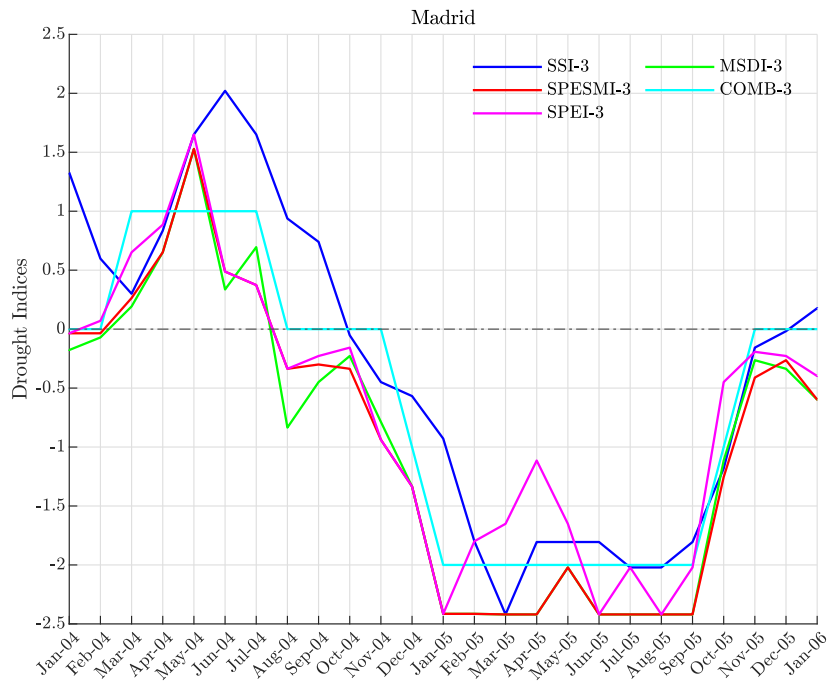
Figure 5.12: Propagation probability PP from meteorological drought detected with SPEI-3 to agricultural drought of different severity levels according to 1-month time scale AD indices. The colors distinguish the severity of generating meteorological drought (blue for $SPEI-3 \leq -1$, red for $SPEI-3 \leq -1.5$, green for $SPEI-3 \leq -2$).

Also in this case, the notable PP increment with meteorological drought severity levels gradually enhancing from moderate to extreme was evident. At the same time,

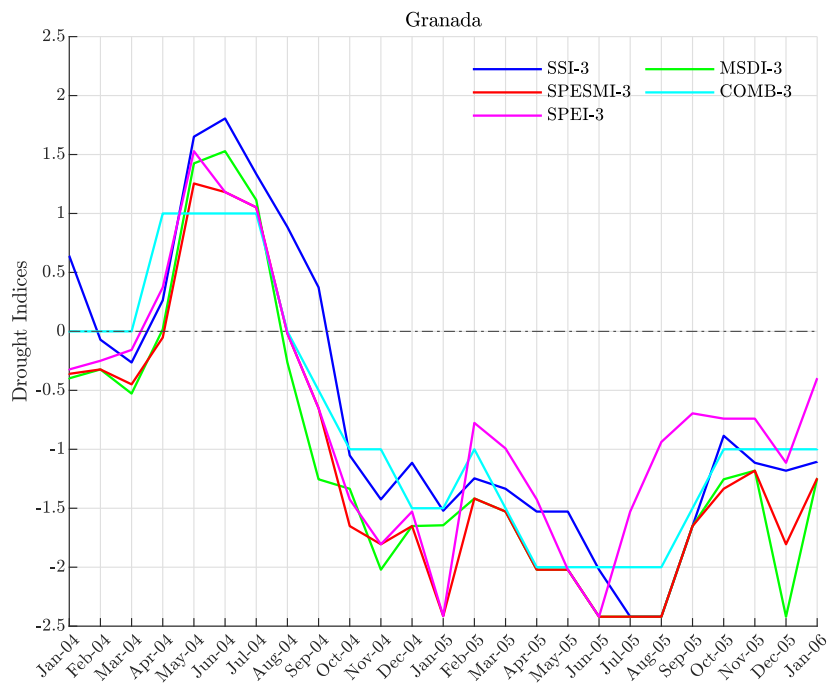
the maximum values of PP were found for moderate agricultural droughts, signifying that the propagation to more severe droughts were less likely to occur. Compared to the outcomes reported in Figure 5.11, the propagation from seasonal meteorological drought revealed a more homogeneous behavior among the AD indices. Both the maxima/minima of PP and the PP signal evolution exhibited common features. As the previous case, the lowest value of PP was reached in March-April 2005, suggesting that during this period the meteorological drought was present, but without propagating into agricultural. Additionally, in particular the panel regarding severe and extreme agricultural drought displayed smaller PP with respect to the SPEI-1 example, therefore the seasonal drought was in general less efficient in propagation with respect to drought provoked by monthly water balance deficits.

To further investigate the 2005 drought event, two areas of the Iberian Peninsula that showed significant variations during the event were selected: the Centre and the South. In order to monitor changes in drought indices and evaluate the lag time (LT), one city was chosen to represent each region. Following the approach of García-Herrera et al. [155], Madrid was chosen as the representative location for the IP Centre, and Granada was selected for the IP South. Figure 5.13 shows the 3-month time scale drought indices for these cities from January 2004 to January 2006. The seasonal drought was considered, as it is characterized by smoother and slower variations than the 1-month drought and provides more significant information for the calculation of LT .

To obtain LT , the differences of drought onset time between SPEI and the AD indices were calculated. Focusing on Madrid, the multivariate indices showed $LT \sim 0$, while $LT \sim 2$ months for SSI, since in that city the agricultural drought resulted to start in February 2005 while the meteorological in December 2004. Also, AD indices revealed low variability with respect to SPEI, whose high range of values indicating different meteorological drought conditions was not reflected in modifications of agricultural droughts. In this case, the propagation of meteorological drought evolution produced prolonged and almost constant effects in the agricultural droughts, especially according to COMB. The situation for Granada was slightly different. Firstly, the meteorological drought onset preceded by 2 months that occurred in Madrid (October 2004), and it was simultaneous to all AD indices, so $LT \sim 0$. Actually, MSDI showed the onset of agricultural drought even 1 month before SPEI, thus the nature of this detected event was not associated to drought propagation. In Granada, even though the onset lag time was approximately zero between meteorological and agricultural drought, it is important to notice that the duration of the two phenomena was not equivalent. That is to say that, while SPEI returned to assess dry meteorological conditions without the presence of drought in August



(a)



(b)

Figure 5.13: Local temporal evolution of different drought indices at 3-month time scale in Madrid (a) and Granada (b) from January 2004 to January 2006.

2005, SSI and COMB estimated the end of agricultural drought in October 2005, and MSDI and SPESMI required even more time.

5.4 Synthesis of the Main Results

This second part of the thesis was dedicated to the study of drought phenomenon. In particular, the propagation from meteorological to agricultural drought was analyzed, identifying the meteorological drought events through the SPEI index, while for agricultural droughts 3 non-parametric agricultural drought (AD) indices were employed, the uni-variate SSI based on soil moisture, and the multi-variate MSDI and SPESMI, which also consider precipitation and water balance, respectively. Also, a new combined agricultural drought index (COMB) was proposed. The study was conducted on a multi-annual reanalysis dataset (1950-2021) regarding the Iberian Peninsula, a recognized European drought hot-spot. Considering the characterization of agricultural droughts, SSI revealed a remarkably reduced area of the IP subjected on average by severe/extreme droughts (40%) with respect to the other AD indices (75%). Also, the frequency of severe/extreme drought events per year described a higher sensitivity of multi-variate AD indices compared to SSI, together with a lower severity. Concerning the proper mechanism of propagation from meteorological to agricultural drought, the calculation of the response time scale (RT) produced small values for all the AD indices, with $RT = 2$ months for SSI and $RT = 1$ month for MSDI, SPESMI and COMB. Moreover, large propagation rate values ($PR \geq 1$) were retrieved examining the propagation from monthly/seasonal meteorological to monthly/seasonal agricultural drought, implying that a single meteorological drought was capable of generating multiple agricultural drought events, and the lowest values were obtained by SSI. The analysis of the 2005 drought episode allowed to identify for SSI a 2-month delayed onset with respect to other AD indices, while the term was almost coincident (October 2005), together with smaller severity values. The patterns of the agricultural drought determined by the AD indices were consistent with those detected by SPEI, especially assessing a higher spatial correlation with seasonal than monthly meteorological drought. The severity values of the four AD indices were generally higher than those of SPEI-1 and SPEI-3, indicating that the agricultural drought impacts were more severe and extensive than the meteorological drought. Large values of propagation probability PP from monthly meteorological drought to monthly agricultural drought were retrieved during the 2005 drought event, with increasingly PP for drier meteorological conditions. Lower PP values were obtained for propagation from seasonal meteorological drought to monthly agricultural drought. The computation of lag time (LT) reported values ranging from $LT \sim 0$ to $LT \sim 2$ months for SSI depending on the location, while the multi-variate indices showed a constant $LT \sim 0$. These values close to 0 suggested interest for a future analysis concerning sub-monthly features of LT .

Chapter 6

Conclusion

6.1 Summary of Relevant Outcomes

The thesis provided a comprehensive analysis of heat-related phenomena and their relationships at different spatio-temporal scales, with a focus on two distinct aspects. The first part of this work addressed an important and novel topic related to the influence of large-scale heatwave events on the local-scale urban heat island (UHI) effect. In this regard, temperatures recorded by a large number of meteorological stations in 37 European cities over a 20-year period were analyzed, furnishing a broad perspective on the behavior of UHI during heatwaves compared to standard meteorological condition across different climate zones and urban context. The study provided new insights into the relationship between these two phenomena, which have not been fully explored in literature. In particular, although no significant modifications were retrieved for daytime UHI, revealing a negligible impact of large-scale extreme temperatures on the local urban climate, interesting features emerged regarding the nocturnal UHI. The majority of the considered cities exhibited an increase of nighttime UHI effect concurrently with heatwave episodes, on average about 0.7 °C, also with an increment in frequency of days subjected to reasonably positive UHI. This finding highlights the potential intensified nighttime discomfort in urban areas during heatwaves, which may ultimately result in higher mortality rates, with major diseases in densely built zones. The study revealed an absence of linear correlations between the intensity of the UHI modifications and some features of the analyzed cities and related stations, suggesting that the UHI response to heatwaves is complex and dependent on multiple factors. The exacerbation of the nocturnal UHI during heatwave periods was explained by a different response to heating of urban and rural temperature, showing the former a larger and more persistent increase during a heatwave, which gave partial insights into the mechanisms underlying the relationship between heatwaves and UHI. Moreover,

the study found that the maximum amplification of UHI occurred 3 days after the onset of the heatwave. However, an increase in the temperature difference between urban and rural areas was observed even one week before the peak of the heatwave. This outcome suggests that there may be implications for early warning systems for heatwaves. The investigation of the relationship between large-scale temperature anomalies and UHI highlighted a smooth and continuous dependence, but with a strong variability. Moreover, the lack of a threshold behavior in this relationship suggested that large-scale temperature variability can affect the local-scale UHI even in different conditions than during extreme events. Additionally, the comparison with the UrbClim model outputs confirmed the result about the UHI strengthening during heatwave episodes, with an intensity independent of the climate zone. This finding provided an important validation for the methodology used in the study.

In summary, this study presented observational evidence of the synergistic interaction between nocturnal UHI and heatwaves, utilizing a homogeneous methodology for *in-situ* observations in a large cluster of European cities. The results supported the conclusion that UHI exacerbates during heatwave events in the majority of European cities, in agreement with the increasingly dominant paradigm in scientific literature (Kong et al. [18], Zhao et al. [28], Miao et al. [40]). Furthermore, this study suggested that the conclusion reached by Scott et al. [41], who found a reduction of UHI during hot days in many US cities using a similar methodology, does not hold for the majority of European cities analyzed in this study. This thesis adds to the existing literature on single case studies (e.g. Founda et al. [43], Nicholson [44], Unger et al. [45]). The findings of the study have important implications for urban planning and management, particularly in the context of climate change, where heatwaves are expected to become more frequent and intense.

The second part of the thesis dealt with the characteristics and temporal patterns of drought, with a focus on the transition from meteorological to agricultural drought, the first stage in the spread of drought. The study drew on a multi-year reanalysis dataset spanning 1950 to 2021, and covering numerous drought events over the Iberian Peninsula, an established drought hotspot in Europe. The analysis employed multiple non-parametric drought indices ranging from uni-variate to multi-variate in order to separately take into account the various physical quantities involved in the process. Meteorological droughts were identified using the SPEI index, a proven tool for this purpose, while the detection of agricultural droughts relied on three non-parametric agricultural drought (AD) indices: SSI (uni-variate), MSDI and SPESMI (multi-variate), which separately accounted for soil moisture, precipitation, and evapotranspiration. In addition, a novel combined agricultural drought index (COMB) was proposed to enhance the accuracy of drought detection. Once

again, it is worth emphasizing that the use of a large spatial area and a multi-year dataset was crucial in providing a comprehensive understanding of the propagation process. The study began with characterizing drought events across different time scales (monthly, seasonal, and six-monthly) over the Iberian Peninsula throughout the entire dataset period. Results indicated a slight trend towards increased dryness during the last two decades, as supported by both the SPEI and AD indices. These findings were consistent with those of Coll et al. [151], who analyzed meteorological droughts using similar indices but in their parametric form. Moreover, the AD indices resulted effective in assessing vegetation stress during drought events, even though they did not reveal all the variations identified by the Fraction of Absorbed Photosynthetically Active Radiation (FAPAR) anomaly values, which take into account other factors than rainfall and soil moisture deficits, such as plant diseases. In terms of the average characteristics of agricultural drought events across the Iberian Peninsula, it was observed that SSI identified a significantly smaller area affected by severe or extreme droughts. The frequency values of severe or extreme drought events per year indicated that multi-variate AD indices were more sensitive than SSI, although they had lower severity. Moreover, when considering long time scales, the severity values covered a wider range than that of monthly time scales, including both the most and the least severe values. In the second step, the mechanism of propagation from meteorological to agricultural drought was analyzed. The response time scale (RT) was calculated for the AD indices, and small values were obtained, in agreement with other studies (Scaini et al. [152]). Specifically, in the majority of the Iberian Peninsula, an RT of 2 months was found for SSI, while MSDI, SPESMI, and COMB had an RT of 1 month, suggesting that the contribution of water balance accelerated the response compared to the effect of soil moisture alone. The transition from monthly/seasonal meteorological drought to monthly/seasonal agricultural drought was analyzed and a high propagation rate ($PR \geq 1$) was found, indicating that multiple agricultural drought events could be generated from a single meteorological drought. This was observed in all the AD indices, with the lowest values being obtained by SSI. The analysis of the 2005 drought episode was valuable in examining the temporal and spatial characteristics of drought propagation. In contrast to global results described in Zhu et al. [116], the time evolution of seasonal agricultural drought showed a 2-month delayed onset for SSI compared to other AD indices, while the termination time was almost coincidental. Additionally, the severity values indicated by SSI were lower. The patterns of agricultural drought determined by the AD indices were consistent with those identified by SPEI, particularly showing a higher spatial correlation with seasonal rather than monthly meteorological drought. The evaluation of propagation

probability (PP) from monthly meteorological drought revealed high values of PP during the period of the identified drought event. Monthly agricultural drought tended to occur more frequently in the presence of increasingly drier meteorological conditions. In contrast, smaller PP values were obtained from seasonal meteorological to monthly agricultural drought, indicating a reduced propagation efficiency compared to meteorological drought caused by monthly water balance deficits. The computation of lag time (LT) revealed different outcomes for SSI depending on the location considered, with values ranging from $LT \sim 0$ to $LT \sim 2$ months, while the multivariate indices consistently showed $LT \sim 0$ regardless of the position.

In conclusion, this study employed a climatological approach to investigate the diverse typologies and temporal scales of drought. The innovative aspect of this research lies in its comprehensive dataset, covering a lengthy time period and utilizing a variety of standardized indices that consider not only soil moisture but also other significant factors, such as precipitation and evapotranspiration. Through this analysis, it was found that multi-variate indices are more effective in identifying severe drought events compared to uni-variate indices, suggesting that other variables contribute to a faster response compared to soil moisture alone. Moreover, the study introduced a novel combined agricultural drought index that balances the characteristics of the other adopted indices, which could be a valuable resource for future investigations. Overall, this work provides valuable insights into drought propagation from meteorological to agricultural conditions, contributing to a deeper understanding of this relatively unexplored phenomenon.

6.2 Future Developments

Regarding the first part, the statistical analysis of temperature data in a large ensemble of cities with remarkably heterogeneous characteristics described in this thesis is probably inadequate to shed light on the details of physical mechanisms regulating the UHI-heatwave interaction and of drivers at play. However, it can provide valuable information in the effort to conceptualize the UHI-heatwave relationship and its multi-scale nature. Indeed, being able to detect features of the UHI-heatwave synergy that are common to many cities can provide guidance to develop simple models on how synoptic meteorological conditions affect the UHI, and can foster the development of simplified large-scale methodologies for the assessment of health-related threats of temperature extremes in urban environment. For instance, results in Figures 3.12(c) and 3.14 suggest that, while UHI and large scale temperature are strongly correlated, heatwave phenomena should exhibit synoptic conditions that favour a strong UHI even when the large-scale temperature

anomaly of the heatwave is not mature. This is an indication to further explore the UHI-heatwave relationship focusing also on the synoptic scale circulation before the heatwave has reached a mature stage. Along these lines, future studies could look for meteorological variables other than temperature that exhibit a sharp collapse like the one found in Figure 3.12(c). Moreover, the temporal asymmetry found in the UHI-heatwave lead-lag relationship can *per se* provide guidance in a prospective development of early warning systems.

To further advance our understanding of the complicate interaction between urban heat islands (UHIs) and heatwaves, several next steps could be taken. Firstly, there is a need to investigate the mechanisms that regulate the behavior of UHI during summer heatwaves compared to standard meteorological conditions. This can be achieved through conducting numerical simulations using mesoscale models. The high-resolution outputs obtained from these models can be used to validate the temperature values presented in this thesis, and extend the limited temporal range of C3S products to cover the entire 20-year period analyzed. Additionally, these simulations can be used to examine other variables that may undergo modifications under heatwave conditions, such as humidity. Moreover, it is important to investigate the main causes of nocturnal UHI enhancement. The strength of nocturnal UHI is commonly more pronounced during clear-sky conditions and weak winds, which are also typical during heatwaves. It would be worthwhile to compare the intensity of UHI between heatwave and non-heatwave days, selecting only those days with low cloud cover and weak winds, to examine the influence of heatwaves on UHI while controlling for other factors that may affect UHI intensity. To further enhance the characterization of UHI based on land cover and Local Climate Zone (LCZ) classification, it would be worthwhile to take advantage of high-resolution models as suggested by Kong et al. [18]. This approach would distinguish the varying impacts of heatwaves on different land cover types such as low-intensity urban areas, high-intensity urban areas, forests, grasslands, croplands, etc. This would provide a more detailed assessment compared to the observational dataset. Studying the hourly diurnal behavior of UHI would also be an interesting avenue of research. This would allow for the estimation of the evolution of the spatial pattern of UHI over time and an assessment of where the observed temporal shift is confirmed. Finally, in the context of global warming, it would be enlightening to examine the interactions between UHI and heatwaves in European cities under future scenarios as recommended by Ma et al. [156], taking into account forthcoming urban structural modifications as discussed by Silva et al. [157]. Overall, these investigations would provide a more comprehensive understanding of the complex interactions between UHI and heatwaves. This understanding could potentially inform strategies

for mitigating the effects of UHI on urban populations.

Regarding the second part of the thesis, this study provided valuable insights into the mechanisms of drought propagation from meteorological to agricultural, and this knowledge could be useful for drought monitoring and management. It could also contribute to the development of more accurate and reliable drought forecasting models, which are essential for effective drought planning and response. However, there are currently a number of challenges that need to be addressed in drought propagation analysis. One of these challenges is the complicated comparison between studies that refer to distinct indices and approaches. Another difficulty is the need to constrain the analysis to single factors, which can prove to be a complex task. Future studies on agricultural drought propagation will need to address these challenges and involve the integration of other techniques beyond statistical analysis based on run theory. For example, a probabilistic approach, as demonstrated in the study conducted by Wong et al. [158], could be extended to explore further analysis techniques. Moreover, the phenomenon of global warming highlights the importance of conducting studies that address the changing environment of the future, taking into account non-stationary conditions. To this end, a study based on a multi-ensemble of regional climate simulations within the EURO-CORDEX project was set up, analyzing the non-parametric SSI, MSDI, and SPESMI indices for different warming scenarios (1.5, 2, 3, 4 °C from 1980 to 2099) relative to the pre-industrial period (1861-1900). Future work could build upon this investigation by extending it to the newly developed COMB index and including an ensemble analysis that incorporates other types of meteorological and agricultural drought indices from existing literature. Moreover, future studies could investigate more in detail the lead time between meteorological drought onset and agricultural drought onset, and how this changes depending on the location and the type of crop. This could help to achieve a more comprehensive understanding of agricultural drought propagation, leading to improved drought monitoring and early warning. Overall, the study of drought propagation from meteorological to agricultural is an important area of research that has the potential to contribute significantly to our understanding of drought and its impacts. By addressing these challenges and incorporating new techniques, future studies that follow the methodology proposed in this thesis could make significant contributions to this field, thereby aiding in the improvement of drought prediction and response.

Supplementary Figures

This section provides additional figures that offer supplementary information about certain aspects of the thesis.

In particular, regarding the study of interactions between urban heat island and heatwaves in European cities through observations, Figure S1 and S2 show the distribution of ECA&D and WMO meteorological stations composing the selected dataset.

Concerning the study about drought, Figure S3 represents the patterns of the average duration of severe/extreme droughts and the average drought magnitude across the IP according to 1-, 3- and 6-month time scale for the different AD indices.

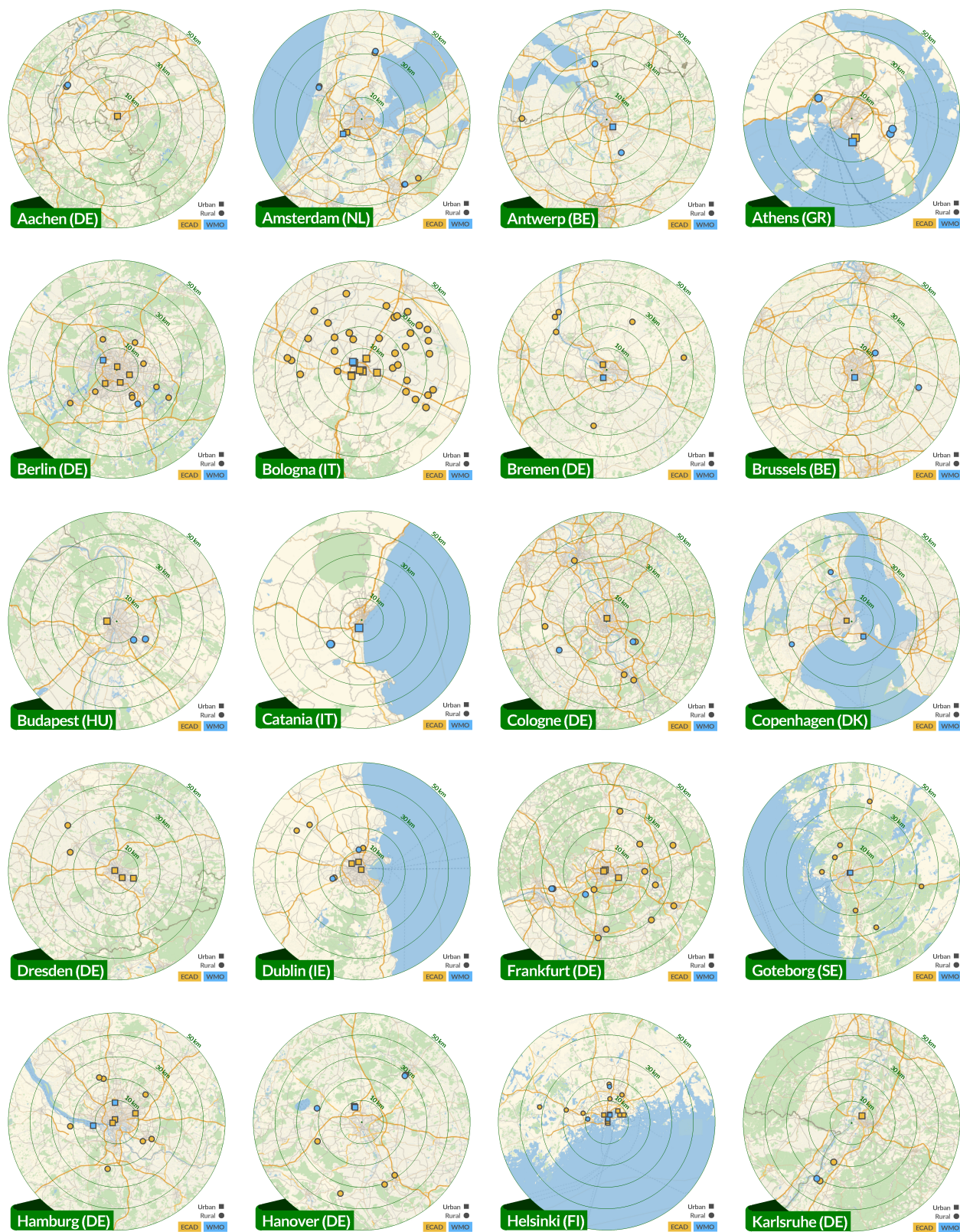


Figure S1: Maps of meteorological stations: locations of employed urban and rural meteorological stations for each city analyzed, distinguishing ECA&D in green and WMO in blue.

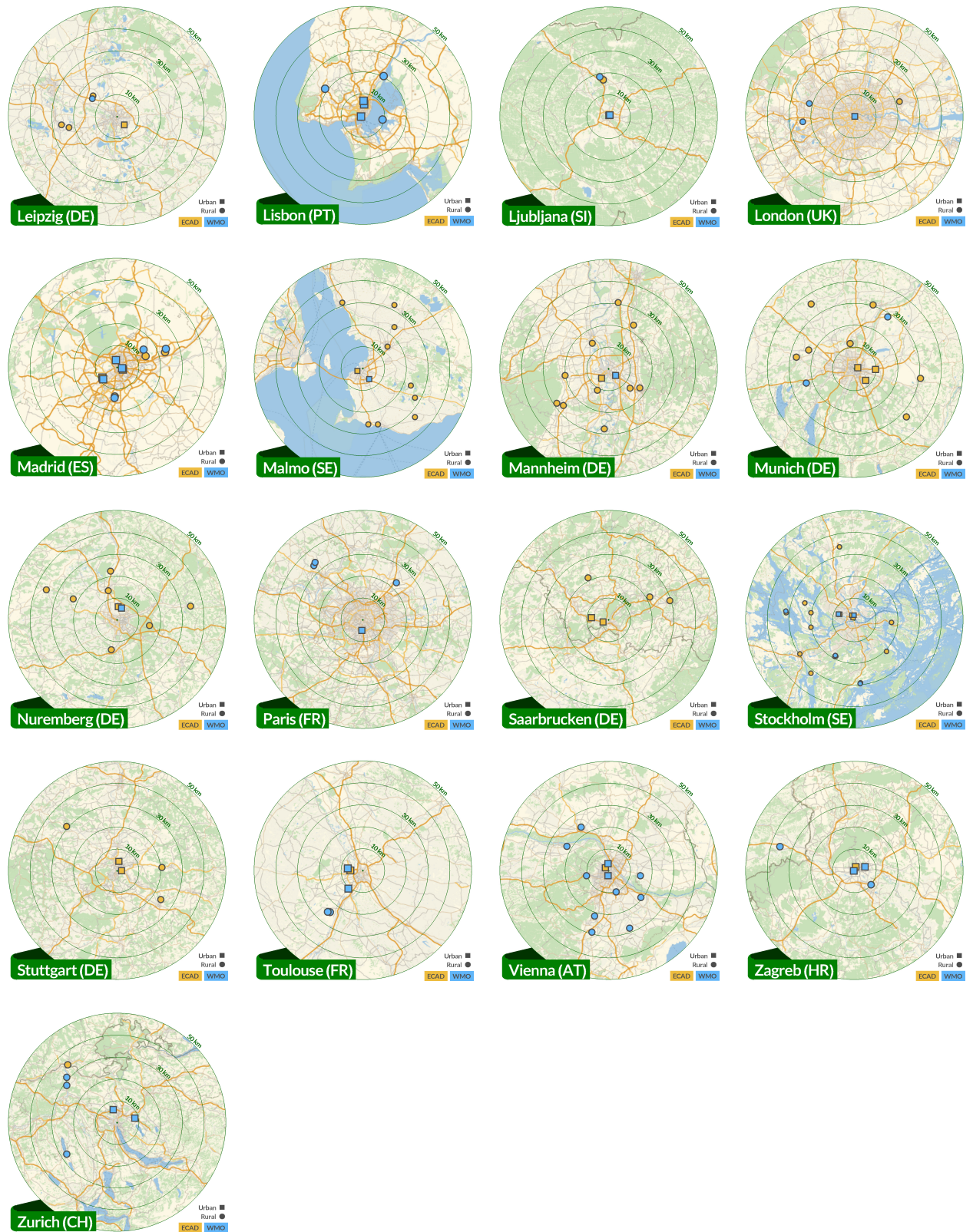


Figure S2: Maps of meteorological stations: locations of employed urban and rural meteorological stations for each city analyzed, distinguishing ECA&D in green and WMO in blue.

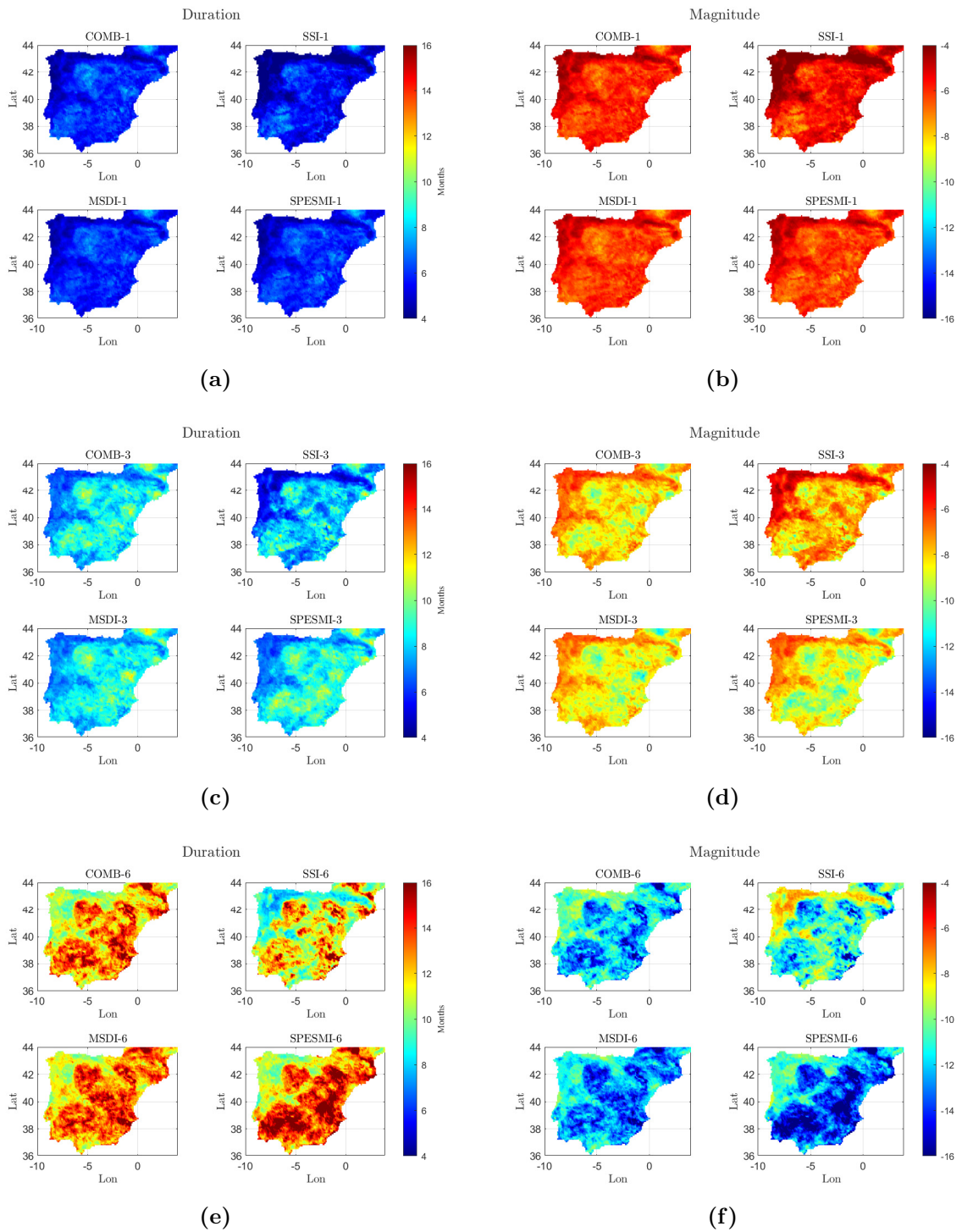


Figure S3: Patterns of the average characteristics of drought events on the IP according to 1-, 3- and 6-month time scale for the different AD indices: duration in months of severe/extreme droughts ((a), (c), (e)), and drought magnitude ((b), (d), (f)).

Acknowledgements

I would like to dedicate a few words to thank the people who have allowed me to complete this work. First of all, I enormously thank Professor Silvana Di Sabatino for giving me the opportunity to undertake this path and for supervising my work by making her great experience available to me. After that, I would like to infinitely thank Doctor Paolo Ruggieri and Doctor Leonardo Aragão, who followed my thesis project closely, offering me valuable advices and helping me to improve various aspects of my work, as well as supporting me in times of difficulty. I would like to thank Doctor Marco Antonio Santo, who was the first person to introduce me to the Atmospheric Physics group of the University of Bologna and who gave me interesting ideas to think about. Sincere thanks to Professor Sonia Raquel Gàmiz-Fortis and Doctor Matilde Garcìa-Valdecasas Ojeda, who kindly hosted me at the University of Granada and with whom a fruitful collaboration relationship began, I thank them for their remarkable availability and professionalism. Finally, I thank Francesca and all the people who have been close to me during this long journey, and especially my parents who have never stopped making me feel their support.

Bibliography

- [1] Masson-Delmotte V, Zhai P, Pirani A, Connors S L, Péan C, Berger S, Caud N, Chen Y, Goldfarb L, Gomis M I, Huang M, Leitzell K, Lonnoy E, Matthews J B R, Maycock T K, Waterfield T, Yelekçi O, Yu R and Zhou B. IPCC, 2021: Summary for Policymakers. *Climate Change 2021: The Physical Science Basis. Contribution of Working Group I to the Sixth Assessment Report of the Intergovernmental Panel on Climate Change*, 2021.
- [2] Brown O. The Clausius-Clapeyron equation. *Journal of Chemical Education*, 28(8):428, 1951.
- [3] Watts N, Amann M, Arnell N, Ayeb-Karlsson S, Beagley J, Belesova K, Boykoff M, Byass P, Cai W, Campbell-Lendrum D and others. The 2020 report of the Lancet Countdown on health and climate change: responding to converging crises. *The Lancet*, 397(10269):129–170, 2021.
- [4] De Bono A, Peduzzi P, Kluser S and Giuliani G. Impacts of summer 2003 heat wave in Europe. 2004.
- [5] Guha-Sapir D, Below R and Hoyois P. EM-DAT: the CRED/OFDA international disaster database. 2016.
- [6] Barriopedro D, Fischer E M, Luterbacher J, Trigo R M and García-Herrera R. The hot summer of 2010: redrawing the temperature record map of Europe. *Science*, 332(6026):220–224, 2011.
- [7] Guerreiro S B, Dawson R J, Kilsby C, Lewis E and Ford A. Future heat-waves, droughts and floods in 571 European cities. *Environmental Research Letters*, 13(3):034009, 2018.
- [8] Fischer E M and Schär C. Consistent geographical patterns of changes in high-impact European heatwaves. *Nature geoscience*, 3(6):398–403, 2010.

- [9] Perkins-Kirkpatrick S E and Gibson P B. Changes in regional heatwave characteristics as a function of increasing global temperature. *Scientific Reports*, 7(1):1–12, 2017.
- [10] Bekiashev K and Serebriakov V. World Meteorological Organization (WMO). In *International Marine Organizations*, pages 540–552. Springer, 1981.
- [11] Coughlan MJ. A comparative climatology of blocking action in the two hemispheres. *Australian meteorological magazine Melbourne*, 31(1):3–13, 1983.
- [12] Nakamura N and Huang C. Atmospheric blocking as a traffic jam in the jet stream. *Science*, 361(6397):42–47, 2018.
- [13] Meehl G and Tebaldi C. More intense, more frequent, and longer lasting heat waves in the 21st century. *Science*, 305(5686):994–997, 2004.
- [14] Miralles D, Teuling A, Van Heerwaarden C and Vilà-Guerau de Arellano J. Mega-heatwave temperatures due to combined soil desiccation and atmospheric heat accumulation. *Nature geoscience*, 7(5):345–349, 2014.
- [15] Miralles D, Gentine P, Seneviratne S and Teuling A. Land-atmospheric feedbacks during droughts and heatwaves: state of the science and current challenges. *Annals of the New York Academy of Sciences*, 1436(1):19–35, 2019.
- [16] World Bank. <https://www.worldbank.org/en/home>.
- [17] Oke T R. The energetic basis of the urban heat island. *Quarterly Journal of the Royal Meteorological Society*, 108(455):1–24, 1982.
- [18] Kong J, Zhao Y, Carmeliet J and Lei C. Urban Heat Island and Its Interaction with Heatwaves: A Review of Studies on Mesoscale. *Sustainability*, 13(19):10923, 2021.
- [19] Pagano T and Durham R. Moderate resolution imaging spectroradiometer (MODIS). In *Sensor Systems for the Early Earth Observing System Platforms*, volume 1939, pages 2–17. SPIE, 1993.
- [20] Baldauf M, Seifert A, Förstner J, Majewski D, Raschendorfer M and Reinhardt T. Operational convective-scale numerical weather prediction with the COSMO model: Description and sensitivities. *Monthly Weather Review*, 139(12):3887–3905, 2011.
- [21] Hurrell J, Holland M, Gent P, Ghan S, Kay J, Kushner P, Lamarque J-F, Large W, Lawrence D, Lindsay K and others. The community earth system model: a

- framework for collaborative research. *Bulletin of the American Meteorological Society*, 94(9):1339–1360, 2013.
- [22] Powers J, Klemp J, Skamarock W, Davis C, Dudhia J, Gill D, Coen J, Gochis D, Ahmadov R, Peckham S and others. The weather research and forecasting model: Overview, system efforts, and future directions. *Bulletin of the American Meteorological Society*, 98(8):1717–1737, 2017.
- [23] Oke T R, Mills G, Christen A and Voogt J A. *Urban climates*. Cambridge University Press, 2017.
- [24] An N, Dou J, González-Cruz J E, Bornstein R D, Miao S and Li L. An observational case study of synergies between an intense heat wave and the urban heat island in Beijing. *Journal of Applied Meteorology and Climatology*, 59(4):605–620, 2020.
- [25] He B-J, Wang J, Zhu J and Qi, J. Beating the urban heat: Situation, background, impacts and the way forward in China. *Renewable and Sustainable Energy Reviews*, 161:112350, 2022.
- [26] Jiang L, Chen Y D, Li J and Liu C. Amplification of soil moisture deficit and high temperature in a drought-heatwave co-occurrence in southwestern China. *Natural Hazards*, 111(1):641–660, 2022.
- [27] Kumar R and Mishra V. Decline in surface urban heat island intensity in India during heatwaves. *Environmental Research Communications*, 1(3):031001, 2019.
- [28] Zhao L, Oppenheimer M, Zhu Q, Baldwin J W, Ebi K L, Bou-Zeid E, Guan K and Liu X. Interactions between urban heat islands and heat waves. *Environmental research letters*, 13(3):034003, 2018.
- [29] Ramamurthy P and Bou-Zeid E. Heatwaves and urban heat islands: a comparative analysis of multiple cities. *Journal of Geophysical Research: Atmospheres*, 122(1):168–178, 2017.
- [30] Li D and Bou-Zeid E. Synergistic interactions between urban heat islands and heat waves: The impact in cities is larger than the sum of its parts. *Journal of Applied Meteorology and Climatology*, 52(9):2051–2064, 2013.
- [31] Chew L W, Liu X, Li X and Norford L K. Interaction between heat wave and urban heat island: A case study in a tropical coastal city, Singapore. *Atmospheric Research*, 247:105134, 2021.

- [32] Kunkel K E, Changnon S A, Reinke B C and Arritt R W. The July 1995 heat wave in the Midwest: A climatic perspective and critical weather factors. *Bulletin of the American Meteorological Society*, 77(7):1507–1518, 1996.
- [33] Schatz J and Kucharik C J. Urban climate effects on extreme temperatures in Madison, Wisconsin, USA. *Environmental Research Letters*, 10(9):094024, 2015.
- [34] Rizvi S H, Alam K and Iqbal M J. Spatio-temporal variations in urban heat island and its interaction with heat wave. *Journal of Atmospheric and Solar-Terrestrial Physics*, 185:50–57, 2019.
- [35] He X, Wang J, Feng J, Yan Z, Miao S, Zhang Y and Xia J. Observational and modeling study of interactions between urban heat island and heatwave in Beijing. *Journal of Cleaner Production*, 247:119169, 2020.
- [36] Katavoutas G and Founda D. Response of urban heat stress to heat waves in Athens (1960–2017). *Atmosphere*, 10(9):483, 2019.
- [37] Richard Y, Pohl B, Rega M, Pergaud J, Thevenin T, Emery J, Dudek J, Vairet T, Zito S and Chateau-Smith C. Is Urban Heat Island intensity higher during hot spells and heat waves (Dijon, France, 2014–2019)? *Urban Climate*, 35:100747, 2021.
- [38] Oliveira A, Lopes A, Correia E, Niza S and Soares A. Heatwaves and Summer Urban Heat Islands: A Daily Cycle Approach to Unveil the Urban Thermal Signal Changes in Lisbon, Portugal. *Atmosphere*, 12(3):292, 2021.
- [39] He B-J, Wang J, Liu H and Ulpiani G. Localized synergies between heat waves and urban heat islands: Implications on human thermal comfort and urban heat management. *Environmental Research*, 193:110584, 2021.
- [40] Miao S, Zhan W, Lai J, Li L, Du H, Wang C, Wang C, Li J, Huang F, Liu Z and Dong P. Heat wave-induced augmentation of surface urban heat islands strongly regulated by rural background. *Sustainable Cities and Society*, 82:103874, 2022.
- [41] Scott A A, Waugh D W and Zaitchik B F. Reduced Urban Heat Island intensity under warmer conditions. *Environmental Research Letters*, 13(6):064003, 2018.
- [42] Antipova A. Urban Environment: The Differences between the City in Europe and the United States. In *Urban Environment, Travel Behavior, Health, and Resident Satisfaction*, pages 35–117. Springer, 2018.

- [43] Founda D and Santamouris M. Synergies between Urban Heat Island and Heat Waves in Athens (Greece), during an extremely hot summer (2012). *Scientific reports*, 7(1):1–11, 2017.
- [44] Nicholson A. Analysis of the diurnal cycle of air temperature between rural Berkshire and the University of Reading: Possible role of the urban heat island. *Weather*, 75(8):235–241, 2020.
- [45] Unger J, Skarbit N, Kovács A and Gal T. Comparison of regional and urban outdoor thermal stress conditions in heatwave and normal summer periods: A case study. *Urban Climate*, 32:100619, 2020.
- [46] Wong K V, Paddon A and Jimenez A. Review of World Urban Heat Islands: Many Linked to Increased Mortality. *Journal of Energy Resources Technology*, 135(2), 03 2013. 022101.
- [47] Klein Tank A M G, Wijngaard J B, Können G P, Böhm R, Demarée G, Gocheva A, Mileta M, Pashiardis S, Hejkrlik L, Kern-Hansen C and others. Daily dataset of 20th-century surface air temperature and precipitation series for the European Climate Assessment. *International Journal of Climatology: A Journal of the Royal Meteorological Society*, 22(12):1441–1453, 2002 (Accessed on 04-Nov-2022). <https://www.ecad.eu/dailydata/predefinedseries.php#>.
- [48] Klok E J and Klein Tank A M G. Updated and extended European dataset of daily climate observations. *International Journal of Climatology: A Journal of the Royal Meteorological Society*, 29(8):1182–1191, 2009.
- [49] Smith A, Lott N and Vose R. The integrated surface database: Recent developments and partnerships. *Bulletin of the American Meteorological Society*, 92(6):704–708, 2011 (Accessed on 04-Nov-2022). <https://www.ncei.noaa.gov/data/global-summary-of-the-day/access>.
- [50] Rasilla D, Allende F, Martilli A and Fernández F. Heat waves and human well-being in Madrid (Spain). *Atmosphere*, 10(5):288, 2019.
- [51] Stefanon M, D’Andrea F and Drobinski P. Heatwave classification over Europe and the Mediterranean region. *Environmental Research Letters*, 7(1):014023, 2012.
- [52] Basara J B, Hall J P K, Schroeder A J, Illston B G and Nemunaitis K L. Diurnal cycle of the Oklahoma City urban heat island. *Journal of Geophysical Research: Atmospheres*, 113(D20), 2008.

- [53] Basara J B, Basara H G, Illston B G and Crawford K C. The impact of the urban heat island during an intense heat wave in Oklahoma City. *Advances in Meteorology*, 2010.
- [54] Oke T R. *Boundary layer climates*. Routledge, 2002.
- [55] Ackerman B. Temporal march of the Chicago heat island. *Journal of Climate and Applied Meteorology*, pages 547–554, 1985.
- [56] Hawkins T, Brazel A, Stefanov W, Bigler W and Saffell E. The role of rural variability in urban heat island determination for Phoenix, Arizona. *Journal of Applied Meteorology*, 43(3):476–486, 2004.
- [57] European Statistics (Eurostat) (Accessed on 04-Nov-2022). <https://ec.europa.eu/eurostat/data/database>.
- [58] Wolfram Research, Inc. Wolfram—Alpha Knowledgebase. Champaign, IL, 2022.
- [59] EEA. Copernicus land monitoring service-urban atlas, 2017 (Accessed on 04-Nov-2022). <https://www.eea.europa.eu/data-and-maps/data/copernicus-land-monitoring-service-urban-atlas>.
- [60] Li K, Chen Y, Wang M and Gong A. Spatial-temporal variations of surface urban heat island intensity induced by different definitions of rural extents in China. *Science of the Total Environment*, 669:229–247, 2019.
- [61] Hooyberghs H, Berckmans J, Lauwaet D, Lefebvre F and De Ridder K. Climate variables for cities in Europe from 2008 to 2017, version 1.0, Copernicus Climate Change Service (C3S) Climate Data Store (CDS), (Accessed on 04-Nov-2022), 2019. <https://doi.org/10.24381/cds.c6459d3a>.
- [62] Zhang P, Imhoff M L, Wolfe R E and Bounoua L. Characterizing urban heat islands of global settlements using MODIS and nighttime lights products. *Canadian Journal of Remote Sensing*, 36(3):185–196, 2010.
- [63] Martin-Vide J, Sarricolea P and Moreno-García M C. On the definition of urban heat island intensity: the “rural” reference. *Frontiers in Earth Science*, 3:24, 2015.
- [64] Ngarambe J, Nganyiyimana J, Kim I, Santamouris M and Yun G Y. Synergies between urban heat island and heat waves in Seoul: The role of wind speed and land use characteristics. *PLoS One*, 15(12):e0243571, 2020.

- [65] EEA. Corine Land Cover (CLC) 2018, Version 20b2, 2018 (Accessed on 04-Nov-2022). <https://land.copernicus.eu/pan-european/corine-land-cover/clc2018>.
- [66] Schumacher U. The Urban mask layer as reference geometry for spatial planning: Moving from German to European geodata. *KN-Journal of Cartography and Geographic Information*, 71(2):83–95, 2021.
- [67] Berckmans J, Lefebvre F, Hooyberghs H, De Ridder K, de’Donato F, Ducheyne E, Marsboom C, Páldy A, Adamonyte D, Voitonis E. Demo web-application URBAN.1 - C3S_422_Lot2_VITO – European Health, 2020.
- [68] Hersbach H, Bell B, Berrisford P, Biavati G, Horányi A, Muñoz Sabater J, Nicolas J, Peubey C, Radu R, Rozum I, Schepers D, Simmons A, Soci C, Dee D and Thépaut J-N. ERA5 hourly data on single levels from 1959 to present. Copernicus Climate Change Service (C3S) Climate Data Store (CDS), 2018 (Accessed on 04-Nov-2022). <https://doi.org/10.24381/cds.adbb2d47>.
- [69] Cornes R, Van Der Schrier G, Van Den Besselaar E and Jones P. An ensemble version of the E-OBS temperature and precipitation data sets. *Journal of Geophysical Research: Atmospheres*, 123(17):9391–9409, 2018.
- [70] Rousi E, Kornhuber K, Beobide-Arsuaga G, Luo F and Coumou D. Accelerated western European heatwave trends linked to more-persistent double jets over Eurasia. *Nature communications*, 13(1):1–11, 2022.
- [71] Di Napoli C, Barnard C, Prudhomme C, Cloke H L and Pappenberger F. ERA5-HEAT: A global gridded historical dataset of human thermal comfort indices from climate reanalysis. *Geoscience Data Journal*, 8(1):2–10, 2021.
- [72] Berckmans J, Lefebvre F, Hooyberghs H, De Ridder K, de’Donato F, Ducheyne E, Marsboom C, Páldy A, Adamonyte D, Voitonis E. Heat wave days for European countries derived from ERA5 reanalysis, 2021. <https://cds.climate.copernicus.eu/cdsapp#!/software/app-health-heat-waves-current-climate?tab=app>.
- [73] Perkins S. A review on the scientific understanding of heatwaves—Their measurement, driving mechanisms, and changes at the global scale. *Atmospheric Research*, 164:242–267, 2015.
- [74] Herbel I, Croitoru A-E, Rus A V, Roşca C F, Harpa G V, Ciupertea A-F and Rus I. The impact of heat waves on surface urban heat island and local

- economy in Cluj-Napoca city, Romania. *Theoretical and applied climatology*, 133(3):681–695, 2018.
- [75] Pyrgou A, Hadjinicolaou P and Santamouris M. Urban-rural moisture contrast: Regulator of the urban heat island and heatwaves’ synergy over a mediterranean city. *Environmental Research*, 182:109102, 2020.
- [76] Oliver E C J, Burrows M T, Donat M G, Sen Gupta A, Alexander L V, Perkins-Kirkpatrick S E, Benthuyzen J A, Hobday A J, Holbrook N J, Moore P J and others. Projected marine heatwaves in the 21st century and the potential for ecological impact. *Frontiers in Marine Science*, 6:734, 2019.
- [77] Welch B L. The generalization of Student’s problem when several different population variances are involved. *Biometrika*, 34(1-2):28–35, 1947.
- [78] Ruxton G D. The unequal variance t-test is an underused alternative to Student’s t-test and the Mann–Whitney U test. *Behavioral Ecology*, 17(4):688–690, 05 2006.
- [79] Wilks D S. *Statistical methods in the atmospheric sciences*, volume 100. Academic press, 2011.
- [80] Stewart I D. *Redefining the urban heat island*. PhD thesis, University of British Columbia, 2011.
- [81] Stewart I D and Oke T R. Local climate zones for urban temperature studies. *Bulletin of the American Meteorological Society*, 93(12):1879–1900, 2012.
- [82] Demuzere M, Bechtel B, Middel A and Mills G. Mapping Europe into local climate zones. *PloS one*, 14(4):e0214474, 2019.
- [83] Geiger R. Klassifikation der Klimate nach W. Köppen [Classification of climates after W. Köppen]. Landolt-Börnstein–Zahlenwerte und Funktionen aus Physik, Chemie, Astronomie, Geophysik und Technik, alte Serie. *Berlin: Springer*, 3:603–607, 1954.
- [84] Peel M C, Finlayson B L and McMahon T A. Updated world map of the köppen-geiger climate classification. *Hydrology and earth system sciences*, 11(5):1633–1644, 2007.
- [85] Rubel F, Brugger K, Haslinger K and Auer I. The climate of the European Alps: Shift of very high resolution Köppen-Geiger climate zones 1800–2100. *Meteorologische Zeitschrift*, 26(2):115–125, 2017.

- [86] Zong L, Liu S, Yang Y, Ren G, Yu M, Zhang Y and Li Y. Synergistic influence of local climate zones and wind speeds on the urban heat island and heat waves in the megacity of Beijing, China. *Frontiers in Earth Science*, 9:673786, 2021.
- [87] Tian W, Yang Y, Wang L, Zong L, Zhang Y and Liu D. Role of local climate zones and urban ventilation in canopy urban heat island–heatwave interaction in Nanjing megacity, China. *Urban Climate*, 49:101474, 2023.
- [88] De Ridder K, Lauwaet D and Maiheu B. UrbClim–A fast urban boundary layer climate model. *Urban Climate*, 12:21–48, 2015.
- [89] Hathway EA and Sharples S. The interaction of rivers and urban form in mitigating the Urban Heat Island effect: A UK case study. *Building and Environment*, 58:14–22, 2012.
- [90] Mishra A and Singh V. A review of drought concepts. *Journal of hydrology*, 391(1-2):202–216, 2010.
- [91] WHO, Constitution of and others. World Health Organization. *Responding to Community Spread of COVID-19*, 2020.
- [92] World Meteorological Organization (WMO). Report on drought and countries affected by drought during 1974-1985. *WMO, Geneva*, page 118, 1986.
- [93] Food and Agriculture Organization (FAO). Guidelines: Land evaluation for Rainfed Agriculture. *FAO Soils Bulletin, Rome*, page 52, 1983.
- [94] Wilhite D and Glantz M. Understanding the drought phenomenon: the role of definitions. *Water international*, 10(3):111–120, 1985.
- [95] Crausbay S, Ramirez A, Carter S, Cross M, Hall K, Bathke D, Betancourt J, Colt S, Cravens A, Dalton M and others. Defining ecological drought for the twenty-first century. *Bulletin of the American Meteorological Society*, 98(12):2543–2550, 2017.
- [96] Van Lanen H and others. Drought propagation through the hydrological cycle. *IAHS publication*, 308:122, 2006.
- [97] Wilhite Donald. Drought monitoring and early warning: concepts, progress and future challenges. *World Meteorological Organization, Geneva, Switzerland. WMO*, 1006, 2006.
- [98] Friedman D. *The prediction of long-continuing drought in south and southwest Texas*. Number 1. Travelers Insurance Company, 1957.

- [99] McKee T, Doesken N, Kleist J and others. The relationship of drought frequency and duration to time scales. In *Proceedings of the 8th Conference on Applied Climatology*, volume 17, pages 179–183. Boston, MA, USA, 1993.
- [100] Palmer W. *Meteorological drought*, volume 30. US Department of Commerce, Weather Bureau, 1965.
- [101] Vicente-Serrano S, Beguería S and López-Moreno J. A multiscale drought index sensitive to global warming: the standardized precipitation evapotranspiration index. *Journal of climate*, 23(7):1696–1718, 2010.
- [102] Byun H-R and Wilhite D. Daily quantification of drought severity and duration. *Journal of Climate*, 5:1181–1201, 1996.
- [103] Tsakiris G and Vangelis H. Establishing a drought index incorporating evapotranspiration. *European water*, 9(10):3–11, 2005.
- [104] Hao Z and AghaKouchak A. A nonparametric multivariate multi-index drought monitoring framework. *Journal of Hydrometeorology*, 15(1):89–101, 2014.
- [105] Narasimhan B and Srinivasan R. Development and evaluation of Soil Moisture Deficit Index (SMDI) and Evapotranspiration Deficit Index (ETDI) for agricultural drought monitoring. *Agricultural and forest meteorology*, 133(1-4):69–88, 2005.
- [106] Hao Z and AghaKouchak A. Multivariate standardized drought index: a parametric multi-index model. *Advances in Water Resources*, 57:12–18, 2013.
- [107] Modarres R. Streamflow drought time series forecasting. *Stochastic Environmental Research and Risk Assessment*, 21(3):223–233, 2007.
- [108] Nalbantis I and Tsakiris G. Assessment of hydrological drought revisited. *Water resources management*, 23(5):881–897, 2009.
- [109] McKee T. Drought monitoring with multiple time scales. In *Proceedings of 9th Conference on Applied Climatology, Boston, 1995*, 1995.
- [110] Zhuang X, Hao Z, Singh V, Zhang Y, Feng S, Xu Y and Hao F. Drought propagation under global warming: Characteristics, approaches, processes, and controlling factors. *Science of The Total Environment*, page 156021, 2022.
- [111] Xu Y, Wang L, Ross K, Liu C and Berry K. Standardized soil moisture index for drought monitoring based on soil moisture active passive observations and

36 years of north American land data assimilation system data: A case study in the southeast United States. *Remote Sensing*, 10(2):301, 2018.

- [112] Zhou K, Li J, Zhang T and Kang A. The use of combined soil moisture data to characterize agricultural drought conditions and the relationship among different drought types in China. *Agricultural Water Management*, 243:106479, 2021.
- [113] Bae H, Ji H, Lim Y-J, Ryu Y, Kim M-H and Kim B-J. Characteristics of drought propagation in South Korea: Relationship between meteorological, agricultural, and hydrological droughts. *Natural Hazards*, 99(1):1–16, 2019.
- [114] Li Y, Huang S, Wang H, Zheng X, Huang Q, Deng M and Peng J. High-resolution propagation time from meteorological to agricultural drought at multiple levels and spatiotemporal scales. *Agricultural Water Management*, 262:107428, 2022.
- [115] Quiring S, Ford T, Wang J, Khong A, Harris E, Lindgren T, Goldberg D and Li Z. The North American soil moisture database: Development and applications. *Bulletin of the American Meteorological Society*, 97(8):1441–1459, 2016.
- [116] Zhu Y, Liu Y, Wang W, Singh V and Ren L. A global perspective on the probability of propagation of drought: From meteorological to soil moisture. *Journal of Hydrology*, 603:126907, 2021.
- [117] Tian Q, Lu J and Chen X. A novel comprehensive agricultural drought index reflecting time lag of soil moisture to meteorology: A case study in the Yangtze River basin, China. *Catena*, 209:105804, 2022.
- [118] Xia Y, Sheffield J, Ek M, Dong J, Chaney N, Wei H, Meng J and Wood E. Evaluation of multi-model simulated soil moisture in NLDAS-2. *Journal of Hydrology*, 512:107–125, 2014.
- [119] Páscoa P, Gouveia CM, Russo A, Trigo RM and others. Drought trends in the Iberian Peninsula over the last 112 years. *Advances in Meteorology*, 2017, 2017.
- [120] Martín-Vide J and Barriendos Vallvé M. The use of rogation ceremony records in climatic reconstruction: a case study from Catalonia (Spain). *Climatic Change*, 30(2):201–221, 1995.
- [121] Austin R, Cantero-Martinez C, Arrúe JL, Playán E and Cano-Marcellán P. Yield-rainfall relationships in cereal cropping systems in the Ebro river valley of Spain. *European Journal of Agronomy*, 8(3-4):239–248, 1998.

- [122] Vicente-Serrano S, Lopez-Moren, J, Beguería S, Lorenzo-Lacruz J, Sanchez-Lorenzo A, García-Ruiz J, Azorin-Molina C, Morán-Tejeda E, Revuelto J, Trigo R and others. Evidence of increasing drought severity caused by temperature rise in southern Europe. *Environmental Research Letters*, 9(4):044001, 2014.
- [123] Greve P, Orlowsky B, Mueller B, Sheffield J, Reichstein M and Seneviratne S. Global assessment of trends in wetting and drying over land. *Nature geoscience*, 7(10):716–721, 2014.
- [124] Khan M I, Zhu X, Arshad M, Zaman M, Niaz Y, Ullah I, Anjum M N and Uzair M. Assessment of spatiotemporal characteristics of agro-meteorological drought events based on comparing Standardized Soil Moisture Index, Standardized Precipitation Index and Multivariate Standardized Drought Index. *Journal of Water and Climate Change*, 11(S1):1–17, 2020.
- [125] Xu L, Chen N, Yang C, Zhang C and Yu H. A parametric multivariate drought index for drought monitoring and assessment under climate change. *Agricultural and Forest Meteorology*, 310:108657, 2021.
- [126] Nelsen R B. *An introduction to copulas*. Springer science & business media, 2007.
- [127] Gringorten I. A plotting rule for extreme probability paper. *Journal of Geophysical Research*, 68(3):813–814, 1963.
- [128] Salvadori G, De Michele C, Kottegoda N T and Rosso R. *Extremes in nature: an approach using copulas*, volume 56. Springer Science & Business Media, 2007.
- [129] Ojeda M, Gámiz-Fortis S, Romero-Jiménez E, Rosa-Cánovas J, Yeste P, Castro-Díez Y and Esteban-Parra M. Projected changes in the Iberian Peninsula drought characteristics. *Science of The Total Environment*, 757:143702, 2021.
- [130] Spinoni J, Vogt J, Naumann G, Barbosa P and Dosio A. Will drought events become more frequent and severe in Europe? *International Journal of Climatology*, 38(4):1718–1736, 2018.
- [131] Spinoni J, Naumann G, Vogt J and Barbosa P. Meteorological droughts in europe: events and impacts-past trends and future projections. 2016.

- [132] Muñoz Sabater J. ERA5-land monthly averaged data from 1981 to present, Copernicus Climate Change Service (C3S) Climate Data Store (CDS), 2019 (Accessed on 04-Nov-2022). <https://doi.org/10.24381/cds.68d2bb30>.
- [133] Zhang R, Li L, Zhang Y, Huang F, Li J, Liu W, Mao T, Xiong Z and Shang-guan W. Assessment of agricultural drought using soil water deficit index based on ERA5-land soil moisture data in four southern provinces of China. *Agriculture*, 11(5):411, 2021.
- [134] Beck H E, Pan M, Miralles D G, Reichle R H, Dorigo W A, Hahn S, Sheffield J, Karthikeyan L, Balsamo G, Parinussa R M and others. Evaluation of 18 satellite-and model-based soil moisture products using in situ measurements from 826 sensors. *Hydrology and Earth System Sciences*, 25(1):17–40, 2021.
- [135] Muñoz-Sabater J, Dutra E, Agustí-Panareda A, Albergel C, Arduini G, Balsamo G, Boussetta S, Choulga M, Harrigan S, Hersbach H and others. ERA5-Land: A state-of-the-art global reanalysis dataset for land applications. *Earth System Science Data*, 13(9):4349–4383, 2021.
- [136] Arora V and Boer G. A representation of variable root distribution in dynamic vegetation models. *Earth Interactions*, 7(6):1–19, 2003.
- [137] Qiu J, Crow W and Nearing G. The impact of vertical measurement depth on the information content of soil moisture for latent heat flux estimation. *Journal of Hydrometeorology*, 17(9):2419–2430, 2016.
- [138] Bageshree K and Kinouchi T. A Multivariate Drought Index for Seasonal Agriculture Drought Classification in Semiarid Regions. *Remote Sensing*, 14(16):3891, 2022.
- [139] Monteith J. Evaporation and environment. In *Symposia of the society for experimental biology*, volume 19, pages 205–234. Cambridge University Press (CUP) Cambridge, 1965.
- [140] Myneni R and Williams D. On the relationship between FAPAR and NDVI. *Remote Sensing of Environment*, 49(3):200–211, 1994.
- [141] Gobron N, Pinty B, Mélin F, Taberner M, Verstraete M, Belward A, Lavergne T and Widlowski J-L. The state of vegetation in Europe following the 2003 drought. *International Journal of Remote Sensing*, 26(9):2013–2020, 2005.
- [142] Spinoni J, Muñoz C, Masante D, McCormick N, Vogt J and Barbosa P. European Drought Observatory. 2018.

- [143] Peng J, Muller J-P, Blessing S, Giering R, Danne O, Gobron N, Kharbouche S, Ludwig R, Müller B, Leng G and others. Can we use satellite-based FAPAR to detect drought? *Sensors*, 19(17):3662, 2019.
- [144] Zhang Q, Li Q, Singh V, Shi P, Huang Q and Sun P. Nonparametric integrated agrometeorological drought monitoring: Model development and application. *Journal of Geophysical Research: Atmospheres*, 123(1):73–88, 2018.
- [145] Yevjevich V. *Objective approach to definitions and investigations of continental hydrologic droughts*. PhD thesis, Colorado State University. Libraries, 1967.
- [146] Huang S, Huang Q, Chang J, Leng G and Xing L. The response of agricultural drought to meteorological drought and the influencing factors: A case study in the Wei River Basin, China. *Agricultural Water Management*, 159:45–54, 2015.
- [147] Sattar M, Lee J-Y, Shin J-Y and Kim T-W. Probabilistic characteristics of drought propagation from meteorological to hydrological drought in South Korea. *Water Resources Management*, 33(7):2439–2452, 2019.
- [148] Ivanova M. Assessing the United Nations Environment Programme. *Global commons*, 2:117–158, 2006.
- [149] Sapir D and Misson C. The development of a database on disasters. *Disasters*, 16(1):74–80, 1992.
- [150] Tijdeman E, Blauhut V, Stoelzle M, Menzel L and Stahl K. Different drought types and the spatial variability in their hazard, impact, and propagation characteristics. *Natural Hazards and Earth System Sciences*, 22(6):2099–2116, 2022.
- [151] Coll J, Aguilar E and Ashcroft L. Drought variability and change across the Iberian Peninsula. *Theoretical and Applied Climatology*, 130(3):901–916, 2017.
- [152] Scaini A, Sánchez N, Vicente-Serrano S and Martínez-Fernández J. SMOS-derived soil moisture anomalies and drought indices: A comparative analysis using in situ measurements. *Hydrological Processes*, 29(3):373–383, 2015.
- [153] Ojeda M, Possega M, Romero-Jiménez E, Rosa-Cánovas J, Yeste P, Castro-Díez Y, Esteban-Parra M, Di Sabatino S and Gámiz-Fortis S. Drought characteristic projections over the Iberian Peninsula: the effect of using nonparametric multivariate standardized drought indices. Technical report, Copernicus Meetings, 2022.

- [154] Jacob D, Petersen J, Eggert B, Alias A, Christensen O, Bouwer L, Braun A, Colette A, Déqué M, Georgievski G and others. EURO-CORDEX: new high-resolution climate change projections for European impact research. *Regional environmental change*, 14(2):563–578, 2014.
- [155] García-Herrera R, Hernández E, Barriopedro D, Paredes D, Trigo R, Trigo I and Mendes M. The outstanding 2004/05 drought in the Iberian Peninsula: associated atmospheric circulation. *Journal of Hydrometeorology*, 8(3):483–498, 2007.
- [156] Ma H, Wang Y and Lin Z. Future changes of summer heat waves over urban agglomerations in eastern China under 1.5 C and 2.0 C global warming. *Frontiers in Earth Science*, 10:113, 2022.
- [157] Silva R, Carvalho A C, Pereira S C, Carvalho D and Rocha A. Lisbon urban heat island in future urban and climate scenarios. *Urban Climate*, 44:101218, 2022.
- [158] Wong G, Van Lanen H and Torfs P. Probabilistic analysis of hydrological drought characteristics using meteorological drought. *Hydrological Sciences Journal*, 58(2):253–270, 2013.